

REVIEW ARTICLE

Neutron Scattering Studies of the Model Glass Former Ortho-terphenyl

Albert Tölle

Department of Biophysics, Biocenter University of Basel, CH-4056 Basel, Switzerland

E-mail: Albert.Toelle@unibas.ch

Abstract. The van der Waals liquid orthoterphenyl has long been used as a model system in the study of the glass transition. Motivated by mode-coupling theory, extensive experiments have been undertaken to monitor the onset of structural relaxation on microscopic time and length scales. Using in particular quasielastic neutron scattering, the decay of density and tagged-particle correlations has been measured as a function of temperature, pressure and wave number. A consistent picture is developed in which the mode-coupling singularity appears as a change of transport mechanism in the moderately viscous liquid, at temperatures far above the conventional (caloric) glass transition.

PACS numbers: 64.70.Pf, 62.50.+p, 61.25.Em, 61.12.-q

Submitted to: *Rep. Prog. Phys.*

1. Introduction

A glass may simply be defined as a non-crystalline solid and is described by the predominance of local order. Translational symmetry, *i. e.* long range order, is lacking. The term *frozen liquid* stresses the structural similarity to a liquid.

By *glass transition* we define the process of solidification of a supercooled liquid to a non-crystalline solid, more exactly we may call it a *liquid-to-glass transition*. When crystallization during cooling can be avoided the structural α -relaxation time τ increases dramatically. In a normal liquid the relaxation time is of the order of 1 psec, it increases continuously within a narrow temperature range over many orders of magnitude to attain values in the range of seconds, hours or even days. Then the supercooled liquid is conventionally called a glass.

Many theoretical concepts have been proposed to explain the glass transition among these free-volume and thermodynamic theories. In the free-volume theories, introduced by Cohen and Turnbull [1] and substantiated by Cohen and Grest [2] the slowing down of the dynamics is related to the decrease of free volume and excess entropy. Thermodynamic theories first formulated by Gibbs and Di-Marzio [3] and Adams and Gibbs [4] assume an underlying second-order phase transition in the limit $\tau \rightarrow \infty$ to account for the Kauzmann paradox.

A new approach to the problem was opened up after the mode-coupling approximation has been introduced first by Leutheusser [5] and independently by Bengtzelius, Götze and Sjögren [6]. It provides an approximation scheme which allows for the calculation of the evolution of time correlations from a microscopic equation of motion and basically deals with the two well known phenomena: cage and backflow effect. In order to understand the structural relaxation it is proposed to investigate the short-time limit $\tau \simeq 1$ psec where relaxational motion begins to evolve from elementary vibrations of atoms or molecules.

Even in its most reduced schematic form mode-coupling theory (MCT) is able to describe essential features of structural relaxation and provides new predictions which can be tested experimentally. Numeric solutions of mode-coupling equations describe the dynamics of computer liquids or colloids with an accuracy of better than 10% *without* any adjustable parameters [7, 8, 9]. The structure of the theory suggests that the asymptotic results hold also for more complicated “real” glass formers. However, only experiments can decide to which extent “real” systems reach the asymptotic behaviour predicted by theory. An increasing number of measurements on many *different* materials has been devoted to this question and give evidence for the relevance of the mode-coupling theory [10].

In the present review, we survey results for *one* often studied model system, the molecular liquid *orthoterphenyl* (OTP) (section 2). The glass former orthoterphenyl can be considered to be a very good candidate to test the validity of such a theory as the molecules are relatively symmetric and rigid. The model character is underlined by the recurrent use for experimental studies and tests of various theories [11].

Neutron scattering is particularly well suited to test microscopic theories as it measures directly the density and tagged-particle correlations on time scales of psec ... nsec and on length scales of intermolecular distances and therefore provides an ideal link between theory and experiment. Thus, neutron scattering experiments have been performed in a large variety of different glass forming systems like ionic glasses [12, 13, 14, 15], polymers [16, 17, 18] and even metallic glasses [19, 20, 21]. A comparison can be found in [22].

To establish the context, we first describe some glass transition signatures (section 3) and some examples of the evolution of structural relaxation on time scales $\tau \gg 1$ nsec accessible by conventional techniques. After some remarks on the experimental method neutron scattering (section 4) a short introduction into the mode-coupling theory of the glass transition (section 5) is given. We then concentrate on the fast dynamics on the psec...nsec time scale. Tagged-particle and collective motion in liquid, glassy and crystalline (section 8) orthoterphenyl have been investigated as a function of temperature (section 6), pressure (section 7) and scattering vector. In this range time correlation functions evolve from vibrations (section 8) at very short times to structural relaxation through an intermediate regime for which the mode-coupling theory makes the most prominent predictions.

The neutron scattering experiments on OTP are probably the most intensive study on a molecular glass former up to now. Here, we not only summarize previously published results, but we also present many new yet unpublished data. Some experimental limitations are discussed in detail. Those figures, which are here published for the first time, or where we include new unpublished data are denoted by “*” in the figure caption. All other figures (or data) are taken from the literature as stated in the caption. This review marks the end of a long term project that was supported over more than 10 years by BMBF under project numbers 03SI2MAI, 03FU4DOR4 and 03FU5DOR1.

2. Orthoterphenyl

Every liquid may be solidified as a glass provided crystallization can be bypassed. Practically, atomic liquids cannot be supercooled into the region of interest without immediate crystallization. The discovery of a concentration driven glass transition in colloidal suspensions provided new model systems in which the dynamics on the length scale of the nearest neighbours is probed by dynamic light scattering. Indeed, very impressive confirmations of MCT predictions have been provided by light scattering studies in such systems [7, 8, 9].

According to mode-coupling theory the dramatic increase of the relaxation time with decreasing temperature or increasing pressure is due to relatively subtle but smooth changes in the static structure factor. Since the theory was originally derived for “simple liquids”, it can be expected to be more reliable for simple systems without internal degrees of freedom than for more complicated molecules.

Molecular liquids form stable supercooled liquids in favorable cases. However, processes related to the molecular complexity which allows for supercooling should not screen phenomena that are predicted by MCT, which, originally, has been developed for simple atomic liquids with hard-core or Lennard-Jones interaction potentials without internal degrees of freedom.

The van der Waals liquid Orthoterphenyl (OTP: 1,2-diphenylbenzene, $C_{18}H_{14}$, boiling point $T_b = 605$ K, melting point $T_m=329$ K) is extensively studied for more than 40 years as an archetypical glass former by many methods and is representative for a whole class of glasses named fragile [23], whose characteristic is an extremely non-Arrhenius behavior of the shear viscosity $\eta(T)$ [24, 25, 26, 27, 28]. OTP is a relatively simple compact, non-polar molecule with an overall shape that comes close to the spherical particles preferred by theory. It consists of small, hopefully rigid molecular units which interact via weak non-directional van der Waals forces. Therefore, we expect that the dynamics of supercooled OTP represents structure independent, generic properties of glass forming liquids and does not depend on microscopic structural peculiarities.

The molecule consists of a central benzene ring and two lateral phenyl rings in ortho position. For steric reasons, the lateral two phenyl rings are necessarily rotated out of plane as shown in figure 1. In addition, the overcrowding in the molecule leads to significant bond-angle and out-of-plane distortions of the phenyl-phenyl bonds. Such structural irregularities may explain why OTP can be supercooled far easier than *m*- or *p*-terphenyl [29].

A number of structural features of the OTP molecule have their origin in the close proximity of the two bulky lateral phenyl rings. However, the details of the molecular structure may depend on whether it is in the crystalline, liquid, glassy or gas phase.

In the crystal, the angles for the out-of-plane rotation of the lateral phenyl rings are $\phi_1 \simeq 43^\circ$ and $\phi_2 \simeq 62^\circ$ [30, 31]. For isolated molecules, an old electron diffraction study had suggested $\phi_1 = \phi_2 = 90^\circ$ [32], but newer experiments and calculations agree

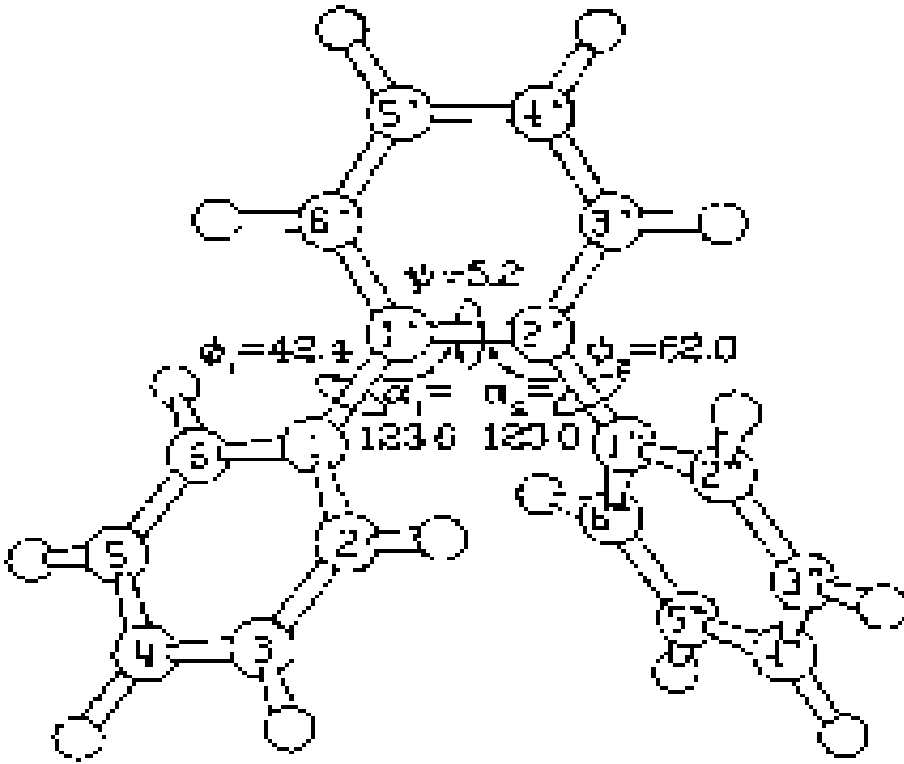


Figure 1. Molecular geometry of orthoterphenyl ($C_{18}H_{14}$) as observed in the crystal structure. It is constituted by three phenyl rings, the two lateral rings being attached to the central one by covalent bonds.

that in the gas or liquid phase $40^\circ \lesssim \phi_1, \phi_2 \lesssim 65^\circ$ [33, 34, 35].

The crystal structure belongs to the orthorhombic space group $P2_12_12_1$ with four molecules per unit cell and lattice parameters $a = 18.583 \text{ \AA}$, $b = 6.024 \text{ \AA}$, $c = 11.728 \text{ \AA}$ at room temperature [30, 31]. A sketch of the structure is given in figure 1 of Ref. [30]. Experimental studies of the crystalline state have been performed mainly on polycrystalline powder samples or on rather small single crystal needles. However, single crystals of high quality and considerable size (several cm^3) can be grown out of a hot methanol solution either by very slow cooling or by evaporation over several months [36]. The crystals grow preferentially along the shortest axis b .

Crystallization behavior of high purity OTP has been studied extensively over a range of supercooling up to above the melting point in connection with the glass forming ability [37, 38, 39, 40, 41]. For many glass formers the rate of cooling is taken as determining whether or not a liquid will form a glass. If unperturbed, OTP and some liquids of similarly shaped molecules require years to nucleate [37, 42]. However, if abundant stable nuclei are artificially created in the sample, then the overall liquid \rightarrow solid transformation occurs fairly rapidly on the time scale of seconds or minutes. The crystal growth rate of OTP at atmospheric pressure passes through a maximum value at 312 K [37]. On the other hand, nucleation frequencies are difficult to measure and

are usually calculated using classical nucleation theory. For example, the steady state homogeneous nucleation frequency is highest at 251 K [41]. The bulk heterogeneous nucleation frequency maximum lies between 260 K and 275 K for contact angles of 100° and 70°, respectively [40]. In most cases, nucleation takes place (heterogeneously) on surface heterogeneities whereas homogeneous nucleation is rather exceptional in glass forming liquids [40]. Heterogeneous nucleation at glass surfaces has not been studied rigorously, even though it is the most common origin of devitrification. Such nucleation may occur whether the surface of the glass is in contact with a container wall or exposed to atmosphere. Heterogeneities characterized by small contact angles have a marked effect on the cooling rates required for glass formation, with the required cooling rate increasing with decreasing contact angle [39, 40]. Nevertheless, with some care it is relatively easy to supercool OTP below the melting point. Depending on the cooling rate, the calorimetric glass transition temperature T_g lies between 242 K [43] and 245 K [25]. Thus, OTP is rather easy to handle as the melting and the glass transition temperature are close to ambient temperature.

One further advantage particularly useful in neutron scattering studies is that the molecule can be selectively or even fully deuterated. As a proton containing system the scattering is almost purely incoherent enabling us to study the single particle or tagged-particle dynamics. Fully deuterated the scattering is mainly coherent giving rise to the observation of the pair correlation function. Partial deuteration can be used to hide groups of atoms and to study the intra- and intermolecular motions separately.

Furthermore, we chose OTP for our investigations since it has been extensively studied in the literature by many spectroscopic methods as we will see in the next section (3). Thus, as a function of temperature and pressure many data are available for comparison.

3. Glass Transition in OTP

3.1. Macroscopic Quantities

The calorimetric techniques used for measuring the heat capacity c_p of glasses are the same as used for other solid materials. In particular, differential scanning calorimetry (DSC) [43, 44] or differential thermal analysis (DTA) [45] are used to determine the glass transition temperature T_g . When the heat capacity $c_p(T)$ of a supercooled liquid is measured as a function of temperature (or pressure) one notices a significant change occurring at a temperature T_g (figure 2). A similar effect is observed in volume–

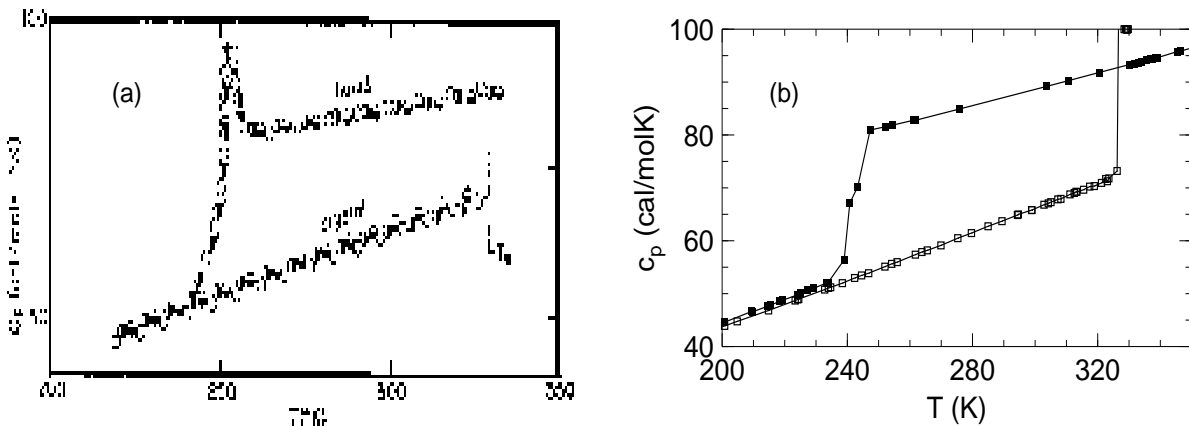


Figure 2. Specific heat of liquid, supercooled liquid, glassy and crystalline OTP obtained by differential scanning calorimetry. The data in the left part (a) are obtained with a scanning speed of 0.3 K/s (reproduced from [44]) while for the data on the right (b) the scanning speed was 0.003 K/s (values taken from [43]).

temperature–pressure measurements [46], reproduced in figure 3. A ”discontinuity” in the thermal expansion coefficient $\alpha = \partial \ln V / \partial T|_P$, the derivative of the volume V at constant pressure P can be deduced from figure 3 for the glass while nothing particular happens in the crystal. Although these features are characteristic of a second–order equilibrium phase transition, T_g cannot be related unambiguously to an equilibrium function, such as the free energy. In particular, the position and the sharpness of the transition near T_g depends on the cooling rate at which for example the heat capacity is monitored. In figure 2 results with two different cooling rates [44, 43] are compared. Conventionally, cooling rates of about 10 K/min are used to determine T_g . Operationally, T_g is defined as the center of the temperature range of the large change in the heat capacity in a DSC run with cooling rate \dot{T} . Note, that in this definition the glass transition is related with a low–frequency excitation: e. g. for a typical rate of $\dot{T} = 10 \text{ K/min} \simeq 0.2 \text{ K/s}$ and a width of the c_p –jump $\Delta T = 10 \text{ K}$ the excitation frequency is $\omega = \dot{T} / \Delta T = 0.02 \text{ s}^{-1}$, thus probing correlation times of about 50 s. The glass transition temperature defined in this manner can be understood as an isodynamic point which allows for a comparison of different glasses.

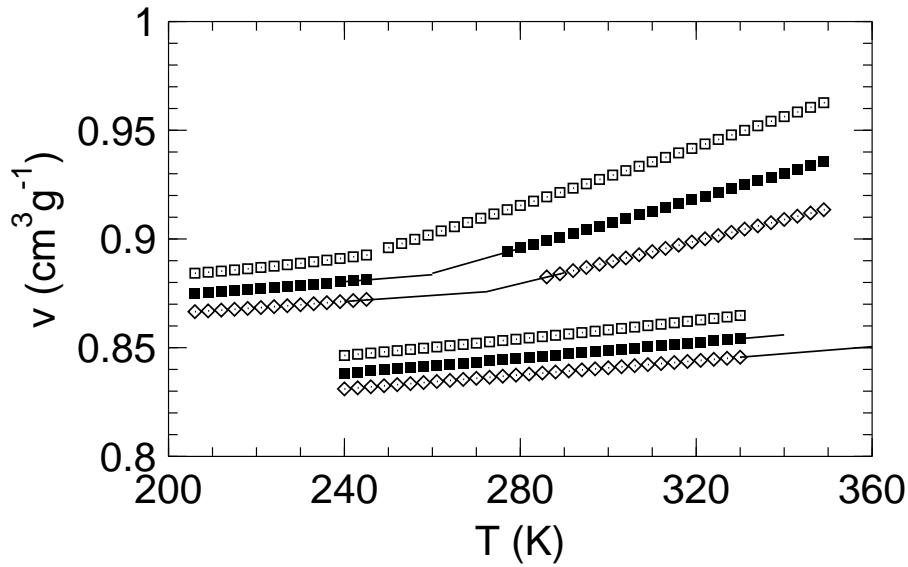


Figure 3. Variations of the isobaric specific volume of liquid, supercooled, glassy and crystalline OTP as a function of temperature for various pressures 0.1 MPa (\square), 50 MPa (\blacksquare) and 100 MPa (\diamond). The solid lines are linear extrapolations from either side. Reproduced using polynomial coefficients given in [46].

When pressure is applied the transition point shifts to higher temperatures as can be seen in the volume–temperature–pressure relation in figure 3. Note, that under pressure OTP shows a very strong density change. Calorimetrically, the glass transition temperature in OTP as a function of pressure, $T_g(P)$, has been measured by DTA by Atake and Angell [45]. Up to at least about 100 MPa the variation of $T_g(P)$ is linear with a slope $dT_g/dP \simeq 0.26$ K/MPa (260 K/GPa). These values for OTP and its isomeric mixtures are the highest yet observed for molecular liquids (though some polymers exhibit higher values). It was suspected that dT_g/dP is larger the more closely the molecular substance behaves repulsively like a hard sphere. These facts have been further motivations for us to use OTP as a model system also for pressure dependent neutron scattering experiments (section 7).

3.2. Primary α -Relaxation: Stretching and Scaling

The fluctuation–dissipation theorem connects a linear response with the time evolution or spectral distribution of spontaneous fluctuations. Thus, relaxation in the equilibrium state can be studied by a variety of spectroscopic or scattering methods.

Time–resolved measurements are performed for instance by photon–correlation spectroscopy (PCS) which measures ultimately the evolution of density correlations $\Phi(t)$ [47, 48, 49]. The PCS data in figure 4 illustrate nicely the most prominent features of structural relaxation: stretching, scaling and a strong temperature and pressure dependence of the mean relaxation time.

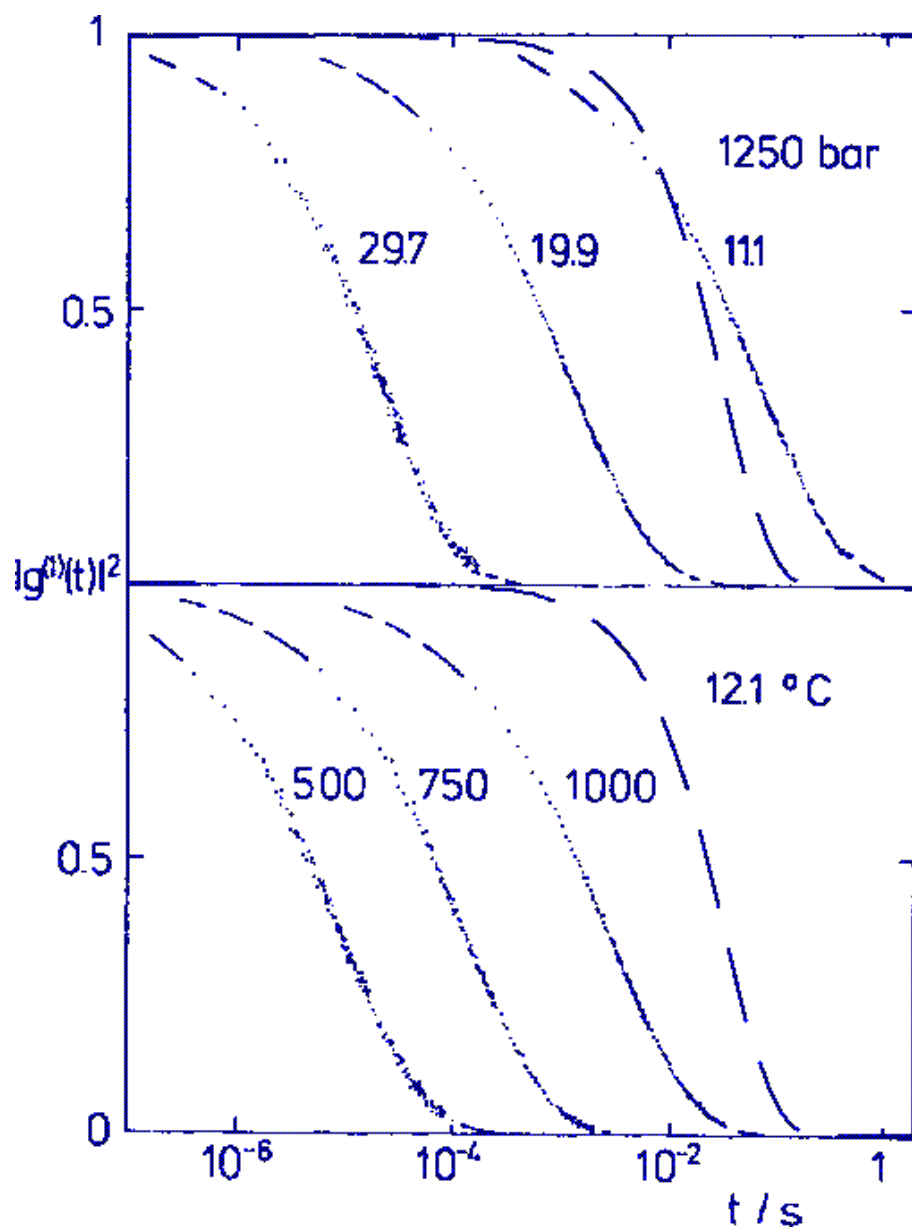


Figure 4. Normalized time–correlation function of liquid OTP, obtained by photon correlation spectroscopy in depolarized (VH) scattering geometry at constant pressure (top) and at constant temperature (bottom). The Kohlrausch stretched exponential is fitted to the data (dots) with exponents β between 0.53 and 0.62. Reproduced from [48]. For comparison, a simple exponential function was added (long dashed line).

The decay of the time correlations $\Phi(t)$ is called *stretched* since it extends over a much wider time range than a simple exponential process. An exponential decay is expected when the dynamics consists of uncorrelated random steps. This is the case for tagged–particle diffusion like motion in the long time and long distance limit [50]. On microscopic scales, however, the motion of molecules is a highly collective process

marked by memory effects.

In many cases the structural relaxation function $\Phi(t)$ is well described by a Kohlrausch law [51, 52], obtained by replacing t/τ in the Debye law by $(t/\tau)^\beta$:

$$\Phi(t) = \exp(-(t/\tau)^\beta), \quad 0 < \beta < 1. \quad (1)$$

For this function, the mean relaxation time $\langle\tau\rangle$ can be calculated as

$$\langle\tau\rangle = \int_0^\infty dt \Phi(t) = \tau \beta^{-1} \Gamma(\beta^{-1}) \quad (2)$$

where $\Gamma()$ is the gamma function. The exponent β is *not* (!) a material constant; it differs for different correlation functions or observables which are probed by different experimental techniques [53] (see also figure 6). Such variations of β demonstrate that an understanding of structural relaxation will not be possible without accounting for the different ways in which experimental probes couple to the microscopic degrees of freedom.

On cooling or compressing a viscous liquid, $\langle\tau\rangle$ increases rapidly as can be seen in figures 4 and 5 while the line shape of $\Phi(t)$, expressed through β varies only weakly. This *scaling* property, known as the *time-temperature-pressure superposition*, implies that in a first approximation the measured individual correlations $\Phi(t; T, P)$ can be collapsed onto a master curve

$$\Phi(t; T, P) = \Phi(t/\tau(T, P)) \quad (3)$$

by rescaling the time axis to $\hat{t} = t/\tau(T, P)$. This property turns out to be particularly useful in the analysis of neutron scattering experiments, to be discussed later in sections 6.5 and 7.5.

In many spectroscopic experiments, the response of a viscous liquid is probed as a function of frequency. A complex susceptibility $\chi(\omega)$ is related to the relaxation function $\Phi(t)$ through

$$\chi(\omega) = \chi_\infty + (\chi_\infty - \chi_0) \int_0^\infty dt e^{i\omega t} \dot{\Phi}(t). \quad (4)$$

For high frequencies, the system reacts as a solid $\chi(\omega \gg \tau^{-1}) = \chi_\infty$; for very low frequencies the fluid-like response is given by $\chi(\omega \ll \tau^{-1}) = \chi_0$.

For intermediate frequencies $\omega \simeq \tau^{-1}$ the Kramers-Kronig relation relates the step in the real part $\chi'(\omega)$ to the maximum in the dissipative part $\chi''(\omega)$. An exponential decay of $\Phi(t)$ leads to

$$\chi(\omega) = \chi_\infty + \frac{\chi_\infty - \chi_0}{1 - i\omega\tau}, \quad (5)$$

which in the context of structural relaxation is often named after Debye, who derived it for Brownian motion of uncorrelated dipoles in a viscous medium [54].

For a stretched relaxation function, the step in $\chi'(\omega)$ and the peak in $\chi''(\omega)$ are much broader than a Debye peak. To describe $\chi(\omega)$ one can either decorate (5) with one or two exponents [55, 56, 57] or use the Fourier transform of (1) [58].

Frequency dependent dielectric susceptibilities for pure OTP have rarely been studied [59, 60, 61, 62, 63] probably due to the extremely weak dipole moment. Instead, in many studies the reorientation of polar host molecules is measured [64, 65, 66, 67, 68, 69, 70, 71]. Typical temperature dependent dielectric spectra and the corresponding master curve of 4.2 weight-% anthrone in OTP are shown in figure 5. For comparison, a Debye peak is also shown. Molecular reorientation of different probe molecules has also been studied by optical [72, 73], ESR [74, 75] and NMR spectroscopy [76].

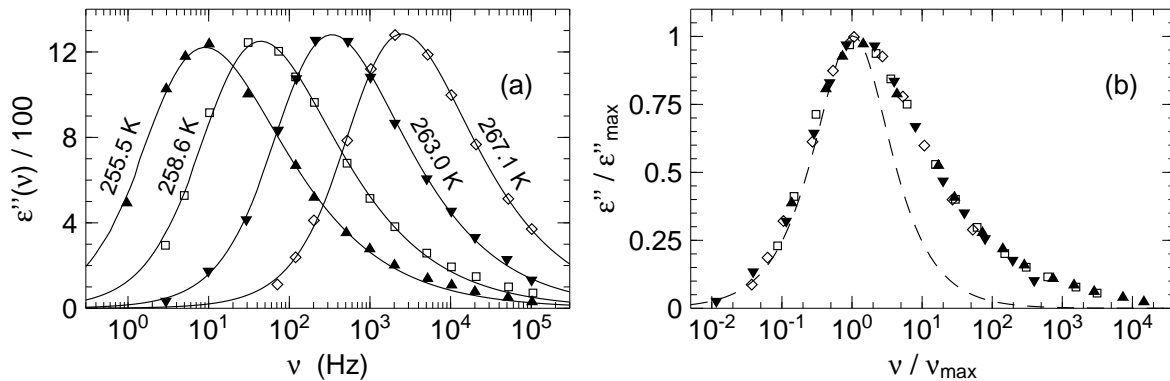


Figure 5. (a) Dielectric loss of 4.2 weight-% anthrone in OTP. Data are scanned from [64] and re-fitted with a Fourier transformed Kohlrausch function. The exponent β seems to increase systematically from 0.52 at 255.5 K to 0.57 at 267.1 K. — (b) Nevertheless, in a good approximation, all data can be condensed onto a master curve. Same symbols as in (a). For comparison, the dashed line shows a Debye peak.

In figure 6 some published values of the Kohlrausch stretching exponent β are compared. For a given experimental probe, β increases systematically with temperature in this temperature range. Thus, the time-temperature superposition (3) only holds in a first approximation and in a limited temperature range. In addition, for any given temperature, different experiments see different exponents β although approximate values of β seem to be correlated with other characteristics of the glass transition dynamics [78, 79].

3.3. Temperature and Pressure Dependence of the α -Relaxation Time

We have seen that the characteristic time (or frequency) of structural relaxation strongly depends on temperature and pressure. Cooling OTP by only 5 K can slow down the decay of the correlation function by a factor of ten or more, as shown in figures 4 and 5.

Figure 7 demonstrates that over many decades the characteristic time τ observed by different spectroscopic techniques follows the same temperature and pressure dependence, although at a given temperature or pressure the absolute values of τ may differ. This finding is confirmed by measurements on many other glass formers.

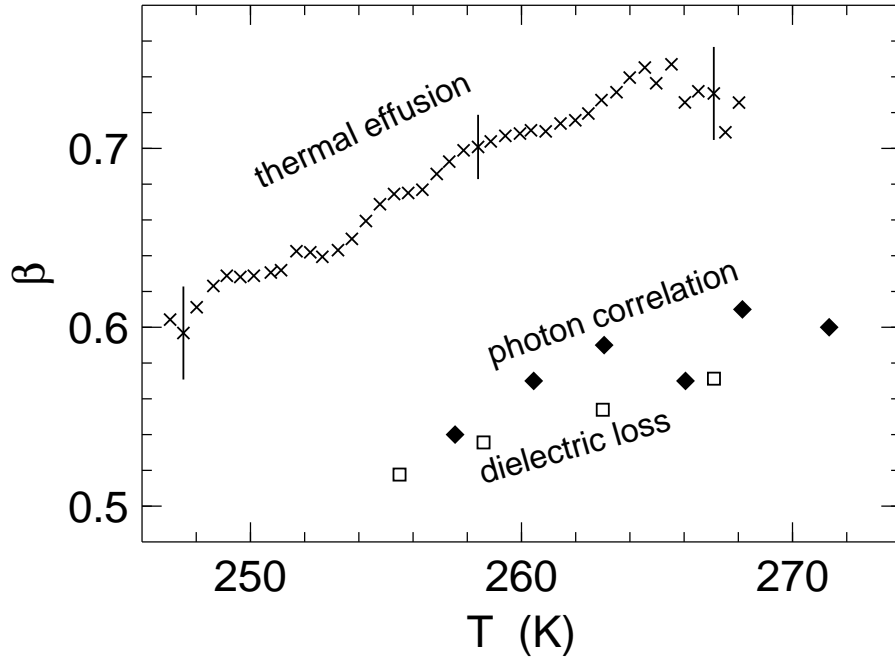


Figure 6. Stretching exponent β from Kohlrausch fits to thermal effusion (\times , OTP with 9% o-phenyl-phenol [77]), photon correlation (\blacklozenge [47]), and dielectric loss (\square , 4.2% anthrone in OTP, our fits to the data [64] of Fig. 5).

The famous Maxwell relation $\eta = G_\infty \langle \tau \rangle$ connects the shear viscosity η with the relaxation time over the shear modulus at infinite frequency G_∞ . Under the assumption that G_∞ varies only weakly with external control parameters like temperature and pressure, it follows $\eta \propto \langle \tau \rangle$.

Therefore, another operational definition of the glass transition temperature T_g is given via the temperature, where the viscosity η reaches $\eta(T_g) = 10^{12}$ Pa.s. With shear moduli of solids, typically of the order $G_\infty \simeq 10$ GPa, this corresponds to a relaxation time of the order of 100 s. This is the same time scale on that structural relaxation falls out of equilibrium in a caloric experiment (see above).

The Maxwell relation makes it possible to determine the temperature or pressure dependence of the structural relaxation time beyond the frequency range of any spectroscopic technique. In fact, the viscosity of OTP has been measured over more than 14 decades as a function of temperature and pressure [24, 25, 26, 27, 28]. The temperature dependent data at ambient pressure are shown in figure 8 together with viscosities of other glass formers in a $\log \eta$ vs. T_g/T representation (Angell plot) motivated by the naïve expectation of thermally activated transport [80]. Although never observed in any real glass former the Arrhenius law $\eta \propto \exp(-E_A/T)$ is taken as a reference to classify the temperature dependence of $\eta(T, P)$.

This classification according to Angell is physical since the curvature in the Arrhenius plot is correlated with the structure of a glass former: *strong* liquids, which

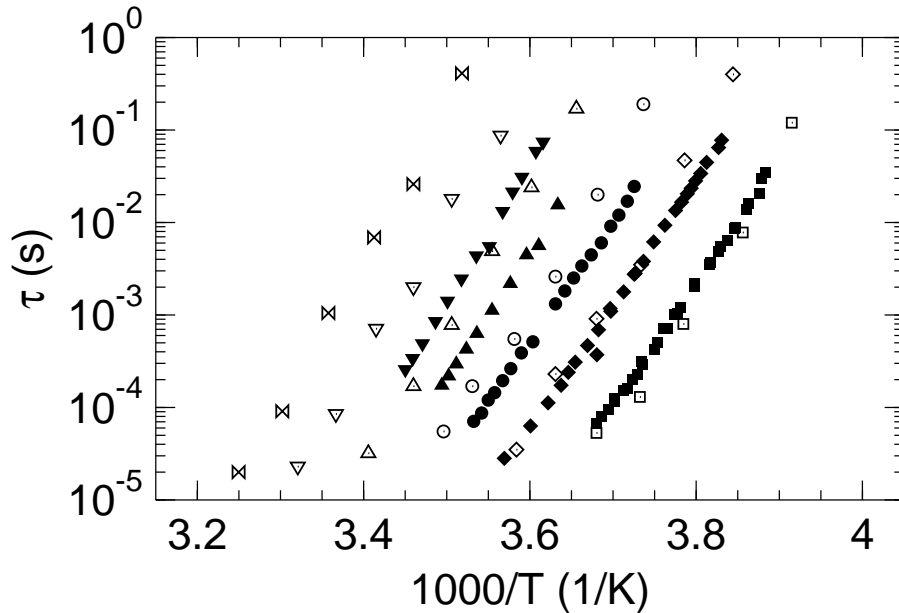


Figure 7. Temperature dependence of the isobaric relaxation time of viscous OTP for pressures between 0.1 MPa and 125 MPa from PCS (open symbols from right to left in steps of 25 MPa) [48] and dielectric spectroscopy (closed symbols from right to left in steps of 19.6 MPa) [60].

deviate only slightly from the Arrhenius law are typically networks like SiO_2 or GeO_2 where the transport is controlled by thermally activated breaking of covalent bonds. Largest deviations are found for molecular liquids, ionic melts and some polymers. They are termed *fragile* liquids. In this classification OTP is one of the most fragile liquids, which is another motivation for its recurrent use as a model system.

From free-volume or entropy arguments [1, 2] it is possible to derive the popular Vogel–Fulcher–Tamman fit formula

$$\eta(T) \propto \exp\left(\frac{A}{T - T_0}\right) \quad (6)$$

with some arbitrary reference temperature $T_0 \ll T_g$. In any case, (6) and similar functions are not able to fit $\eta(T)$ data over the entire temperature range, but they work much better when applied to a restricted range. A critical review of these and other approaches can be found in Ref. [81]. The differential analysis of $\eta(T)$ in the inset of figure 9 is one way to show that the temperature dependence of $\eta(T)$ cannot be described by a single physical model over the whole temperature range. In particular, one recognizes a change of regime at about 290 K. Within mode-coupling theory this is interpreted as a cross-over from liquid-like to hopping dynamics (section 5). For OTP the value $T_c \simeq 290$ K was first determined by strict elastic neutron scattering [82] (section 6.3) and in the meantime it reappeared in many other measurements and simulations, as will be shown throughout this review. In its simplest version, mode-

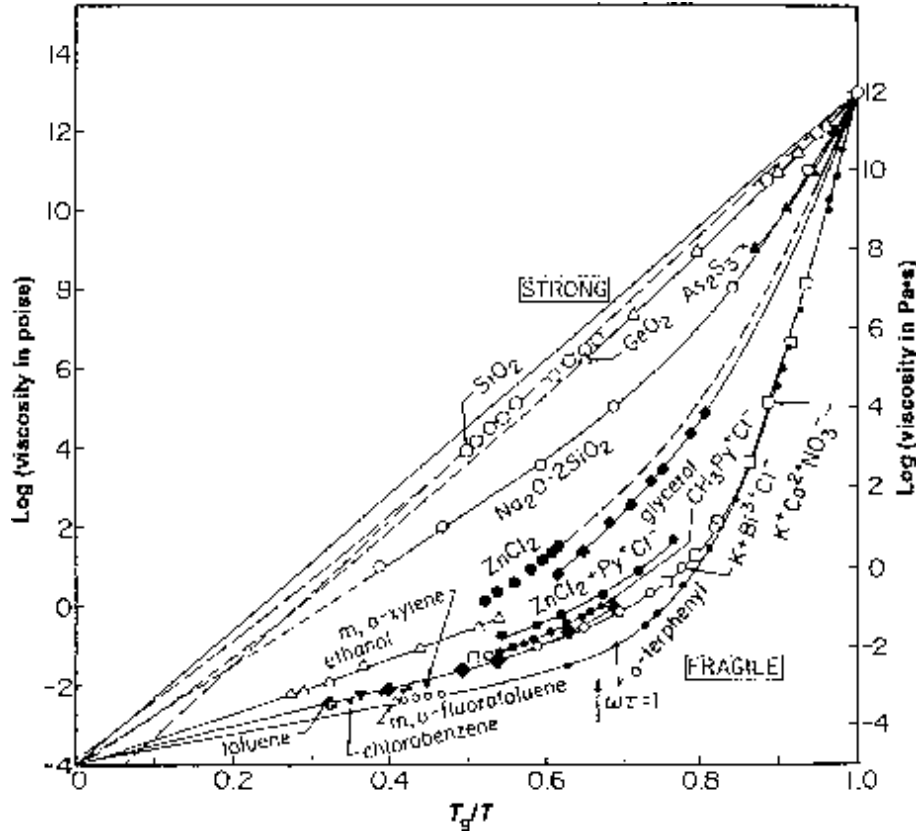


Figure 8. “Angell plot”: Viscosities of various glass forming liquids in an Arrhenius representation with reduced temperature scale T_g/T . This plot motivates Angell’s “strong”—“fragile” classification in which OTP is one of the most fragile liquids. Reproduced from [23].

coupling theory predicts for $T > T_c$ a power law divergence

$$\eta \propto (T - T_c)^\gamma, \quad 1.76 < \gamma < 4.83. \quad (7)$$

Figure 9 shows a three parameter fit of $\eta(T)/T$ yielding a critical temperature $T_c = 290$ K and an exponent $\gamma = 2.59$.

3.4. Diffusion and Decoupling of Time Scales

It is interesting to compare the translational and rotational diffusion coefficients, D_t and D_r , which are integrals over single particle correlation functions, with the shear viscosity η . The shear viscosity depends upon intermolecular momentum transfer through cross correlation functions of neighbouring molecules. In simple van der Waals liquids, the validity of the Stokes–Einstein and the Debye relations,

$$D_t = \frac{k_B T}{6\pi\eta r_S}, \quad D_r = \frac{k_B T}{8\pi\eta r_D^3}, \quad (8)$$

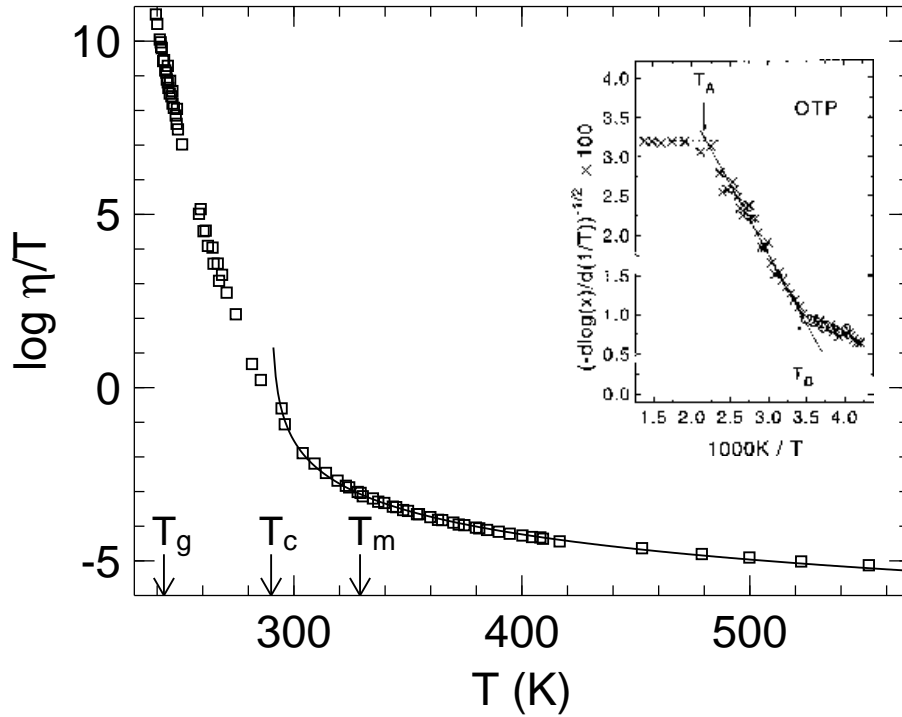


Figure 9. Temperature variation of $\eta(T)/T$. The solid line is a free fit of a power law $(T - T_c)^\gamma$ expected from mode coupling theory yielding $T_c \simeq 290$ K and $\gamma = 2.59$. The arrows indicate the caloric glass transition temperature $T_g = 243$ K, the critical temperature $T_c = 290$ K and the melting temperature $T_m = 329$ K. In the inset (taken from [63]) the temperature dependence of the maximum f_{max} of the dielectric α -process (\circ) and the viscosity $\eta(T)$ (\times) is plotted as $[-d \log(x)/d(1/T)]$. Such a representation linearizes a VFT-type temperature dependence (6) and an Arrhenius behavior appears as a horizontal line. $T_B \simeq 290$ K marks the temperature where the data begin to deviate from a VFT-fit (line). Above $T_A \simeq 455$ K $\eta(T)$ follows an Arrhenius law.

originally derived for a Brownian particle in a viscous liquid, is well established in the fluid regime, although it is a non-trivial fact. The lengths $r_S = 0.21$ nm [83] $\approx r_D = 0.23$ nm [84, 85] are temperature independent and smaller than the geometrical van der Waals radius $r_W = 0.37$ nm [86]. It is most remarkable that D_t and D_r are proportional to η^{-1} in the whole fluid regime.

Rotational self diffusion in neat OTP has been measured by ^2H -NMR stimulated echos [34, 87], translational self diffusion by ^1H -NMR static gradient stimulated echos [34, 88]. Towards lower temperatures, tracer diffusion coefficients of two photochromic tracer molecules having a size comparable to OTP and dissolved in OTP at low concentrations were measured by forced Rayleigh scattering [89]. Results are shown in figure 10.

Rotational self diffusion could be measured almost down to T_g where Debyes' relation (cf. 8) still holds. Apparently, momentum transport is closely connected with

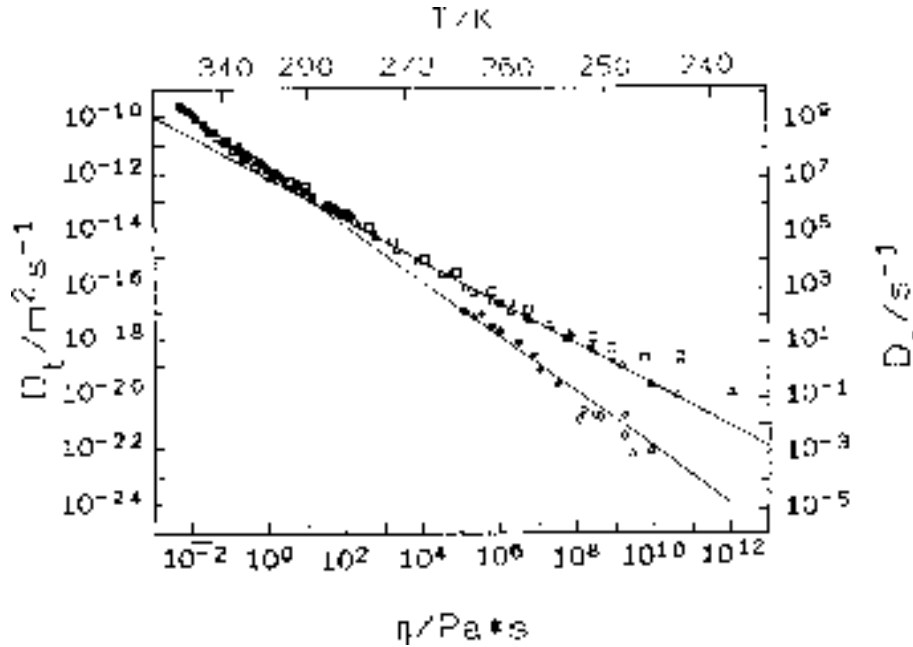


Figure 10. Log-log plot of the translational and rotational diffusion coefficients D_t and D_r of OTP vs. viscosity η and temperature T : translational self diffusion (\bullet); translational tracer diffusion (different photochromic molecules in OTP, Δ , \square); rotational diffusion coefficient (\blacklozenge , \diamond) scaled along $D_t/D_r = 4/3r^2$ (see (8) using $r = 0.22$ nm). The steep line represents the Stokes–Einstein relation $D_t = k_B T / (6\pi\eta r_S)$ using $r_S = 0.22$ nm and fits well the $D_t(\eta)$ data above $T_c \simeq 290$ K and the $D_r(\eta)$ data. The flat line that fits the $D_t(\eta)$ below $T_c \simeq 290$ K has a slope $\eta^{-0.75}$ and crosses the η^{-1} line at 290 K. Reproduced from [90].

molecular reorientations. Translational diffusion, however, *decouples* from rotational diffusion and viscosity and crosses over around $T_c = 290 \pm 10$ K to a weaker temperature dependence approximately given by $D_t \propto \eta^{-0.75}$. Thus, D_t and η behave differently as the mechanism of molecular motion changes from fluid to glass like behaviour. On the other hand, D_r remains proportional to η^{-1} at temperatures down to T_g indicating that rotational motion remains more efficiently coupled to structural relaxation on approaching the glass transition, at least, in fragile glass forming liquids like OTP, toluene [91], salol, glycerin and others [92].

Indications for a cross-over between two distinct dynamic regimes at a temperature T_c above the glass transition temperature T_g have been found for many simple supercooled liquids [93]. A discontinuity for the temperature coefficient of τ/η or $(D\eta)^{-1}$ demonstrates the failure of the Stokes–Einstein relations for $T < T_c$. The existence of the cross-over temperature T_c is further substantiated by a plot of the correlation times on a reduced temperature scale T_g/T , which then shows a bifurcation of the two relevant α and β processes for $T < T_c$.

4. Experimental Method

4.1. Neutron Scattering

In the previous section we have presented a variety of experimental glass transition signatures observed with conventional spectroscopic methods. What can we expect to learn about the glass transition from neutron scattering?

The energy of neutrons of the appropriate wavelength for structural and dynamic studies corresponds to thermal energies for temperatures between a few degrees K to well above room temperature. In fact, neutrons produced from a reactor or spallation source have their wavelength “adjusted” by the equilibration at a given temperature; thus “cold” neutrons have a wavelength of several Å, “hot” neutrons have a wavelength of a fraction of an Å and “thermal” neutrons have a wavelength close to 1 Å. Because of this wavelength–energy link, neutron inelastic scattering allows the simultaneous study of spatial structure, on the one hand, and dynamics, on the other, at the atomic and molecular level [94, 95, 96, 97].

Neutron scattering experiments on viscous liquids are motivated by the following observations: In amorphous and crystalline solids vibrational excitation frequencies are generally of the order of 1 THz; long wavelength phonon frequencies of sound waves are found in the GHz to THz region depending on the wave number Q [95, 96]. Furthermore, the mean relaxation time in normal fluids is typically of the order of 1 ps [97]. Thus, for the observation of the onset of the glass transition – when relaxational motions decouple from vibrational ones – we have to look at the GHz to THz range which is traditionally the domain of scattering experiments. Such high frequencies are nowadays accessible with many experimental techniques like e. g. dynamic light scattering, inelastic X–ray scattering, quasielastic neutron scattering, dielectric spectroscopy or impulsive stimulated light scattering (section 4.3). However, not all of these techniques have been applied to OTP.

Neutron scattering remains one of the most versatile methods for the study of the fast dynamics. It can be used in almost every type of material since it does not depend on optical transparency, dipole moments or polarizabilities [96]. In neutron scattering one observes excitations at a well defined momentum transfer \mathbf{Q} of the order of several Å⁻¹, *i. e.* microscopic motion on interatomic and intermolecular distances can be resolved.

The observed quantity is the so called dynamic structure factor $S(\mathbf{Q}, \omega)$ and is a well defined correlation function [94, 95, 96, 97]

$$S(\mathbf{Q}, \omega) = \frac{1}{N} \int \frac{d\omega}{2\pi} e^{i\omega t} \sum_{j,k=1}^N \langle e^{i\mathbf{Q}\mathbf{R}_j(0)} e^{-i\mathbf{Q}\mathbf{R}_k(t)} \rangle, \quad (9)$$

which couples directly to the nuclear coordinates $\mathbf{R}_j(t)$. It therefore provides an ideal link between experiment and theory as $S(\mathbf{Q}, \omega)$ is the space–time Fourier transformation of the well know van Hove correlation function $G(\mathbf{r}, t)$ [98].

Equation (9) is based on the *coherent* superposition of partial waves scattered by pairs of nuclei j, k . The coherence can be diminished by spin flips except when both

Table 1. Neutron scattering cross sections for incoherent and coherent scattering and absorption cross section in barn ($=100 \text{ fm}^2$) [102].

atom/molecule	σ_{inc}	σ_{coh}	σ_{abs}
H	80.27	1.76	0.33
D	2.05	5.59	0.00
C	0.00	5.55	0.00
OTP- d_0	1123.8	124.5	4.62
OTP- d_{10}	341.6	162.8	1.32
OTP- d_{14}	28.7	178.2	0.00

partial waves are scattered by the same nucleus $j = k$. This leads to an additional *incoherent* scattering

$$S_{\text{inc}}(\mathbf{Q}, \omega) = \frac{1}{N} \int \frac{d\omega}{2\pi} e^{i\omega t} \sum_{j=1}^N \langle e^{i\mathbf{Q}\mathbf{R}_j(0)} e^{-i\mathbf{Q}\mathbf{R}_j(t)} \rangle, \quad (10)$$

which contains valuable information about tagged-particle motion.

In an actual experiment one measures always the sum of both contributions

$$S_{\text{exp}}(\mathbf{Q}, \omega) = \sigma_{\text{coh}} S_{\text{coh}}(\mathbf{Q}, \omega) + \sigma_{\text{inc}} S_{\text{inc}}(\mathbf{Q}, \omega). \quad (11)$$

Incoherent and coherent scattering can be separated by a polarization analysis [99, 100] which is based on the different scattering cross sections for spin-flip $\sigma_{\uparrow\downarrow} = 2/3\sigma_{\text{inc}}$ and non-spin-flip $\sigma_{\uparrow\uparrow} = \sigma_{\text{coh}} + 1/3\sigma_{\text{inc}}$

$$\begin{aligned} S_{\uparrow\uparrow}(\mathbf{Q}, \omega) &= \sigma_{\text{coh}} S_{\text{coh}}(\mathbf{Q}, \omega) + \frac{1}{3}\sigma_{\text{inc}} S_{\text{inc}}(\mathbf{Q}, \omega), \\ S_{\uparrow\downarrow}(\mathbf{Q}, \omega) &= \frac{2}{3}\sigma_{\text{inc}} S_{\text{inc}}(\mathbf{Q}, \omega). \end{aligned} \quad (12)$$

Although this implies a considerable loss in neutron flux in high resolution experiments such experiments are indeed feasible as shown below.

In practice, most often one concentrates on either incoherent or coherent scattering by choosing appropriate samples. In organic samples like OTP, the total cross section is largely dominated by incoherent scattering from hydrogen (table 1). Mainly coherent scattering can be measured on perdeuterated OTP- d_{14} . Partial deuteration has been employed to hide the lateral phenyl rings [101] (section 6.3).

The spectrometers used for neutron scattering on OTP are listed in table 2. They belong to basically five types [103] and are all located at the Institute Laue-Langevin in Grenoble, France. Three of them measure $S(\mathbf{Q}, \omega)$, one the so called intermediate scattering function $S(\mathbf{Q}, t)$ which is the Fourier transform of $S(\mathbf{Q}, \omega)$ and one spectrometer works without energy analysis:

- Triple-axis spectrometers (IN12) are instruments which can measure the four dimensional dynamic structure factor $S(\mathbf{Q}, \omega)$. In single crystals the phonon dispersions relations $\omega(\mathbf{Q})$ can explicitly be measured.

- Time-of-flight (TOF) spectrometers with multichopper (IN5) or crystal (IN6, D7) monochromators where the energy of the scattered neutrons is measured by the time they need to travel a certain distance are used to measure vibrational dynamics as well as fast relaxation.
- Back-scattering (BS) spectrometers achieve high energy resolution by (nearly) 180° Bragg scattering from both the monochromator and the analyzer crystals. They are used to measure the amplitude of elastic scattering and the onset of the slow relaxation. In order to measure full spectra the incident energy is changed either by Doppler shifting the neutron wavelength (IN10, IN16) or by thermal expansion of the monochromators (IN10, IN13).
- Neutron spin-echo (NSE) instruments (IN11) require by construction the use of polarized neutrons. They profit from the fact that the magnetic moment of the neutron undergoes Larmor precessions in a homogeneous magnetic field. This is used to encode the neutrons' energy in the number of Larmor precessions. The polarization analysis of the scattered neutrons amounts to an implicit Fourier transform of the scattering function $S(Q, \omega)$ and has a much larger dynamic range as frequency domain spectrometers at the cost of a lower contrast.
- Diffractometers (D7, D20) are used to measure the static structure factor of liquids and amorphous solids. The integration over all energies is intrinsically performed. In addition to a time-of-flight option, D7 can perform a polarization analysis and is thus able to measure simultaneously incoherent and coherent scattering.

For isotropic samples like powders, liquids and glasses we can only access $Q = |\mathbf{Q}|$.

4.2. Data Evaluation and Limitations

To obtain the desired quantity $S(Q, \omega)$ from the measured scattering intensities several standard corrections have to be performed like normalization to the incoming flux and to the scattering of a vanadium standard, subtraction of container scattering and background noise and, if necessary, calculation of attenuation and absorption effects and conversion to energy.

Since all instruments measure at given scattering angles θ a conversion to the physically interpretable wave number Q has to be done. In figure 11 we show the dependence of the wave number Q on the energy transfer ω for several scattering angles $2\theta = 0 \dots 180^\circ$. For backscattering and neutron spin-echo instruments, where the energy E_i of the incident neutrons is much larger than the energy transfer ω the momentum transfer Q at a given scattering angle is essentially constant (left panel). However, when the energy transfer ω is of the order of E_i – for instance in time-of-flight spectroscopy – then the dependence of Q on ω cannot be neglected (right panel) although sometimes still done [104].

In any substance, one observes at intermediate temperatures significant contributions to $S(2\theta, \omega)$ up to several 10 meV. Before calculating a Fourier transform to get $S(Q, t)$, $S(2\theta, \omega)$ has to be interpolated to $S(Q, \omega)$. As illustrated in figure 11,

Table 2. Neutron spectrometers used in our studies of the statics and dynamics of OTP summarized in this review. All instruments are located at the Institute Laue–Langevin in Grenoble and use cold neutrons except IN13 which uses thermal neutrons. Only IN12 is a single detector instrument, on all other instruments use multidetector banks which cover a wide range of scattering angles. The energy resolution δE varies with detector angle and chosen incoming wavelength λ_i . Often quasielastic scattering data are analyzed by Fourier deconvolution and the approximative time ranges are given. The spin-echo spectrometer IN11 measures directly in the time regime and can be operated with a single- or a multidetector.

Instrument	type	λ_i (Å)	δE (μeV)	Fourier time (psec)
IN5	time-of-flight	5.7–7.5	25–40	0.2 – 35
IN6	time-of-flight	5.1	80–120	0.1 – 10
IN10	back-scattering	6.27	1–3	200 – 2000
IN11	spin-echo	5.5–6.0	–	1 – 2200
IN12	triple-axis	1.55 (k_f)	300	–
IN13	back-scattering	2.23	8–10	10 – 200
IN16	back-scattering	6.27	1	100 – 2000
D7	time-of-flight	4.8	150	0.2 – 5
D7	diffractometer	4.8	–	–
D20	diffractometer	0.82	–	–

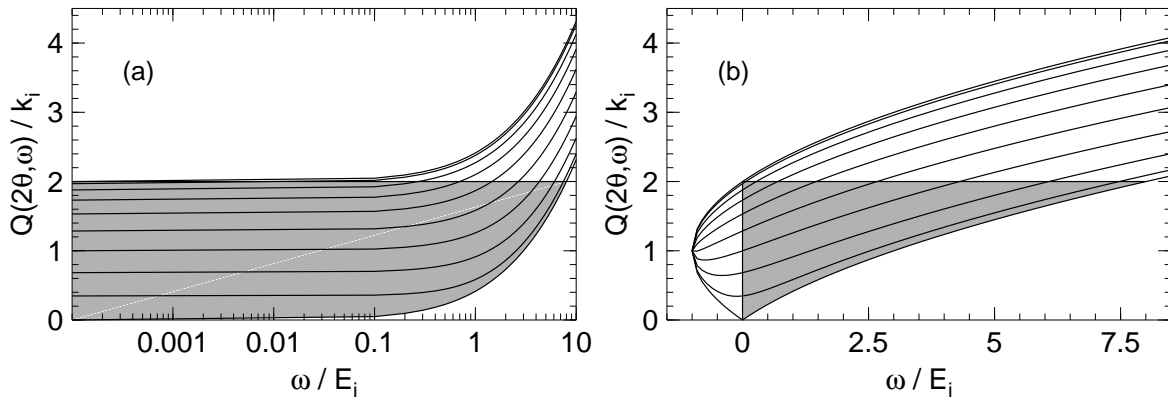


Figure 11. Maximum dynamic range of neutron scattering: (a) on a logarithmic energy scale to emphasize the small energy transfer region typical for BS or NSE instruments and (b) on a linear energy scale to emphasize the large energy transfers typical for TOF instruments. The lines display the frequency dependence of the wave number $Q(2\theta, \omega)$ for several scattering angles ranging from 0° to 180° in steps of 20° from bottom to top. In any real experiment the subregion depends on the largest and lowest scattering angle accessible by each individual instrument. Only the data along a $Q = \text{const.}$ -line in the gray hatched subregion can be used when interpolated spectra $S(Q, \omega)$ are Fourier transformed. The vertical line $\omega = 0$ is the lower energy bound as the elastic channel is needed for the FT. At a given wave number Q the highest accessible energy is restricted and limited by the lowest scattering angle θ_{min} .

this imposes restrictions upon the accessible energy transfers. The Fourier transform $S(Q, t)$ can only be evaluated if the frequency spectrum includes the elastic channel $\omega = 0$. The truncation problem at ω_{\max} is mathematically solved by a multiplication with the step function and leads to a lower bound in Fourier time t below that the Fourier transform is not reliable [105]. The truncation effect may also appear in $S(Q, t = 0) = 2 \int_0^\infty d\omega S(Q, \omega)$ which is then less than the true static structure factor $S(Q)$. Calculating the density and tagged-particle correlation function $\Phi(Q, t)$ from the dynamic structure factors

$$\Phi(Q, t) = S_{\text{coh}}(Q, t)/S_{\text{coh}}(Q) \quad \text{and} \quad \Phi^s(Q, t) = S_{\text{inc}}(Q, t). \quad (13)$$

might then lead to a wrong normalization. For incoherent scattering this problem can be circumvented by measuring $S(Q, \omega)$ at low temperatures where the scattering is totally elastic and $S(Q) = 1$. For coherent scattering this is not possible as $S(Q)$ strongly depends on temperature and pressure. Note, that the truncation effect depends on Q and on the dynamics of the studied system itself and that two competing effects are operative: With decreasing Q the accessible energy range gets narrower (see figure 11), but at the same time the quasielastic broadening and the inelastic intensity decrease as well. Though, while it is straightforward to measure a plateau or a decay of the correlation function it is rather difficult to determine its absolute value within a few percent. The truncation effect can be studied using several upper cut-off frequencies and is in general negligible at least for intermediate and large wave numbers Q .

The determination of the dynamic structure factor in absolute units is further complicated by the inevitable presence of multiple scattering. Multiple scattering is basically a convolution of the dynamic structure factor $S(Q, \omega)$ with itself. The correction for it is far from being a standard data treatment. In the inelastic spectrum, most multiple scattering intensity comes from elastic-inelastic scattering histories [106]. This contribution is nearly isotropic and therefore weakest at large scattering angles. It tends to smear out the characteristic Q dependence of the scattering, and dominates at small angles where the single-scattering signal is expected to vanish as Q^2 .

There are several different approaches to correct for this effect. One can perform a Monte-Carlo simulation of the neutron histories in an effective way [107]. In order to calculate the fraction of multiply scattered neutrons at one point (Q, ω) one has, in principle, to know the ideal scattering in the whole (Q, ω) -space in absolute units. As can be seen in figure 11 only part of it is experimentally covered. Therefore, one needs a physical model for the ideal scattering including Q - and temperature dependences. This makes the correction even more complicated for coherent scattering where elastic, quasielastic and inelastic scattering are oscillating functions of Q .

A new experimental, model independent, however very time consuming approach for multiple scattering correction in inelastic neutron scattering consists in the use of a set of different incident neutron wavelengths in connection with Monte Carlo simulations [108]. Combining data at different wavelengths one can reliably establish an ideal, single scattering function in a wide Q range which then serves as an input to the simulation

followed by a self-consistent, iterative correction.

Another possibility at least for incoherent scattering is to expand the scattering function $S(Q, \omega) = A(\omega) + Q^2 B(\omega) + \dots$ which enables us to estimate the multiple scattering $A(\omega)$ by $Q^2 \rightarrow 0$ extrapolation from the $S(2\theta(Q, \omega), \omega)$ spectra however, loosing the elastic channels [36]. In practice, one often uses thin samples with high transmissions of the order of 90% and more. Then multiple scattering is in general neglected at least at high scattering angles [107].

Recently, an alternative approach has been worked out. By extensive Monte Carlo simulations on very simple models some generic trends of multiple scattering were identified [109]: it distorts the wave number dependence much more than the frequency dependence of $S(Q, \omega)$.

Neutron scattering is always a compromise between the desired statistics, the wave number resolution and coverage, the elastic energy resolution and the accessible energy window. Apart from notoriously lacking statistics, one major problem in neutron scattering is that practically all high resolution spectrometers lack dynamic range. It is known that in order to measure the dynamics of supercooled liquids and glasses properly one has to cover several decades in frequency or time. Several approaches (partly) overcome this problem: (i) the use of master functions obtained by scaling procedures like the time-temperature superposition and / or (ii) the combination of data from different spectrometers with overlapping time ranges. Over the years we have been using both approaches. Elastic resolution effects can be corrected in the $S(Q, t)$ representation by division with the Fourier transformed resolution function (Fourier deconvolution) that has been measured at very low temperatures either on the sample itself or on a Vanadium standard.

Neutron spin-echo spectrometers which measure directly in time domain have a rather large dynamic range of about 3 decades and more, depending on the scattering angle and the incoming wavelength [103]. However, the concomitant shortcuts are low countrates and low Q resolution compared to multidetector instruments. Recently, a multidetector (42 detectors) has been installed on the NSE instrument IN11 covering about 40° . Now, by binning several detectors at least the statistical quality can be improved. The Q resolution is still implicitly limited by the transmission band of the velocity selector of typically $\Delta\lambda/\lambda \simeq 10\%$ leading directly to $\Delta Q/Q \gtrsim 10\%$. One should be aware that in such a case one measures averages $\langle \Phi(Q, t) \rangle_Q$ over correlation functions. Increasing the Q resolution by a narrower band width using for example a graphite monochromator leads to an unacceptable reduction in intensity.

Improvements of neutron sources [110, 111] to increase the incoming flux and of instrumental performance [112] to increase the efficiency are currently under way. In order to test the new developments and extentions of the theory (section 5.4) experimentally or to attack even new questions the dynamic range and concomitantly the Q -resolution and the Q -coverage have to be enhanced.

Let us demonstrate to which extent it is desirable to push improvements for a real progress. As an example we show in figure 12 the tagged-particle and the density

dynamic structure factor of OTP measured in the only proper way by polarization analysis on the instrument D7 at the ILL. Currently, D7 is the only multidetector instrument in the world which is able to separate the energy resolved incoherent and coherent scattering from one sample. Some triple-axis spectrometers can do polarization analysis as well, however, are equipped with a single detector only. On each other instrument one always measures both contributions which are differently weighted depending on the spectrometer type. This possibility is particularly interesting for some

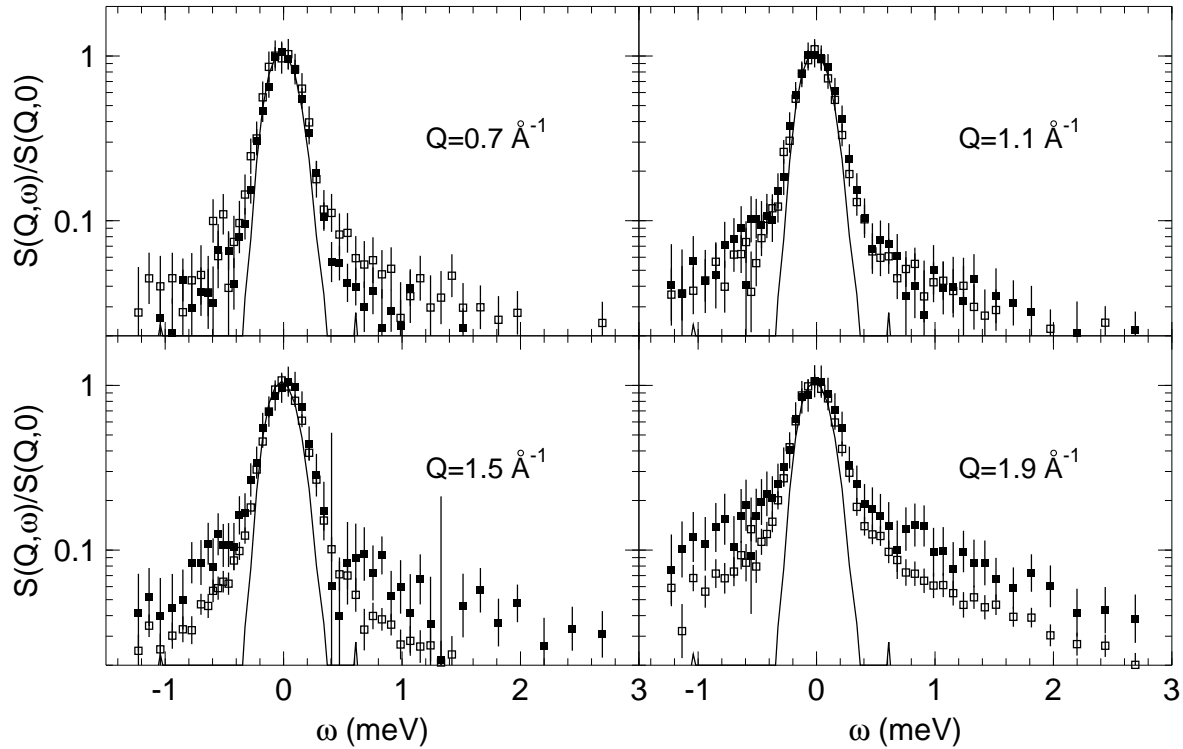


Figure 12. (*) Coherent (open symbols) and incoherent (full symbols) dynamical structure factor $S(Q, \omega)$ of OTP for several values of Q at 340 K as measured on D7 with polarization analysis. Note the different quasielastic scattering for different Q .

important questions not only in glass science which have not been studied up to now. For example, it would be possible to study exclusively the center-of-mass (COM) motion of OTP. Measuring the incoherent scattering of OTP- d_{10} where only the lateral phenyl rings are deuterated gives access to the tagged-particle correlation function of the COM motion. Conversely, measuring the coherent scattering of central ring deuterated OTP- d_4 would lead to the density correlation function of the COM motion. At the same time, important information can be gained from the coherent scattering and the incoherent scattering of the lateral phenyl rings in OTP- d_{10} and OTP- d_4 , respectively, about e. g. relaxational modes and their time scales or vibrational excitations of intramolecular motions.

Furthermore, it would also be possible to compare both structural relaxation times

and their Q dependence in the context of recurrent used models like “de Gennes” narrowing [113]. The advantage is evident: such studies could be performed on one and the same sample under exact identical experimental conditions.

The spectra shown in figure 12 were obtained under fairly optimized experimental conditions. Nevertheless, although the transmission of 67% was extremely low and the energy resolution rather moderate data accumulation took about 42 h! Such test experiments make it clear that, for example, increasing the incoming flux by a factor of two while leaving the instruments as they are is far too less. The total efficiency which is a product of the source strength, the transport efficiency and the instrument efficiency has rather to be increased by orders of magnitudes [112].

4.3. Other Experimental Approaches

In section 3 we have already presented many experimental techniques probing the glass transition phenomena and the slow structural relaxation of OTP. Therefore, we limit ourselves to a short enumeration of those other experimental approaches that probe the fast dynamics in the GHz – THz band and have been applied to OTP.

Light scattering spectroscopy has been often employed in OTP and many other supercooled liquids and glasses. Raman scattering has primarily been performed in connection with the Boson peak and the study of the vibrational dynamics of the glassy and polycrystalline state [114, 115, 116]. Brillouin scattering explores the longitudinal (LA) and transverse (TA) acoustic modes in the GHz range and their interaction with the structural relaxation [117, 118, 119]. Inelastic X-ray scattering extends the Q - ω range of the conventional Brillouin technique and makes it possible to study sound waves on intermolecular distances and in the THz range [120, 121, 122]. Depolarised light scattering using geometries in which the usual LA and TA Brillouin components are forbidden is the most often used method to study the sub GHz to THz dynamics [53, 123, 124, 125, 126, 127]. Although the scattering mechanism and the connection to density fluctuations are still debated [128] the experimental results have often been compared to mode-coupling theory. A promising development covering about 5 orders of magnitude in time is actually taking place using the optical Kerr effect in terms of a pump-and-probe experiment [129, 130].

Computer simulation yield $\Phi(t)$ as primary output. In recent Monte-Carlo [131] and molecular dynamics [132, 133] studies the time range was extended to such long times, that they now deal with the same windows as achieved by the above mentioned modern experiments. In molecular dynamics simulations many different observables can be studied which are not accessible by any other experimental methods. The data quality is so good that the results can be compared with more sophisticated mode-coupling models and with numerical solutions of the mode-coupling equations, where the static structure factor is the only input. However, simplified models have to be used approximating the real molecule [35, 134, 135, 136, 137, 138]. The need for extending the simulations to times long enough to follow the relaxation processes in the supercooled

and glassy state still necessitates a compromise with respect to the complexity of the model and the number of interaction sites. Lewis and Wahnström used a three-site model mimicking OTP, where each phenyl ring was treated as a single interaction site [134, 135, 137]. Although simple, this model essentially reproduces the dynamics of OTP, in particular the anomalous behaviour of the Debye–Waller (Möbbaauer–Lamb) factor and the existence of a fast motional process. Later, Scortino *et al.* extended the calculations of Lewis and Wahnström by more than one decade towards longer times [138]. In addition to the translational correlation functions the rotational ones were calculated and compared with theory. However, the planar nature of model makes it easier for the molecules to slide past one another. The 18-site, three-ring model of Kudchadkar and Wiest [136] and later of Mossa *et al* [35] takes into account the three-dimensional nature of the OTP molecule and may provide a better representation of the reorientational dynamics. In addition it retains some internal torsional motions of the lateral rings with respect to the central one. However, with the extended complexity only a few number of molecules could be simulated and the time range is rather limited.

5. Mode–Coupling Theory

5.1. Aim

The dynamics of normal simple liquids is governed mainly by excluded volume and binary collisions between molecules which, at high temperatures or low density become more and more statistically independent from each other. It can be described by generalizing the kinetic equation of Boltzmann. When the liquid is densified it is clear that this description breaks down at some point, as the binary collision events become highly correlated. This gives rise to two well known phenomena: the back–flow and the cage effect. Suppose a tagged–particle is trapped in a cage formed by its nearest neighbours which are caged themselves. On a short time scale the only possible motion is a rattling in this cage. The particle cannot escape and move over distances larger than the next neighbour distances. These correlated collisions in the cage lead to a strong damping of the motion and correspond to an increasing friction. On longer time scales and for transport over longer distances the cage must open which requires a cooperative rearrangement of many particles. For large densities the cage forming particles are subject to the same dynamics as the particle in the cage, *i. e.* all fluctuations have to be treated on the same level.

It is the essence of the mode–coupling theory of the glass transition (MCT) that it indeed deals with the two phenomena cited above. Its advent has highly stimulated many discussions and experiments. MCT describes the evolution of structural relaxation in simple liquids. The cage effect is responsible for the slowing down of the dynamics of supercooled liquids and drives the system towards an ergodic–nonergodic transition at some critical temperature $T_c > T_g$ or some critical density $n_c < n_g$. A smooth cross–over from vibrations to structural relaxation is predicted as a new dynamic feature – the β –relaxation. At some point the back–flow effect counterbalances the cage effect and allows the system to stay ergodic until it drops finally out of equilibrium at the caloric glass transition.

In the following we briefly recall the analytical solutions of the mode–coupling theory as derived for the idealized case as far as necessary for the interpretation of the experimental data in sections 6 and 7. It is expected that the essential features of the idealized theory above T_c (or below n_c) prevail in real systems [139]. While the analytical solutions for the idealized theory provide handy fit formulars, numerical solutions of the mode–coupling theory can only hardly be used to analyze the experimental data. The most adequate for our purpose is the formulation of the results in the time.

5.2. Equations of Motion

Starting point of the original (referred to as simplified or idealized) version of MCT is a generalized Langevin equation of motion for the normalized density fluctuation correlator $\Phi_Q(t) = \langle \rho_Q(0)\rho_{-Q}(t) \rangle / \langle \rho_Q(0)\rho_{-Q}(0) \rangle$, where $\rho_Q(t)$ is the Fourier component

of the density fluctuation:

$$\partial_t^2 \Phi_Q(t) + \nu_Q \partial_t \Phi_Q(t) + \Omega_Q^2 \Phi_Q(t) + \Omega_Q^2 \int_0^t dt' m_Q(t-t') \partial_{t'} \Phi_Q(t') = 0. \quad (14)$$

The set of integro-differential equations can be closed using Kawasakis factorization approximation. The kernel $m_Q(t)$ is expressed in terms of products of correlation functions (called the mode-coupling approximation):

$$m_Q(t) = \sum_{k_1+k_2=Q} V(Q; k_1, k_2) \Phi_{k_1}(t) \Phi_{k_2}(t) = \mathcal{F}_Q(V, \Phi_k(t)). \quad (15)$$

The internal control parameters V representing the strength of the coupling of different density modes are controlled by the external control parameters like temperature T or density n via the static structure factor $S(Q; n, T)$. They can be calculated from the interaction potentials and vary smoothly with wave number Q and all external control parameters. Changing the temperature or the pressure, a dynamic phase transition from a liquid to a glass occurs at a critical value V_c called the glass transition singularity. In the vicinity of a particular value V_c a characteristic slowing down of $\Phi_Q(t)$ is found [5, 6]. As it is not accompanied by marked structural changes we deal with a purely dynamic transition.

In most real materials the knowledge of the interaction potentials is too inaccurate to compute the MCT solutions explicitly. However, in the vicinity of the glass transition singularity V_c a number of generic features of the solutions exist and are independent of the detailed form of the coupling constants. Most of the predictions of MCT are obtained from asymptotic expansions in the vicinity of the singularity.

5.3. Solutions of Mode-Coupling Equations

(i) The Square Root Singularity

Denoting the distance from the singularity V_c by the *separation parameter* σ , it follows for the Debye-Waller factor or the nonergodicity parameter $f_Q = \lim_{t \rightarrow \infty} \Phi_Q(t)$ in leading order [140, 141]

$$f_Q(\sigma) = f_Q^c + \begin{cases} \mathcal{O}(\sigma) & : (\sigma < 0, \text{ergodic}) \\ h_Q \sqrt{\sigma} + \mathcal{O}(\sigma) & : (\sigma > 0, \text{nonergodic}) \end{cases} \quad (16)$$

h_Q is called the critical amplitude. Let x be one external control parameter like T or n , then for the glass transition we have $\sigma \propto (x - x_c)/x_c$. This square root cusp in $f_Q(x)$ is an important signature of x_c in the MCT.

The Debye Waller factor can easily be measured by elastic neutron scattering. In practice, due to the finite instrumental resolution δE it is impossible to measure strictly elastic scattering $\omega = 0$. All scattering events within δE appear elastic. Therefore, an effective nonergodicity parameter f_Q is used which corresponds to the replacement of $f_Q \delta(\omega)$ by the area under the α peak or equivalently by the plateau height of the correlation function $\Phi_Q(t \simeq \hbar/\delta E)$.

(ii) *The β -Relaxation*

Let us now turn to the dynamic behaviour of the density correlation function $\Phi_Q(t)$ in the vicinity of the dynamic phase transition. The existence of a β -relaxation with a critical spectrum is probably the most important result of MCT. It concerns the mesoscopic time range between the microscopic short time dynamics determined by Ω_Q and the α -relaxation dynamics at long times. This time range corresponds to the frequency range around the minimum in the susceptibility spectrum $\chi''(\omega)$ separating the microscopic peak from the low frequency α -relaxation peak. In the ideal version of MCT the shape of $\Phi_Q(t)$ in this region is completely determined by a separation parameter σ and a material dependent constant λ .

Strong predictions are made in the β -relaxation regime, the external control parameters being sufficiently close to the critical point. For $t_0 = \Omega_Q^{-1} \ll t \ll \tau$ and for $|x - x_c|$ sufficiently small the correlators $\Phi_Q(t)$ stay close to the plateau value f_Q^c . The equation of motion (14) can then be asymptotically developed in terms of $|\Phi_Q(t) - f_Q^c|$. Note, thereby one implicitly defines a time interval, where $\Phi_Q(t)$ is close to f_Q^c called the β -regime. One obtains in leading order [141, 142]

$$\Phi_Q(t) = f_Q^c + H_Q g_{\pm}(t/t_{\sigma}), \quad (\sigma \gtrless 0). \quad (17)$$

where the amplitude and the cross-over time

$$H_Q = h_Q c_0 |\sigma|^{1/2} \quad \text{and} \quad t_{\sigma} = t_0 |\sigma|^{1/2a} \quad (18)$$

depend critically on the distance from the transition point. c_0 is a material dependent dimensionless constant describing the proportionality between the theoretical and the experimental control parameters.

It is a remarkable property that $\Phi_Q(t)$ factorizes into a purely Q -dependent amplitude H_Q and a purely time-dependent function $g_{\pm}(t/t_{\sigma})$. Applied to the particle density $n(\mathbf{r}, t)$ this means that the variations of the density in space are uncorrelated with those in time.

The scaling function $g_{\pm}(\tilde{t})$ depends only on the line shape parameter λ and can be calculated from the expansion [143]

$$g_{\pm}(\tilde{t}) = \begin{cases} \tilde{t}^{-a} \pm A_1 \tilde{t}^a + A_2 \tilde{t}^{3a} \pm \dots & : \quad (t_0 \ll t \ll t_{\sigma}, \sigma \gtrless 0) \\ -B \tilde{t}^b + B_1 / (B \tilde{t}^b) + \dots & : \quad (t_{\sigma} \ll t \ll \tau, \sigma < 0). \end{cases} \quad (19)$$

The exponents a and b as well as the expansion coefficients A_i and B_i and the cross-over time are tabulated functions of λ . Starting from short times $t \rightarrow t_{\sigma}$, g_{\pm} slowly decays to zero. For times t longer than t_{σ} it changes its sign for $\sigma < 0$ and initiates the further decay of the correlations.

The two non-universal critical exponents a and b are related to the line shape parameter λ via the transcendental equation

$$\frac{\Gamma^2(1-a)}{\Gamma(1-2a)} = \lambda = \frac{\Gamma^2(1+b)}{\Gamma(1+2b)}, \quad 0 < a < 1/2, \quad 0 < a < b < 1 \quad (20)$$

from which follows that $1/2 < \lambda < 1$.

On leaving the plateau region, we obtain from (19) the asymptotic power law

$$\Phi_Q(t) = f_Q - Bh_Q|\sigma|^{1/2}(t/t_\sigma)^b = f_Q - Bh_Q(t/\tau)^b \quad (21)$$

with a new universal time scale

$$\tau = t_0|\sigma|^{-\gamma}, \quad \gamma = \frac{1}{2a} + \frac{1}{2b} \quad (22)$$

which leads up to the final decay of correlations in the α process. Its fractal time dependence is the key to stretching [140]. Eq. (21) is called the von Schweidler law and its region of validity is often rather limited. However, it gives a theoretical explanation of the often observed time–temperature–pressure principle

$$\Phi_Q(t; X) = \Phi_Q(t/\tau(X)), \quad X = T, P, \dots \quad (23)$$

This means in general, that the line shape may still depend on Q but not on X . A change of the external control parameter only causes a rescaling in time.

MCT predicts that the relaxation times τ of all correlators that couple to density fluctuations should show a divergent behaviour near the critical point in the form of a power law with the same universal exponent γ . This property is called the α scale universality. The exponent γ can be calculated once the line shape parameter λ is known and vice versa.

The final decay of the correlations is often parameterized by the Kohlrausch stretched exponential (1). Note, that the Kohlrausch law is not a general solution of the MCT equations. However, it is an asymptotic result in the limit of large wave numbers [144].

(iii) Q -dependence

In the framework of MCT the Q dependence of f_Q, h_Q, A_Q, τ_Q and β_Q is determined solely by the static properties of the system and have so far been determined from numerical solutions of mode–coupling equations for systems like hard spheres [6, 145], Lennard–Jones [146] spheres, and binary mixtures of hard spheres [147] and Lennard–Jones spheres [148].

In the incoherent case, *i. e.* the tagged–particle correlations, f_Q^s reflects the single particle oscillations and it closely corresponds to a Gaussian distribution in space $f_Q^s = \exp(-Q^2 r_s^2)$ [6, 149]. The half width of f_Q^s is inversely proportional to the root–mean–square displacement of a particle. The amplitude h_Q^s starts to increase with a Q^2 behaviour that is also expected from harmonic theory of vibrational excitations in the high frequency low temperature limit.

For the coherent case, *i. e.* the density correlations, the amplitudes f_Q and h_Q reflect the oscillatory character of $S(Q)$ and are found to oscillate in phase and out of phase with the static structure factor $S(Q)$, respectively.

Theory does not claim that the short time expansion of (1) matches exactly (21). However, it makes it plausible that the α -relaxation time τ_Q follows the Q dependence of f_Q/h_Q . The α -relaxation time of the density correlations τ_Q is found to vary strongly around Q_0 , the position of the first structure factor maximum [145]. Such oscillations

of τ_Q are in a more general context known as de Gennes narrowing [113]. Since in general $\beta_Q \neq b$ oscillations in f_Q and h_Q^{-1} should also lead to oscillations in β_Q .

The α -relaxation time of the tagged-particle correlations τ_Q^s decreases monotonously close to a Q^{-2} law while β_Q^s varies monotonically from 1 in the $Q \rightarrow 0$ limit to a constant value in the large Q limit [145].

For both, tagged-particle and density correlations the lineshape parameter λ and the crossover time t_σ are identical and Q -independent.

5.4. Extensions of Mode-Coupling Theory

In the idealized theory below T_c the α -relaxation time τ and the cross-over time t_σ are predicted to diverge at T_c with the viscosity η . However, in reality they stay finite at this temperature. The divergence is due to the overestimation of the cage effect in the approximation used for the memory kernel $m_Q(t)$ (15). In the extended theory α -relaxation and cross-over evolve smoothly with decreasing temperature below T_c . Including the coupling to density currents, *i. e.* products of type $\Phi_Q(t)\dot{\Phi}_Q(t)$ or $\dot{\Phi}_Q(t)\dot{\Phi}_Q(t)$ in (15), lifts the divergence at T_c and the system remains ergodic even below the critical temperature. This so called "phonon assisted hopping" processes counterbalance the cage effect and restore ergodicity at T_c . Thus, the ideal glass transition is replaced by a change of mechanism of motion from liquid-like diffusional motion above T_c to solid-like jump processes below T_c .

The equations and solutions of the extended version are rather involved and we expect that the essential features of the idealized version concerning the β -relaxation prevail. For several glassy systems, in particular OTP, we will see that nature comes very close to the ideal theory.

Equations (19) are the predictions of the theory about the leading asymptotic behaviour for the time and the temperature (or density) dependence of a generic correlator. Recently the next leading order corrections to the asymptotic solutions have been calculated [149, 150]. These corrections lead to some modifications in the *early* β -regime for $t_0 \ll t \ll t_\sigma$, namely

$$\Phi_Q(t) = f_Q^c + h_Q(t_0/t)^a \{1 + [K_Q + \Delta](t_0/t)^a\} \quad (24)$$

with a Q -independent constant Δ and a Q -dependent constant K_Q ; both are temperature independent. In the *late* β -regime the correlation function is now predicted to behave like

$$\Phi_Q(t) = f_Q^c - h_Q(t/\tau)^b \{1 - [K_Q + \Delta'](t/\tau)^b\}. \quad (25)$$

The corrections are the second terms in the curly brackets in (24) and (25). The important result is that the Q dependent correction constant K_Q is the same in both equations. In addition, the constant Δ and Δ' are related with each other. Indications of the existence and the correctness of these corrections have been found in molecular dynamics simulations [151].

The success of mode-coupling theory for simple liquids has stimulated a considerable amount of theoretical work to extend it to molecular liquids. Recent contributions include the extension to the rotational dynamics of a linear molecule immersed into a system of spherical particles [152] and the generalization to molecular liquids of linear and rigid molecules [153]. Using the projection operator formalism an equation of motion is derived for the correlators $S_{lm,l'm'}(Q, t)$ of the tensorial one particle density $\rho_{lm}(Q, t)$, which contains also the orientational degrees of freedom for $l > 0$. Now, the translational and the orientational degrees of freedom freeze in in a different manner and at different critical values and demonstrate a hierarchy for the freezing: the orientational degrees of freedom can never freeze in before the translational degrees of freedom are frozen.

MCT has also been extended to treat the dynamics of full molecular systems using a site-site representation [154]. A further step has been undertaken to describe the orientational and translational dynamics of liquids composed by rigid molecules of arbitrary shape [155].

As in neutron scattering we are unable to unravel the reorientational correlation functions we do not go into detail here. The interested reader is referred to the cited references.

Generally, the mode-coupling approximations (15) are difficult to control as there is no obvious smallness parameter. Thus, MCT predictions have to be checked by comparison with experimental and numerical results. This will be done in the next sections.

6. Temperature Dependent Experiments

6.1. Experimental Considerations

As already mentioned in section 2 the crystallization tendency of OTP requires some care. Our first experiments have been performed with aluminum containers where the temperature range between 245 K and 290 K was inaccessible due to crystallization. Later, the crystallization tendency could be significantly reduced using high purity samples in clean glass capillaries with very smooth container surfaces. For incoherent scattering experiments with OTP- d_0 several hundred soda lime glass capillaries of 0.32 mm inner diameter and 0.04 mm wall thickness were used. For the coherent scattering experiments with fully deuterated OTP- D_{14} below T_m soda lime glass capillaries with an inner diameter of 1.2 mm and a wall thickness of only 10 μm were used. The sealed capillaries were arranged on a circle of an appropriate sample holder whose diameter was adapted to the neutron beam size mimicking a hollow cylinder geometry. This geometry keeps multiple scattering and self-shielding effects relatively isotropic. Furthermore, the use of capillaries allows to check visually for any traces of crystallization. Another positive side effect not considered before: The glass tubes can be used for scattering experiments beyond $Q \geq 2.7 \text{ \AA}^{-1}$ as no Bragg reflection occurs contrary to Al sample holders.

High purity samples were obtained by repeated recrystallization out of a hot methanol solution and subsequent vacuum distillation. Before filling the capillaries were flushed with distilled water to remove dust and baked out at about 850 K for several hours. After filling, the samples were tempered at about 350 K for several days. When left undisturbed at room temperature no crystallization occurred for more than 2 years.

The measured transmission of a collimated beam of the samples was always higher than 90% which is generally regarded as a good compromise between the conflicting requirements of high single scattering and low multiple scattering. Therefore, no attempt has been made to correct for multiple scattering leading to some reservations in particular at low wave numbers, say $Q \lesssim 0.5 \text{ \AA}^{-1}$.

6.2. Static Structure Factor

Although OTP is a relatively simple molecule the static structure factor $S(Q)$ is rather involved [156]. A straightforward connection of the structure factor peaks to single molecular units is no trivial task since the static structure factor $S(Q)$ is a weighted sum of atomic correlations. $S(Q)$ of supercooled deuterated OTP as measured on the diffractometer D20 of the Institute Laue Langevin (ILL), Grenoble, is shown in figure 13. In contrast to atomic systems the main peak of the static structure factor is splitted into two maxima at about 1.4 \AA^{-1} and 1.9 \AA^{-1} . With decreasing temperature a slight shift of the peak positions to higher Q values due to the increase in density n and in addition an increase of the peak height at 1.9 \AA^{-1} is observed. The peak height at 1.4 \AA^{-1} is slightly reduced which is probably connected to the decrease of the isothermal compressibility

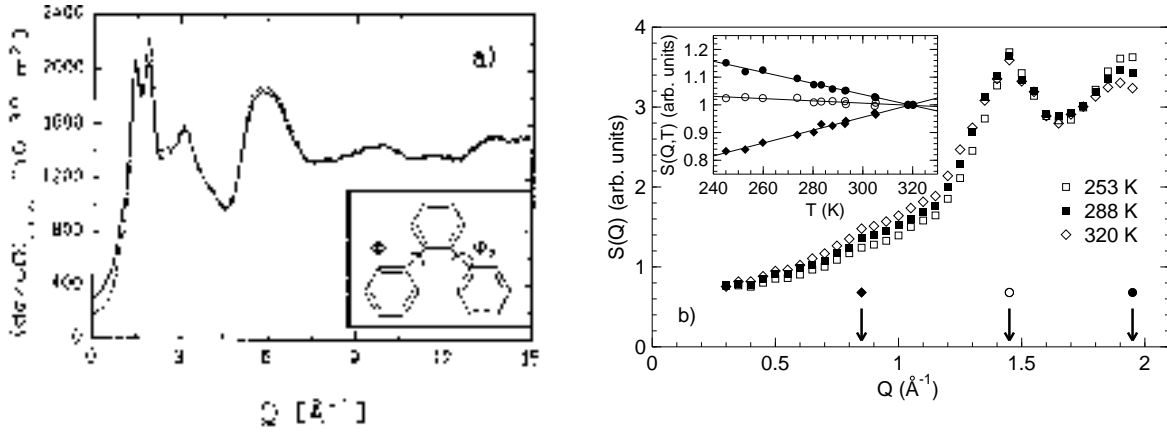


Figure 13. (a) Static structure factor of fully deuterated OTP at 314 K (full line) and 255 K (dashed dotted line) as measured on the neutron diffractometer D20 of the ILL, reproduced from [156]. (b) Static structure factor in the low Q region of deuterated OTP from IN5. Note the appearance of a clear shoulder around $Q = 0.85 \text{ \AA}^{-1}$. The inset shows the temperature dependence of $S(Q)$ at selected Q values which are indicated by the arrows in the figure. $S(Q)$ shows strong temperature variations at $Q = 0.85 \text{ \AA}^{-1}$ and $Q = 1.95 \text{ \AA}^{-1}$. Taken from [42].

$$n\chi_T k_B T = S(Q = 0).$$

Due to experimental limitations the Q region below about 1 \AA^{-1} was not accessible in the D20 experiment. Therefore, we show in the right part of figure 13 the static structure factor $S(Q)$ in the low Q region as measured on the time-of-flight spectrometer IN5 of the ILL [42]. The double peak structure is resolved and the temperature dependence of $S(Q)$ agrees well with the one measured on D20. One recognizes a clear shoulder around 0.85 \AA^{-1} with an increasing peak height with increasing temperature. In inelastic X-ray scattering experiments a real prepeak at $Q \simeq 0.85 \text{ \AA}^{-1}$ was observed [157] together with a main peak at $Q \simeq 1.45 \text{ \AA}^{-1}$ while nearly nothing is found around $Q \simeq 1.9 \text{ \AA}^{-1}$. Note that in neutron scattering on fully deuterated OTP both Deuteron and Carbon atoms are seen with about the same scattering cross sections (cf. table 1), while in X-ray scattering only the distribution of Carbon atoms has to be taken into account.

In simulations simplified models are used for the complex molecule to keep the computing time reasonable. Lewis and Wahnström employed a three site complex, each site playing the role of a whole benzene ring [135]. The static structure factor of the center of mass shows a maximum around $0.8 \dots 1 \text{ \AA}^{-1}$ while the one of the sites is solely peaked at 1.5 \AA^{-1} . A refinement of this model with 18 sites on 3 rings was later studied by Kudchadkar [136]. The static structure factor shown in figure 14 now well reproduces the experimental one, in particular at higher Q including the hump at 3 \AA^{-1} and the prominent peak at 6 \AA^{-1} . For smaller Q it yields, besides a double peak structure at 1.4 \AA^{-1} and 1.5 \AA^{-1} , also a clear shallow peak around 0.8 \AA^{-1} as illustrated in the inset of figure 14. The fact that the second peak of the double peak is at lower

Q than observed experimentally is probably due to the fact of “fusing” the carbon and the attached hydrogen atoms into one “united atom”. In a recent work on a flexible molecule model [35] a good agreement among the molecular dynamics structure factor and that measured by neutron scattering was obtained in the high- Q region. A clear shoulder was observed at 0.9 \AA^{-1} , a diffraction peak at 1.5 \AA^{-1} but no double peak structure, only a small bump around 1.8 \AA^{-1} . Their analysis in terms of a calculated structure factor on the molecular and ring center of mass clearly support our simplified picture that follows below.

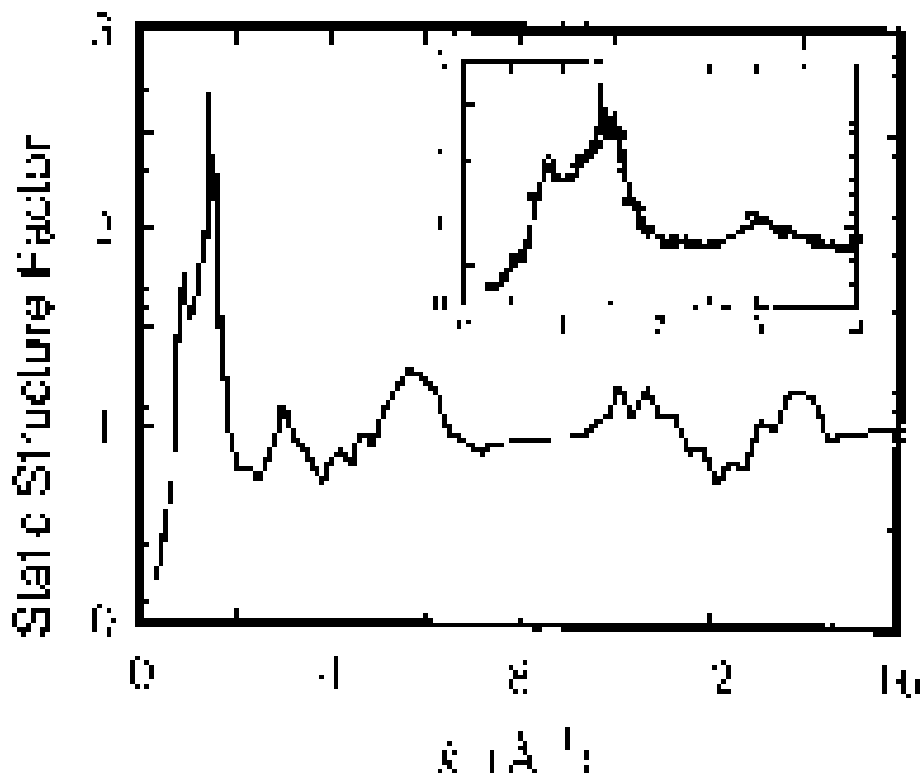


Figure 14. Calculated static structure factor for the 18-site model of OTP. The inset displays the small Q region in more detail. Note the shoulder around $Q = 0.8 \text{ \AA}^{-1}$. Reproduced from [136].

In this context we point out that the structure factors of fully deuterated benzene and hexafluorobenzene, that can be considered as unconnected subunits of OTP are nearly indistinguishable from the one of OTP both showing the double peak at the right positions as well as the hump at 3 \AA^{-1} and 6 \AA^{-1} [158]. Similar double-peak structures are found even in similarly simple phenyl systems like *m*-fluoroanilin [159].

In this context we point out that the structure factors of fully deuterated benzene and hexafluorobenzene, that can be considered as unconnected subunits of OTP are nearly indistinguishable from the one of OTP both showing the double peak at the right positions as well as the hump at 3 \AA^{-1} and 6 \AA^{-1} [158]. Similar double-peak structures are found even in similarly simple phenyl systems like *m*-fluoroanilin [159].

The following simplified picture may therefore be developed: The peak at $Q_2 \simeq 1.9 \text{ \AA}^{-1}$ is probably built up mainly by correlations within the phenyl rings, while the maximum at $Q_1 \simeq 1.45 \text{ \AA}^{-1}$ might be associated with correlations between phenyl rings. The shoulder around $Q_0 \simeq 0.85 \text{ \AA}^{-1}$ is presumably the most direct manifestation of intermolecular correlations [35, 135, 136]. Its position is indeed compatible with the inverse van der Waals radius of $r_W = 3.7 \text{ \AA}$ [86]. We don't believe that the shoulder in OTP is due to pure orientational correlations that can lead to a prepeak at low Q [160].

6.3. Square Root Singularity

The first experimental indications of an anomalous behaviour of the Debye–Waller factor $f_Q = \exp(-2W)$ have been observed long before MCT of the glass transition was developed in Mößbauer-spectra of ^{57}Fe in ferrocene dissolved in butylphthalate [161] and OTP [162]. The results for OTP at $Q = 7.3 \text{ \AA}^{-1}$ are shown in figure 15. One notices a linear temperature dependence at low temperatures. Above T_g a rather strong increase of $2W$ is observed.

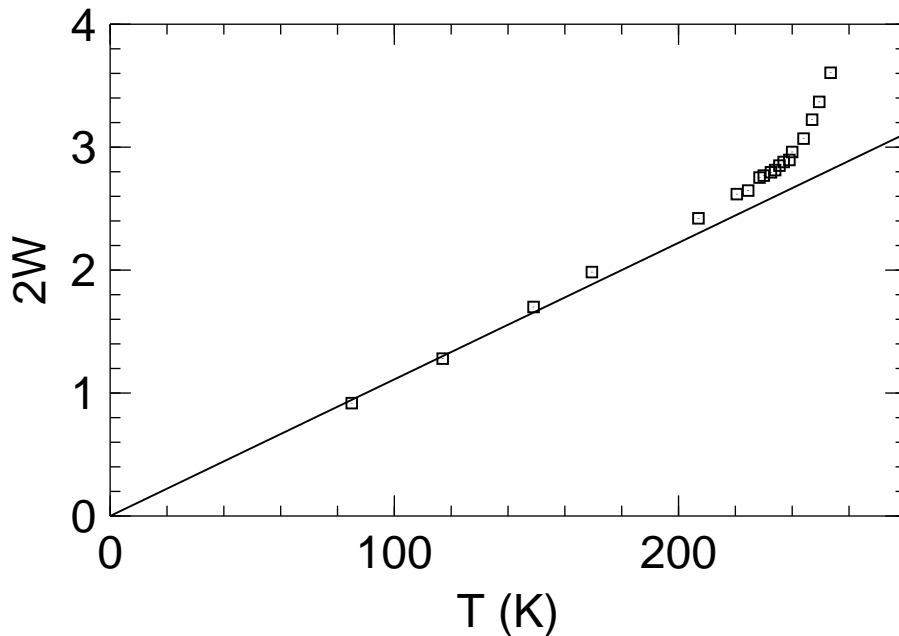


Figure 15. Exponent of the Debye–Waller factor of ^{57}Fe in ferrocene dissolved in OTP as a function of temperature. Based on values given in [162]. The straight line is a linear fit to the lowest two values and zero to give a consistent picture with the results discussed in section 8. Note a nearly linear temperature dependence at low temperatures followed by a strong anomalous increase above T_g .

The predicted square root singularity (16) was extensively tested by neutron scattering experiments [42, 82, 101, 163, 164, 165, 166]. At low temperatures f_Q can be easily measured by the elastic intensity in a BS experiment or by determining the plateau

of the $\Phi(Q, t)$ vs. $\log t$ curve. In figure 16 we give results for temperature dependent incoherent and coherent scattering. For low temperatures we simply follow the harmonic evolution of the mean square displacement ($\ln f_Q(T) \propto T$). The anomalous decrease connected with the glass transition starts somewhere around T_g in the glassy phase due to anharmonic motion on a microscopic length scale. It is clear that the structural relaxation which at T_g is of the order of seconds cannot be responsible for this effect and therefore T_g as conventionally defined has nothing to do with it.

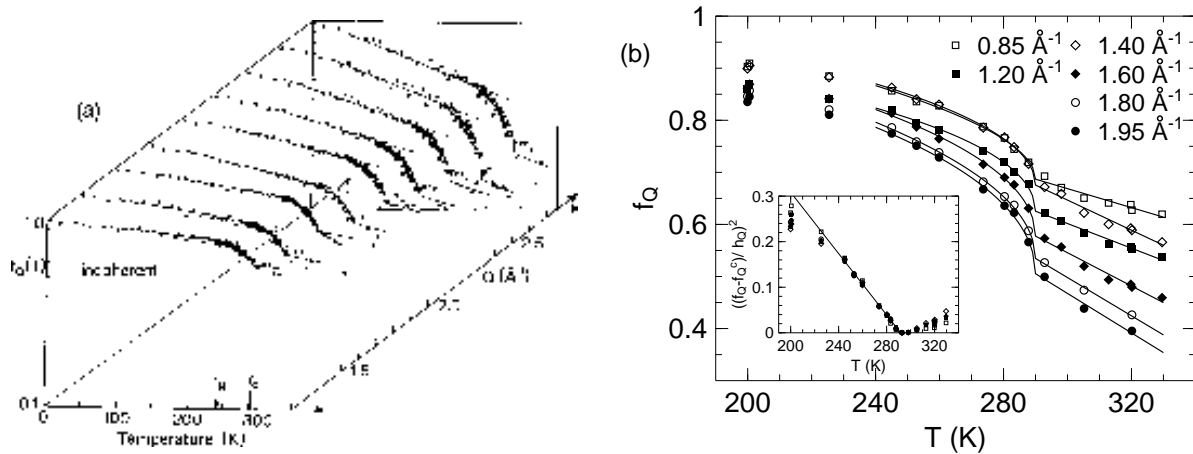


Figure 16. (a (*) Incoherent Mößbauer–Lamb factor of protonated OTP for several Q -values [163]. A harmonic behaviour at low temperature is followed by the onset of an anomalous decrease around T_g . Note the cusps in the temperature dependence at T_c . A square–root law fit gives a common $T_c \simeq 290$ K for all Q . (b (*) Temperature dependence of the Debye–Waller factor of the density correlations for various values of Q . Lines are fits with a square root law leading to a critical temperature of $T_c \simeq 290$ K. Towards higher temperatures a weak linear temperature dependence is assumed. The inset demonstrates the square root law in linearised form.

On approaching T_c the sharp transition predicted by the idealised version of the theory is smeared out through thermally activated hopping processes, which are present in any molecular liquid. Clearly, between the caloric glass transition temperature T_g and T_c structural relaxation is present. When its time scale falls into the experimental window quasielastic broadening appears and its total intensity can no longer be determined from strict elastic scattering alone. Instead, the integral over the whole α peak has to be taken. The results are presented in figure 16 showing all features predicted by (16).

An important question to answer is whether the anomaly of the Debye–Waller factor may be caused by any intramolecular motion such as the librational dynamics of the lateral phenyl rings relative to the central one. This can be checked by measurements of the Debye–Waller factor in isotopically substituted OTP systems, namely fully protonated OTP- d_0 , fully deuterated OTP- d_{14} and selectively deuterated at the lateral phenyl rings OTP- d_{10} . Assume two types of motion, a center–of–mass (COM) motion and an intramolecular (IM) motion of the lateral phenyl rings. Then the central ring

only contributes to the COM motion, while the lateral rings contribute to both the COM and the IM motion. From the total scattering cross sections (cf. table 1) for the nuclei participating in each motion it follows, that in particular in OTP- d_{10} neutron scattering is nearly insensitive to the lateral rings (they are "hidden") as the dominant scattering stems from the central ring protons. Consequently, if the β -process, which is responsible for the anomalous decrease of $f_Q(T)$ is due to intramolecular motion, it should be much less pronounced in OTP- d_{10} . As the Q dependence of the DWF is essentially the same for the three isotopically substituted OTPs [101] and can be approximated by a Gaussian $f_Q = \exp[-\frac{1}{3}Q^2\langle r^2 \rangle]$ we can deduce the mean square displacement shown in figure 17. From the comparison of the observed anomaly in

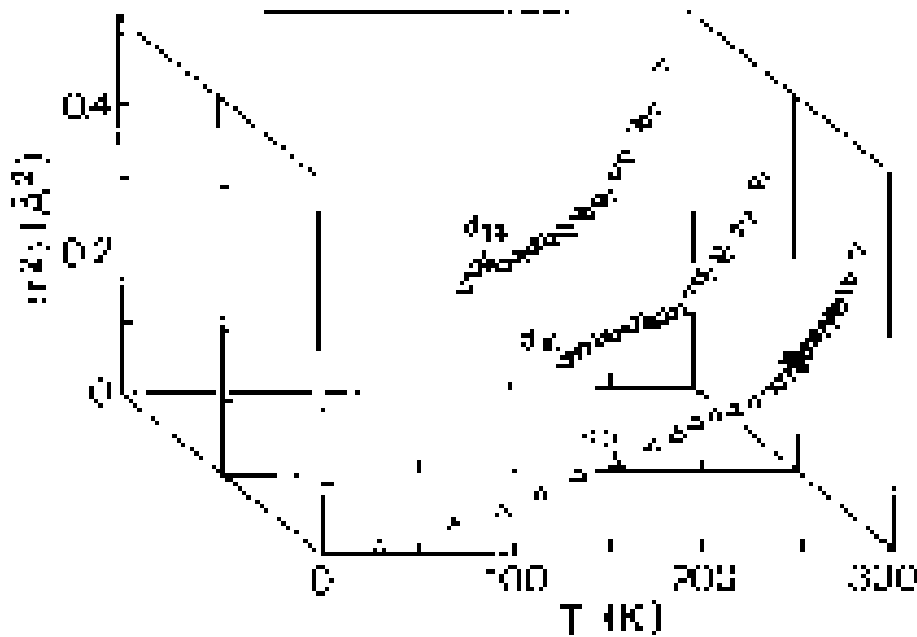


Figure 17. Mean square displacement of three isotopically substituted OTPs obtained from elastic scans on IN13. Within experimental error the three data sets are identical. Taken from [101].

OTP- d_0 and OTP- d_{10} , we can exclude any intramolecular phenyl ring dynamics as the dominant mechanism for the β process. The data thus support MCT proposing a center-of-mass motion as precursor of the glass transition. Note, that although the values for $\langle r^2 \rangle$ of OTP- d_{14} coincide with those of OTP- d_0 and OTP- d_{10} , the comparison is biased as in OTP- d_{14} , which is a dominant coherent scatterer, we do not observe the single particle mean square displacement. In addition, with a higher Q -resolution one can clearly observe oscillations in f_Q (see figure 22) leading to deviations from the simple Gaussian behaviour.

The anomalous behaviour and cusp of the nonergodicity parameter f_Q has also been observed in computer simulations [134, 135]. The cited critical temperature $T_c = 280$ K is in reasonable agreement with the one determined from neutron scattering. X-ray

results allowed for the identification of a temperature $T_x \simeq 290$ K and a cusp from the temperature dependence of a high energy propagating soundlike mode [120].

6.4. Critical Correlations

On BS spectrometers only indirect information can be gained about the existence of a fast process. In order to study the β process directly shorter times have to be accessed which is possible on TOF spectrometers. Whether data are analyzed in frequency or time is a question of convenience.

One remarkable prediction of MCT is the factorization property of the β -relaxation. In a certain frequency and temperature or pressure range, all observables are expected to have the same spectral distribution. This implies that the dynamic structure factor $S(Q, \omega)$ factorises into a Q - and a ω dependent part as a direct consequence of the cage effect. Figure 18 demonstrates the validity of the factorization property for incoherent and coherent scattering: the rescaled intensities $S(Q, \omega)/S(Q)A_Q = G(\omega)$ fall onto a common master curve for different wave numbers Q [42, 107, 167].

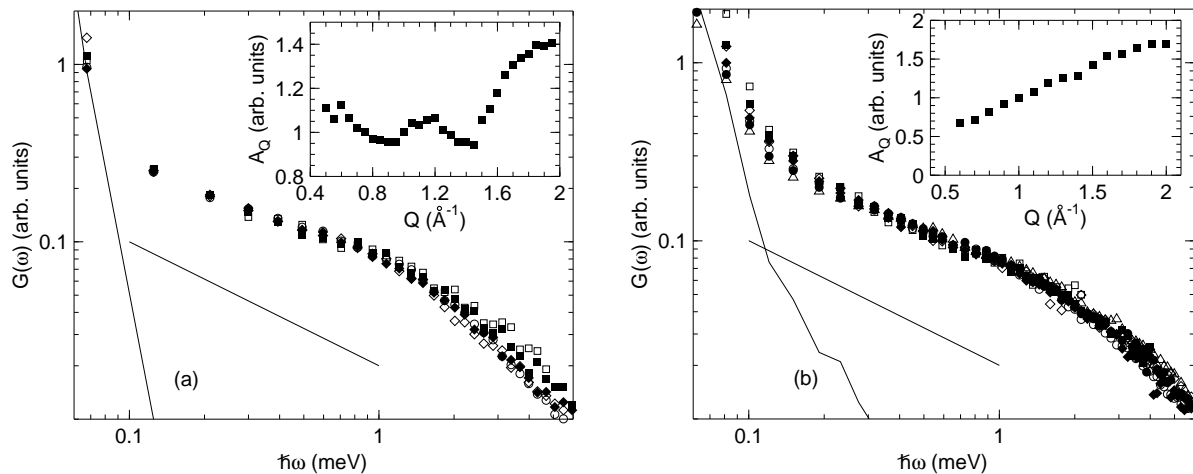


Figure 18. Test of the factorization property for coherent at 293 K (a) and incoherent scattering data at 324 K and 60 MPa (b (*)). The rescaled intensities $S(Q, \omega)/S(Q)A_Q = G(\omega)$ for different wave numbers ranging from 0.4 \AA^{-1} to 2 \AA^{-1} are shown to fall onto a common curve in the energy range between 0.1 meV and 1 meV. For comparison a power law ω^{1-a} , $a = 0.3$ is shown which is the proposed line shape from theory. The steeper lines are the measured resolution functions and set the lower bounds. The insets show the scaling factors A_Q which are proportional to the β -relaxation amplitude h_Q . Note for coherent scattering the two minima corresponding to the prepeak and the first maximum of the static structure factor.

For a detailed study of the β -relaxation we Fourier deconvolute the dynamic structure factors as the quasielastic broadening is of the order of the instrument's resolution. For an analysis in time domain we combine data from different spectrometers with overlapping time ranges to enlarge the dynamic range. Some results for the tagged-particle [107] and the density correlations [42, 164] at different temperatures are shown

in figure 19. In Ref. [167] a second Fourier transform was hereafter performed to analyze the scaling behaviour of the dynamic susceptibility $\chi''(\omega)$ around its minimum.

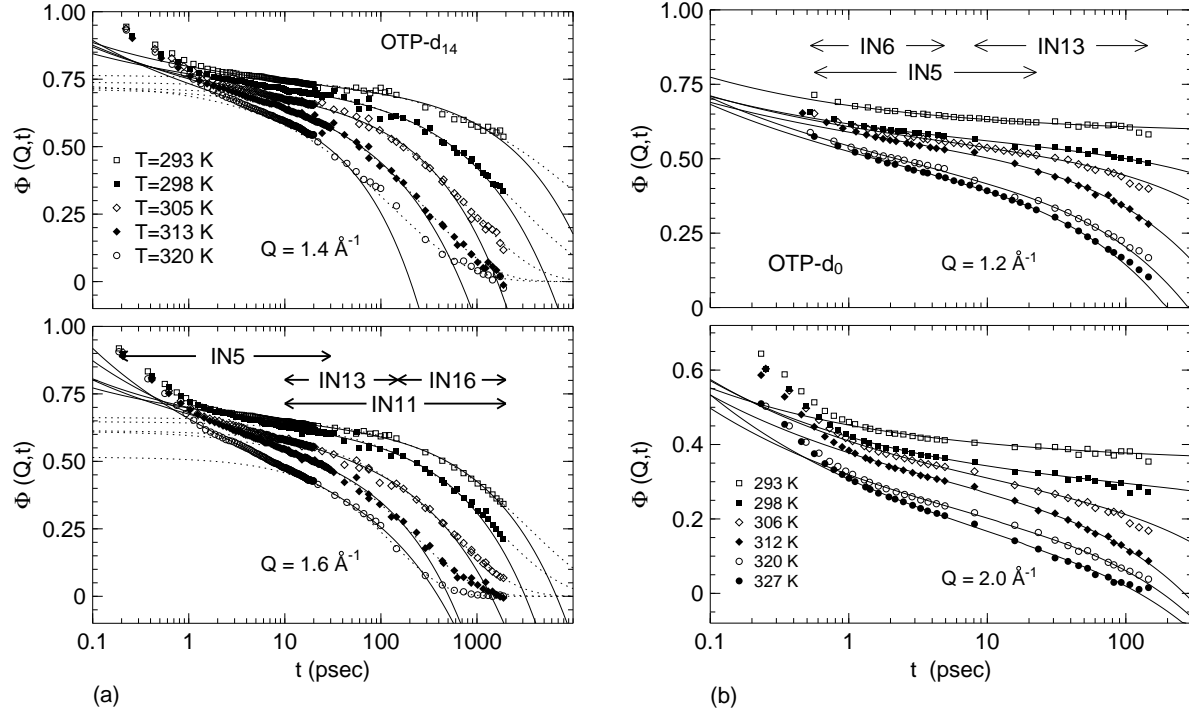


Figure 19. Normalized intermediate scattering functions $\Phi(Q, t)$ for density (a (*)) and tagged particle fluctuations (b) (taken from [22]) for two different wave vectors at various temperatures. The ranges of the instruments used are indicated. Solid lines are fits with the MCT scaling law (17). The line shape parameter $\lambda = 0.77$ was kept fixed for the incoherent data while for the coherent data it was fitted freely. The decay of the correlations is described over several decades. For the coherent data we included KWW fits (1) to the long time tail of the correlation functions (dotted lines).

For fits with (17) we use the tabulated expansion coefficients [143] of the scaling function $g_\lambda(t/t_\sigma)$ which is completely determined by the exponent parameter λ . Meaningful four-parameter fits are often not warranted by the dynamic range covered, here in particular for the incoherent data shown in figure 19 on the right. However, as the line shape is not very sensitive to small variation of λ it was kept fixed at the value 0.77 previously derived from a scaling analysis of the long time asymptote of the correlation function $\Phi(Q, t)$ [163, 168]. This value is compatible with the one from the power-law fit to the viscosity $\eta(T)/T$ in figure 9 [168]. For the coherent data by the combination of time-of-flight (IN5), spin-echo (IN11) and back-scattering (IN13, IN16) data a time range of now more than four decades is covered as can be seen in the left part of figure 19. IN5, IN11 and IN13 have a broad overlap and their $\Phi(Q, t)$ show very good agreement after the absolute scales were adjusted by typically 5%. IN16 data couldn't be obtained in absolute units and were matched to IN11 or IN13 data. Note, a combination of spin-echo data with TOF and BS data has rarely been attempted [13] possibly due to the different weighting of coherent and incoherent scattering in (12).

However, when the coherent scattering largely dominates the signal, for example around the static structure factor maximum such a combination is reasonably possible. Now a four-parameter fit seems more promising and the results for the line shape parameter λ is shown in figure 20. The values for different temperatures T and wave numbers Q indeed scatter statistically around the mean value $\bar{\lambda} = 0.77$ validating our previous analysis [42, 107].

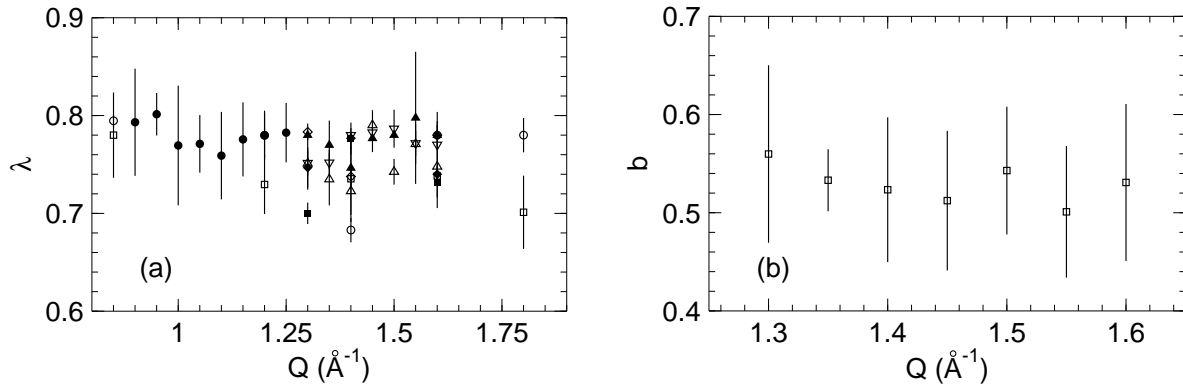


Figure 20. (a (*)) Line shape parameter λ from fits to the density correlation functions (figure 19) which have been obtained by combining up to four different instruments (IN5,IN11,IN13,IN16). The values lie between 0.7 and 0.8 and scatter statistically around a mean value of 0.77 which is consistent with the one determined by other means. Note, no significant temperature (different symbols) or Q -dependence is observed in accordance with the prediction of MCT. (b (*)) Von Schweidler exponent b for density correlations from fits to the master curves. The data scatter statistically around a mean of 0.53 which is consistent with $\lambda = 0.77$.

The β -relaxation scaling is expected to hold only in a wave number and temperature dependent time window $[t_{\min}(Q, T), t_{\max}(Q, T)]$ around the cross-over time t_{σ} . As the scaling law is a long-time expansion where details of the vibrational motion are neglected it should fail to hold for times shorter as or of the order of a typical vibrational period, say a psec. Towards longer times the α -relaxation which itself strongly depends on Q and T starts to merge with the late β regime and renders the identification of a fit range rather ambiguous. As the predictions of MCT are based on expansions around T_c we expect the scaling law to hold best close to the critical temperature. There, on the other hand, additional transport processes not included in MCT's elementary version may obscure it.

From figure 19 we can see that the fits with (17) are able to describe the decay of tagged-particle as well as density correlations over several decades in time. It might come as a surprise that the correlators at the highest temperatures are described down to about $f_Q/2$ as the leading order solutions $\Phi(Q, t)$ (17) have been obtained by an expansion in the distance from the plateau $|\Phi(Q, t) - f_Q|$.

The physical meaning of such fits has to be judged from the comparison of the obtained parameters with the theoretical predictions (18). Such comparisons should

comprise not only temperature T and / or pressure P but also the wave number Q dependence. The temperature dependence of h_Q and t_σ for tagged-particle and density correlations is shown in figure 21 confirming the asymptotic prediction (18). Extrapolation of the T -dependence gives consistently $T_c \simeq 290$ K for *all* data sets coinciding with the critical temperature determined from the square root anomaly of the Debye-Waller factors and the divergence of the viscosity.

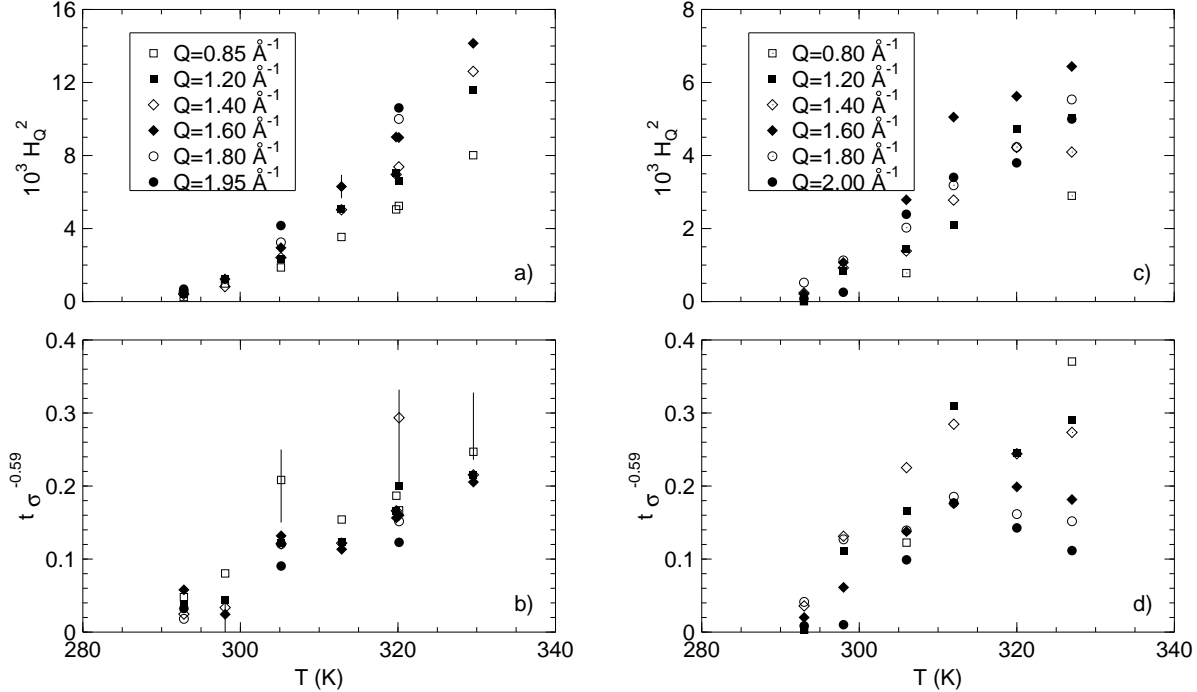


Figure 21. Temperature dependence of the amplitude H_Q and the cross-over time t_σ as obtained from fits to the correlation functions $\Phi(Q, t)$. The parameters are plotted such that a linearized T dependence is expected according to (18). Coherent (a,b) as well as incoherent (c,d) data extrapolate consistently to $T_c \simeq 290$ K. While the absolute values of both, the incoherent and the coherent cross-over times t_σ are quite the same the amplitudes H_Q differ. Taken from [42, 107].

Also the wave number dependence shown in figure 22 at least qualitatively agrees with results from numerical solutions of mode-coupling equations [6, 145]. For incoherent scattering f_Q^s reflects the single particle oscillations and it corresponds closely to a Gaussian distribution [163, 168]. For coherent scattering the plateau height f_Q^c and the amplitude h_Q are obtained from a fit by (16) to the DWF shown in figure 16 and from a fit of (17) to $\Phi(Q, t)$ shown in figure 19. Both results are nearly identical and oscillate in and out of phase with the static structure factor $S(Q)$, respectively. Remember, the scaling factors A_Q in the insets of figure 18 are proportional to h_Q , which independently gives strong support for our findings.

When the abscissa of the theoretical curves [6, 169] is scaled to a hard sphere diameter of $\sigma \simeq 7.5$ Å even a more quantitative agreement is found for both, the coherent and incoherent results.

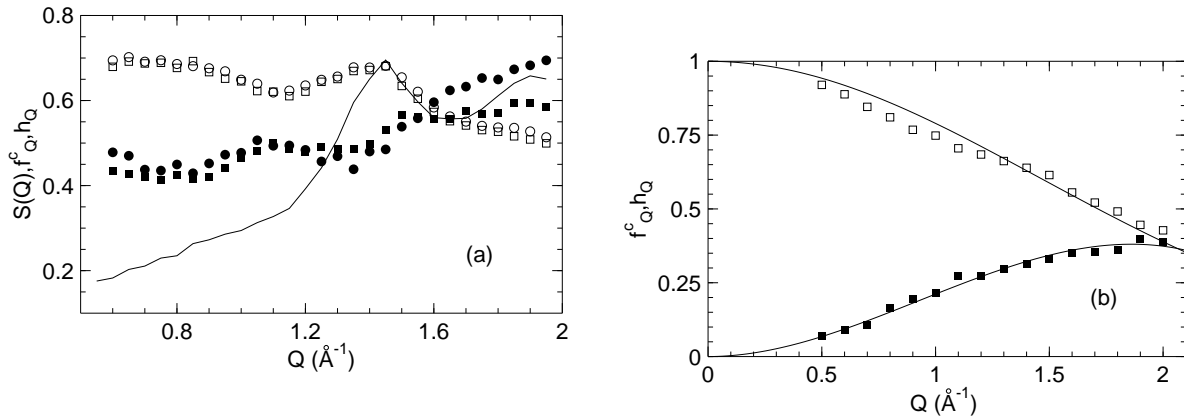


Figure 22. (a (*)) Wave number dependence of the non-ergodicity parameter f_Q^c (open symbols) and the β -relaxation amplitude h_Q (closed symbols) for the density fluctuations compared to the static structure factor (line). The results stem from the fits to the correlation function (squares) and to the DWF (circles). f_Q^c varies in phase, h_Q out of phase with the static structure factor. (b (*)) Same as in (a) for the tagged particle fluctuations. The lines are predictions of theory redrawn from [6] with the abscissa scaled to a hard sphere diameter $\sigma \simeq 7.5 \text{\AA}$ which corresponds to the prepeak of the static structure factor $S(Q)$.

The factorization property has also been verified for the coherent intermediate scattering function in an appropriate time regime [42]. According to (17) the quantity $(\Phi(Q, t) - f_Q^c)/h_Q$ is independent of Q . This has been tested using the fit parameters f_Q^c and h_Q for wave numbers between 0.8\AA^{-1} and 2\AA^{-1} . The cross-over time t_σ and the time range over which the factorization is fulfilled decrease with increasing temperature. This factorization is only possible if the line-shape parameter λ and the cross-over time t_σ of the β -correlator are both independent of Q . A fit of $g_\lambda(t/t_\sigma)$ to the combined data gives $\lambda = 0.78$ in excellent accord with the values determined by other means [42].

Here we want to follow another approach. As already mentioned in section 5 in the context of equation (17), the whole time dependence of any arbitrary time-correlation function $\Phi_Q(t)$ which couples to density fluctuations is given by the Q -independent function $g_-(t/t_\sigma)$ ($\sigma < 0$). Introducing the following function [151]

$$R_Q(t) = \frac{\Phi_Q(t) - \Phi_Q(t')}{\Phi_Q(t'') - \Phi_Q(t')} \quad (26)$$

one can test this prediction even without fitting with (17). Here $t' \neq t''$ are arbitrary times in the β -relaxation regime. From (17) we immediately recognize that the function $R_Q(t)$ is independent of the correlator, *i. e.* of Q . To test this property we take the density correlation function at 293 K of figure 19. For the five different Q ($0.85 \text{\AA}^{-1} \leq 1.8 \text{\AA}^{-1}$) we determined $R_Q(t)$ choosing arbitrarily $t' = 5 \text{ ps}$ and $t'' = 50 \text{ ps}$. Figure 23 shows that in the β -relaxation regime the different $R_Q(t)$ indeed collapse onto a master curve demonstrating the validity of the factorization property. This is not a trivial result as outside the β -relaxation regime the curves fan out. One can even try to go further. Regarding the next order corrections (24) and (25) it can easily be shown that for the function $R_Q(t)$ the order of the corrections in the early β -relaxation regime and in the

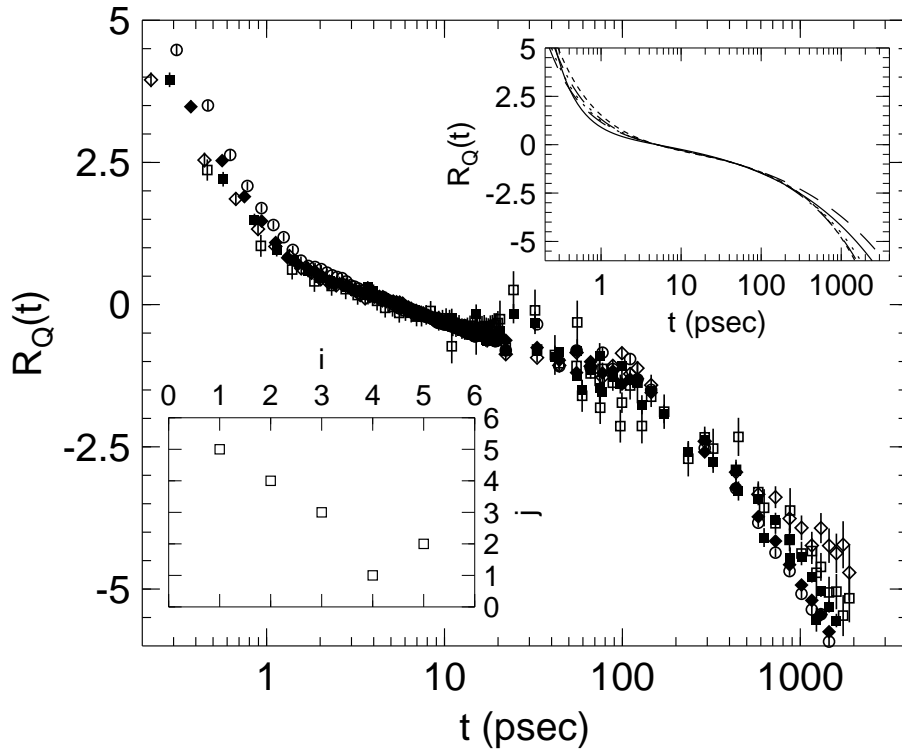


Figure 23. (*) Time dependence of the ratio $R_Q(t)$ given in (26) demonstrating the factorisation property for $T=293\text{K}$. In the upper right inset $R_Q(t)$ for fitted curves is shown. For the lower left inset see text.

late β -relaxation regime are related in the following way: Counting from top to bottom the first (second, ...) curve at short times (label i) is also the first (second, ...) at large times (label j) which means that $i = j$. Both times have to be taken slightly outside the range where (17) holds. Counting at $t \simeq 1\text{ps}$ and at $t \simeq 1000\text{ps}$ gives us the function $j(i)$ displayed in the inset of figure 26. Although only five values are considered here there seems to be no clear correlation $i = j$ but rather an anticorrelation. This is in contrast to results from molecular dynamic simulations [151]. As the experimental data scatter quite large we fitted the correlation functions with a power law similar to the (17) however without any constraints to have a good smooth representation of the data in the time range from about 0.2ps to about 2000ps . We then calculate $R_Q(t)$ for the fitted curves which are displayed in the upper right inset of figure 23. Identical results are obtained concerning the factorization and the function $j(i)$ as from the experimental data. Here again the limitations of neutrons scattering show up: To tackle this problem properly, high energy transfers (very short times) in combination with high energy resolution (long times) (preferably on one spectrometer) would be needed in addition to a good Q resolution and a large wave number range to have a considerable amount of different correlation functions.

The fast dynamics has also been experimentally observed by depolarized light

scattering [53, 125, 127]. Comparisons with idealized MCT yields a critical temperature $T_c \simeq 288 - 292$ K with line shape parameters of $a = 0.33, b = 0.65, \lambda = 0.7$ [124, 125] and equally $T_c \simeq 288 - 292$ K with $a = 0.32, b = 0.61, \lambda = 0.72$ [127]. The numbers for T_c and λ are consistent within the experimental uncertainties with the values used to describe the neutron scattering results. Depolarized light scattering has a rather large dynamic range covering about 4 decades and high statistics such that a comparison with the extended MCT became possible [127]. The analysis yields $T_c \simeq 276$ K with $a = 0.3, b = 0.54, \lambda = 0.76$.

The dynamics below the critical temperature T_c was investigated less extensively. Below T_c the idealized MCT predicts a nontrivial behaviour of the generalized susceptibility $\chi''(\omega)$: a white-noise spectrum at very low frequencies $\chi''(\omega) \propto \omega$ should cross-over to a power law $\chi''(\omega) \propto \omega^a, a < 0.4$ resulting in a "knee" in $\chi''(\omega)$ at intermediate frequencies. Rather counterintuitive is the nontrivial prediction for the temperature dependence of the position of the "knee"-frequency: ω_β^{-1} should *increase* with increasing temperature and diverge at T_c . In our neutron scattering experiments in the temperature range $200 < T < T_c$ no indication for such a cross-over is observed in the frequency range $\omega \gtrsim 0.1$ meV (25 GHz). The same observation was made in careful light scattering experiments [170]. However, this does not necessarily mean that the "knee" does not exist as the influence of the hopping processes *i. e.* its strength is unknown at present. If the hopping is sufficiently small the ideal spectrum is rather undisturbed and the "knee" should appear, however, if the hopping term is large the initial α decay can make it disappear.

So far, the only support of the existence of such a diverging time scale below T_c comes from PCS experiments on a hard sphere colloidal liquid [7, 8, 9] and on a polymer microneetwork colloidal liquid [171] where no microscopic dynamics and no hopping processes disturb the β -process.

6.5. α -Relaxation

The α -relaxation can be directly studied e. g. either by energy resolved BS or NSE experiments. For instance in figure 24 we show the coherent scattering function $\Phi(Q, t)$ of OTP- d_{14} as measured on the SE instrument IN11C using the multidetector set-up. For comparison, $S(Q, \omega)$ as measured on IN10B with a heated monochromator is shown on the right hand side of figure 24 for several wave numbers Q . In both cases the line-shape cannot be described by a single Debye function but can be well fitted by a Kohlrausch function.

The validity of viscosity scaling and time-temperature superposition is still an ongoing debate. We have seen that it is a very good first approximation at least in a narrow temperature range. Statistics and the limited dynamic range of one instrument hardly allows for a serious test. However, consistent results with acceptable error bars can be obtained by combination of measurements from different temperatures (or pressures). Assuming that viscosity scaling holds over the covered T -range we employ

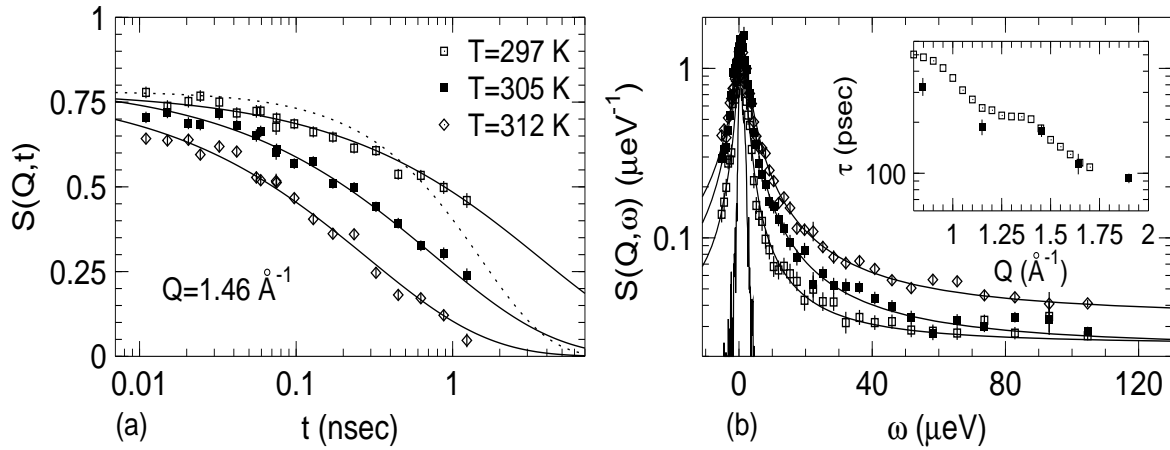


Figure 24. (a (*)) High resolution spectra of OTP- d_{14} at $Q = 1.46 \text{ \AA}^{-1}$ for several temperatures as measured on the SE instrument IN11C using the multidetector. The fit curves demonstrate that the line shape of the structural relaxation is well described by a KWW function according to (1) with $\beta \simeq 0.57$ and not by a simple Debye process drawn for comparison (dashed line). (b (*)) Dynamic structure factor $S(Q, \omega)$ at 320 K for $Q = 0.85 \text{ \AA}^{-1}$ (\square), $Q = 1.45 \text{ \AA}^{-1}$ (\blacksquare) and $Q = 1.90 \text{ \AA}^{-1}$ (\diamond) as measured on the BS instrument IN10B with a heated monochromator. Lines are fits with a Fourier transformed Kohlrausch function with $\beta_Q = 0.57$ fix for all Q .

the following iterative procedure to construct master curves $\hat{\Phi}(Q, \hat{t})$: We use published viscosities [24, 25, 26, 27, 28] to rescale experimental times to

$$\hat{t} = t[\eta(T_0)/T_0]/[\eta(T)/T] \quad (27)$$

with an arbitrary normalization $T_0 = 290 \text{ K}$. From Kohlrausch fits to $\hat{\Phi}(Q, \hat{t})$ we obtain first approximations for the line shape parameter β_Q and the relaxation time $\tau_Q(T_0)$. By means of this $\tau_Q(T_0)$ the unscaled $\tau_Q(T)$ of the individual temperatures are calculated and are then kept fixed together with the line shape parameter β_Q in fits to the individual $\Phi(Q, t)$. The resulting set of amplitudes A_Q is used to obtain reduced correlators $\hat{\Phi}(Q, \hat{t})/A_Q$ and the procedure is repeated. It is numerically stable and converges after a few iterations [163]. To get the temperature dependence of each parameter the individual $\Phi(Q, t)$ at each temperature can then be fitted with one free parameter while the other two are kept fixed at the values determined from the iterative procedure.

The results in figure 25 confirm the validity of viscosity scaling for temperature dependent tagged-particle and density correlations. Note, that the scaling is a necessary but not sufficient condition for the applicability of MCT.

The temperature dependence of the relaxation time τ_Q of the density correlations at the structure factor maximum is shown in figure 26. Combination of data from several spectrometers using the iterative procedure described above makes it possible to cover nearly five decades in relaxation time. The structural relaxation time follows nicely the viscosity confirming the validity of viscosity scaling.

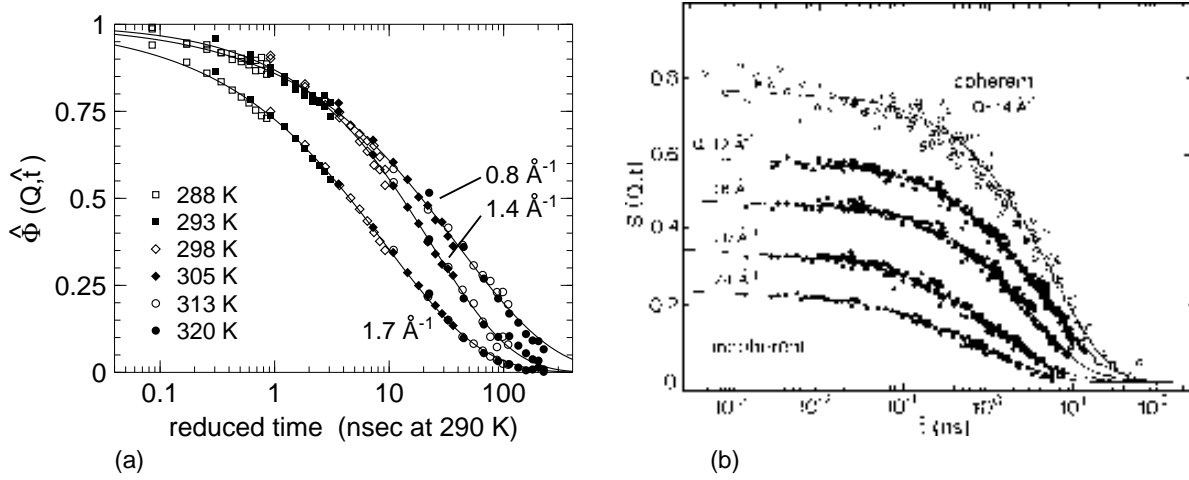


Figure 25. (a) Master curves $\hat{\Phi}(Q, \hat{t})/A_Q(T)$ for the α -relaxation of the density fluctuations at different temperatures, obtained by rescaling times with viscosity $\eta(T)/T$. From [172]. (b) Typical master curves obtained using the scaling assumption for the tagged particle fluctuations. From [163].

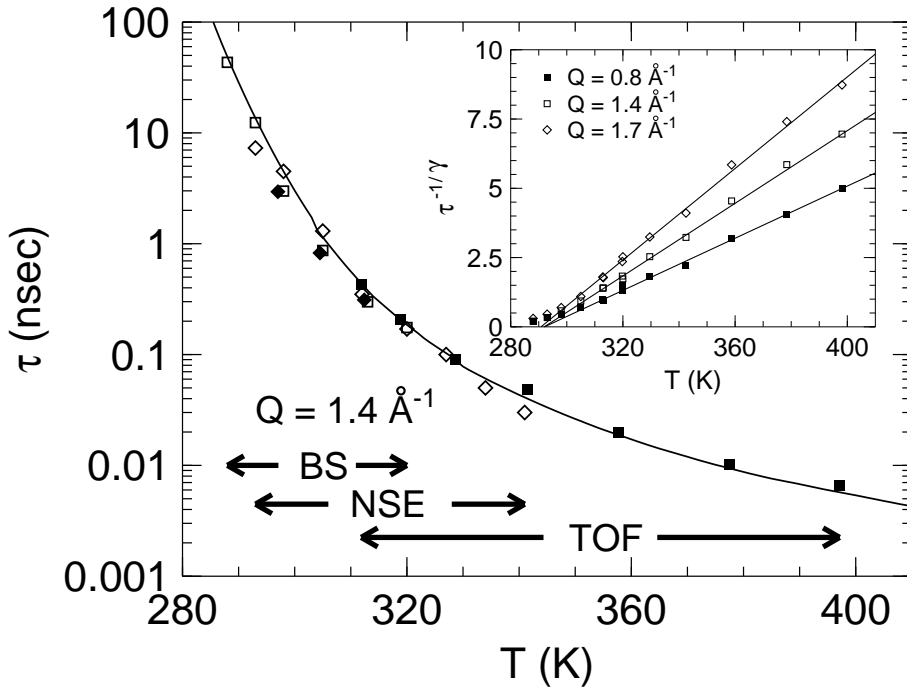


Figure 26. (*) Temperature dependence at ambient pressure of the α -relaxation time τ_Q at the structure factor maximum $Q = 1.4 \text{ \AA}^{-1}$ obtained from the scaling analysis of BS (\square), NSE (\diamond : single detector, \blacklozenge : multidetector) and TOF (\blacksquare) data. The solid line is the scaled viscosity interpolated from literature data [24, 25, 26, 27]. The inset shows $\tau_Q^{-1/\gamma}$ vs. T from BS and TOF data at three different Q -values using $\gamma = 2.59$. A linear behavior extrapolating to zero at $T_c \simeq 292 \text{ K}$ is observed for all Q in accordance with the prediction of MCT.

In the inset of figure 26 we test the divergence of the α scale predicted by MCT (22). Assuming $|\sigma| \propto (T - T_c)$ a plot of $\tau_Q^{-1/\gamma}$ vs. T should produce a straight line extrapolating to zero at T_c . Indeed, a linear behaviour is observed for all wave numbers studied extrapolating to zero at $T_c \simeq 292$ K. This also supports the α -scale universality. The deviations from this law in a narrow temperature range close to T_c may be due to thermally activated hopping processes not contained in MCT's ideal formulation and smearing out the sharp transition. As a consequence, testing the power law only in a narrow range around the critical point could give a wrong idea of, e. g., γ .

The cross-over from the β - to the α -process is described by the von Schweidler law (21). Thus, it should be detectable in the short time behaviour of the α -process. By plotting the master curves in the form $\log[1 - \Phi(Q, \hat{t})/f_Q]$ vs. $\log \hat{t}$ this should yield straight lines with slope b for short rescaled times. The result for coherent and incoherent data is shown in figure 27. Both data sets show a von Schweidler behaviour at short

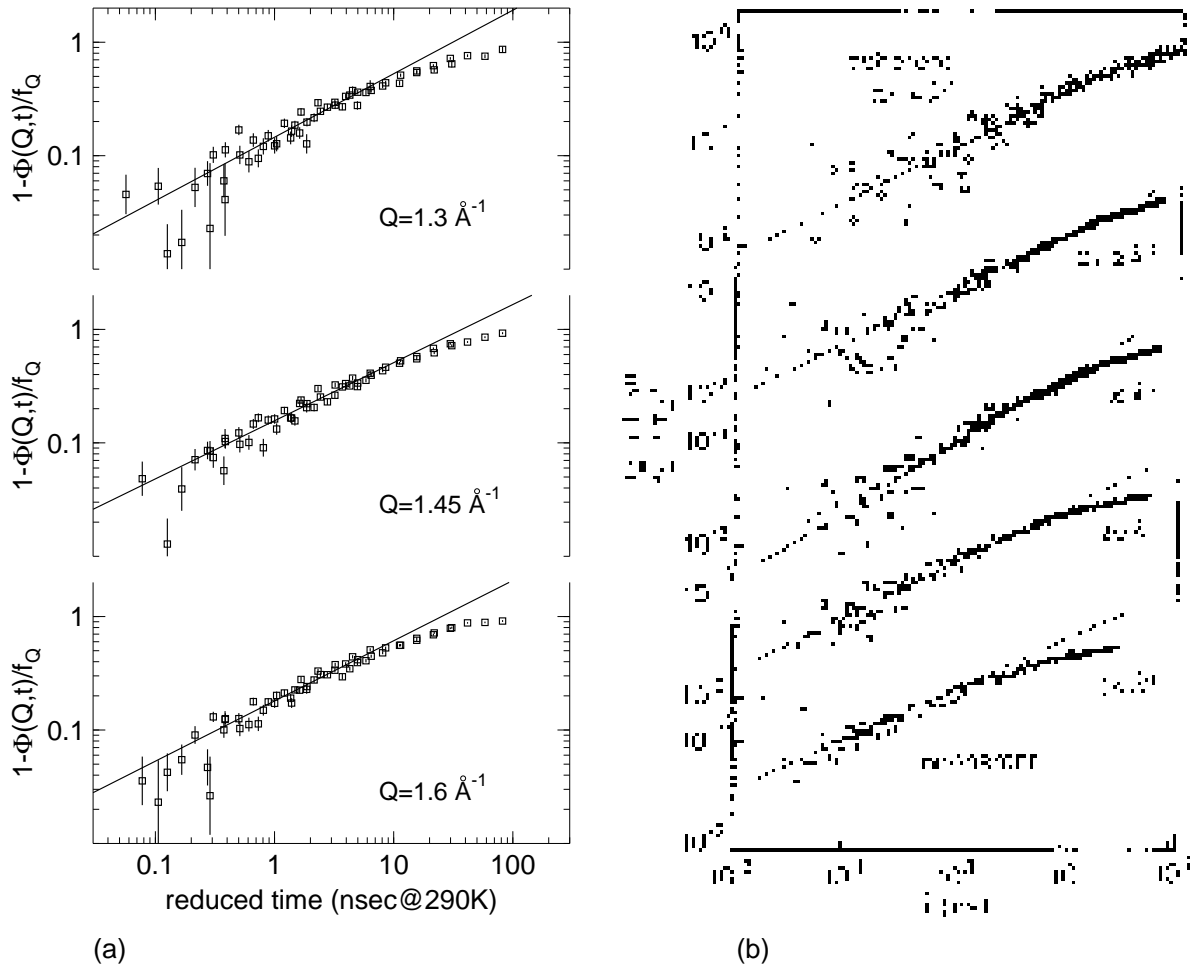


Figure 27. Fits of the von Schweidler law (21) to some linearized master curves for coherent scattering (a (*)) and incoherent scattering (b) (from [163]) in order to show the fractal time dependence t^b . The slopes b scatter around a mean value of 0.53 for both coherent and incoherent data. This value is in excellent accord with the value imposed by the line shape parameter $\lambda=0.77$.

times while at long times deviations occur. In accordance with the theory the values of the von Schweidler exponent b do not show any systematic Q dependence (see figure 20). They scatter around a mean value of $\bar{b} = 0.53 \pm 0.03$.

In order to investigate the Q dependence of the parameters describing the density correlations of the α -relaxation a high Q resolution is necessary. For the question studied here spin-echo seems less appropriate than high resolution multidetector instruments as the Q resolution is implicitly limited by the transmission band of typically $\Delta\lambda/\lambda \simeq 10\%$. Note, increasing the Q resolution by use of a narrower bandwidth or a graphite monochromator leads to an unacceptable reduction in intensity in particular if the experimental beam time comprises several Q and T scans.

The big advantage of spin-echo, the large dynamic range of about three decades, can be compensated either by combining data from time-of-flight and backscattering spectrometers or by the use of master curves. On the BS instruments IN16 (figure 25) and IN10B (figure 24) the Q resolution was improved by covering part of the analyzer crystals by large cadmium shields [172]. This reduces considerably the number of detectors which can be used in the analysis. Multidetector TOF instruments intrinsically have a good Q resolution. However, now a compromise between wave number coverage and energy resolution has to be chosen. On IN5 the elastic energy resolution (fwhm) was set to $25\mu\text{eV}$ restricting the accessible wave number range to $Q \leq 1.7\text{\AA}^{-1}$. As $25\mu\text{eV}$ is a rather broad resolution for a study of the α -relaxation higher temperatures are required to make the dynamics appear in the experimental energy window.

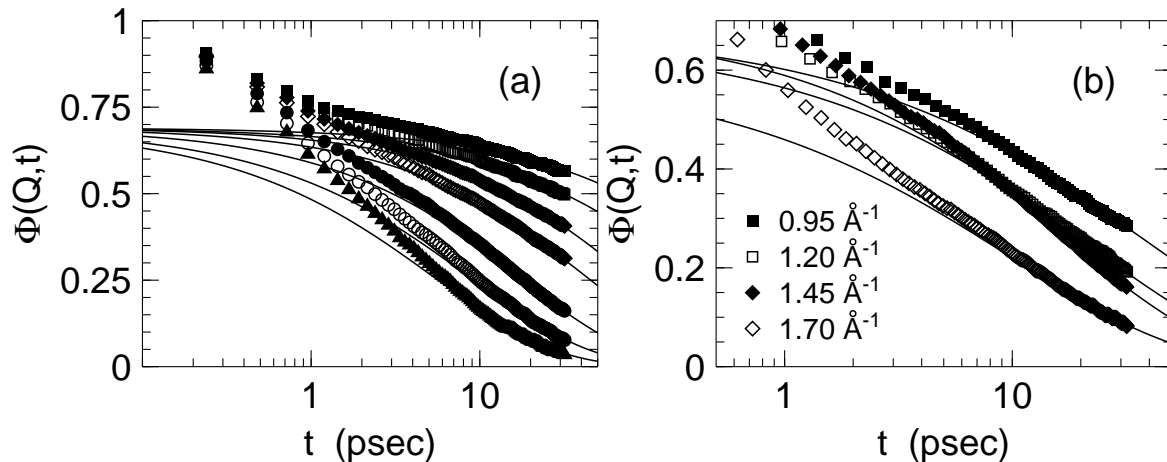


Figure 28. Density correlation function, obtained by Fourier deconvolution of coherent neutron scattering spectra measured on the time-of-flight spectrometer IN5. (a) for different temperatures at the structure factor maximum $Q_1 = 1.45\text{\AA}^{-1}$. Temperatures are from top to bottom: 313 K, 320 K, 330 K, 340 K, 360 K, 380 K, 400 K. (b) on an enlarged scale for 360 K at different wave numbers Q . Solid lines are Kohlrausch stretched exponentials as determined from a master curve analysis. Without any fitting one recognizes that correlations decay steeper at Q_1 than at other wave numbers. Taken from [172].

Some of the data are shown in figure 28a. Up to high temperatures, far above the *melting* point, correlations decay in two steps. The second step is strongly stretched and temperature dependent as expected for the α -relaxation. In figure 28b the long time tail belonging to the α -relaxation is plotted on an enlarged scale for different wave numbers Q . Not only the relaxation time, but also the line shape exhibits a pronounced Q dependence. At $Q_1 = 1.45 \text{ \AA}^{-1}$, the position of the first maximum of the static structure factor, the correlations decay steeper, *i. e.* with *less* stretching, than at any other wave number. Such a behaviour can also be seen in the master curves displayed in figure 25. As one can easily imagine from the data in figure 28a the individual correlation functions $\Phi(Q, t; T)$ do not allow for a three parameter fit of (1): Either, for low temperatures the α -relaxation is outside the accessible time window of the spectrometer, or at high temperatures, where the decay is fully in the window it is heavily disturbed by the β -relaxation. Then a separation of both contributions is not obvious and the fit range is somewhat arbitrary. Note, that even at the highest temperature the decay of the correlation function cannot be fully described by a single Kohlrausch law. Moreover, a free fit with (1) yields unphysical results like a strongly decreasing stretching to values as low as 0.3 and an increase of the amplitude with increasing temperature.

For a more quantitative analysis we employ the time-temperature superposition to obtain master curves. Indeed, without further adjustment, the data converge towards a temperature independent long-time asymptote [172]. The results from this scaling analysis are shown in figure 29. The amplitude factor A_Q and the line shape parameter β_Q are quite independent of temperature in the range from 313 K to 400 K in accord with results from light scattering [127]. In contrast to an often held belief, the stretching exponent does not increase with temperature towards a diffusion limit $\beta = 1$ in the normal liquid phase. Even 70 K above the melting point the correlation functions $\Phi(Q, t)$ remain stretched. The structural relaxation time follows the viscosity and has a generic Q -dependence which confirms the α scale universality.

All parameters describing the density correlations exhibit pronounced characteristic oscillations in phase with the static structure factor $S(Q)$ (figure 29). The amplitude A_Q is in almost quantitative agreement with the Debye-Waller factor f_Q previously obtained from the β -relaxation plateau (figure 22). Note, f_Q and A_Q not necessarily have to be identical. The relaxation time τ_Q shows two plateaus around 0.8 \AA^{-1} and 1.4 \AA^{-1} on top of an overall decrease. More important, the stretching exponent β_Q shows a systematic variation in phase with $S(Q)$ being largest at the structure factor maximum. Even around 0.8 \AA^{-1} a slight variation is suggested from our data. At 1.4 \AA^{-1} the results are obvious from the raw data by plotting the Q dependent decay curves in one diagram (see figures. 25 and 28). They are fully confirmed by fits of (1) to numerical solutions of MC equations for the hard spheres system [145] and a soft spheres mixture [173].

Some reservation is necessary for the smallest wave numbers $Q \lesssim 0.5 \text{ \AA}^{-1}$ where A_Q starts to tend to 1. Even for 99% deuteration the incoherent scattering amounts to about 15% to the total scattering cross section. In addition, in the small Q region the

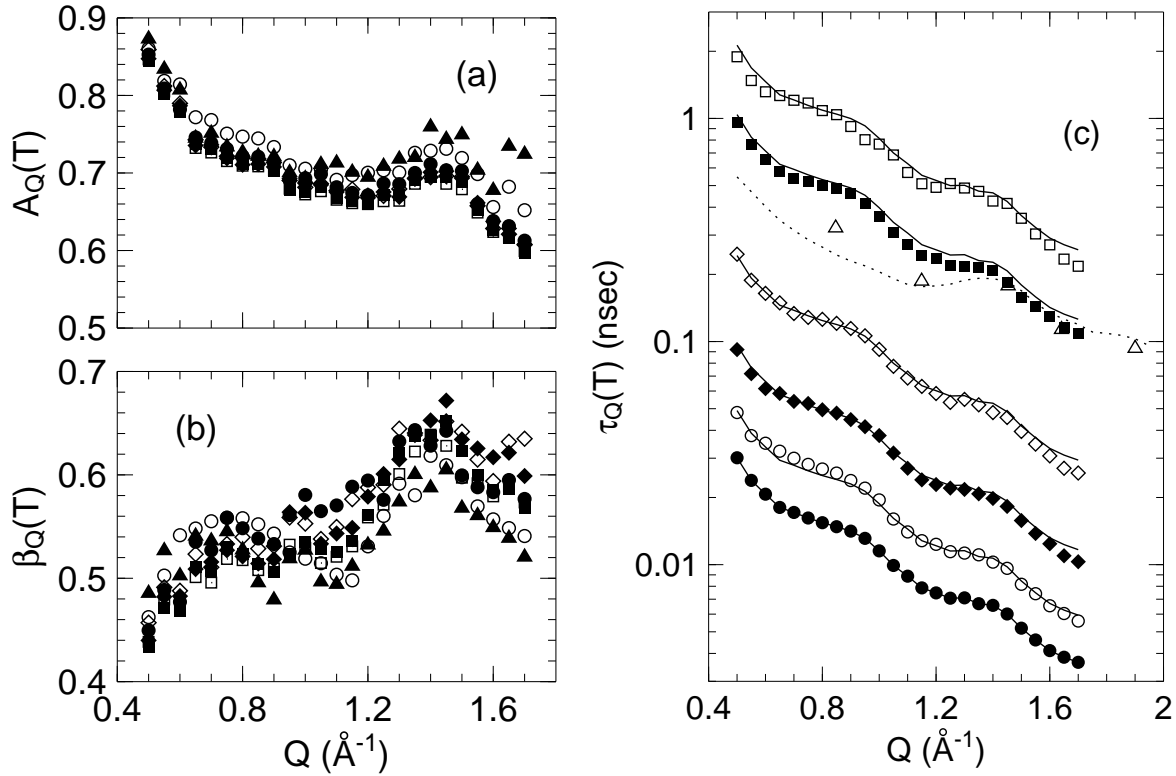


Figure 29. Kohlrausch parameter at seven different temperatures ranging from 313 K to 400 K. In each of these fits, one parameter was free while the two others were kept fixed at the values obtained from the master curve analysis. (a) The amplitude A_Q and (b) the stretching exponent β_Q are temperature independent confirming our scaling approach. (c) The α -relaxation time τ_Q follows for all Q the viscosity and exhibits a generic Q dependence. The data at 330 K have been omitted for clarity as at 320 K the results from the BS instrument IN10B are included (Δ). The dotted line represents the quantity $S(Q, 320 \text{ K})/Q^2$ known as de Gennes narrowing. Based on [172].

coherent scattering itself should be weak as it is roughly proportional to $S(Q)$ which tends towards a constant level. Therefore, the relative incoherent contribution might be even much stronger than 15%. This effect can be studied in more detail by a separation of coherent and incoherent scattering by polarization analysis, cf. figure 12. From this experiment we learn that the coherent f_Q or the α -relaxation amplitude A_Q must be smaller than the incoherent one at $Q \lesssim 0.7 \text{ \AA}^{-1}$ and remains larger for higher Q values. This behaviour is indeed observed in figure 22 and we can conclude that at the lowest Q values contributions from multiple scattering cannot be excluded. They are now even more complicated to treat as coherent and incoherent scattering are a weighted mix. A separation of coherent and incoherent scattering from very thin samples *i. e.* with high transmission seems the most straightforward access to solve this problem. However, as outlined above quantitative results are still out of reach within an acceptable measuring time with the presently available neutron flux and spectrometers.

In a recent work on Toluene, the structural relaxation time τ_Q followed nearly perfectly $S_{\text{COM}}(Q)/Q^2$, where $S_{\text{COM}}(Q)$ is the center-of-mass static structure factor calculated by Monte-Carlo simulation [174]. Such a dependence, in a more general context known as de Gennes narrowing [113], indicates the dominance of the center-of-mass motion, which is of purely translational nature. We therefore included in figure 29 $S(Q)/Q^2$. Around $Q = 1.4 \text{ \AA}^{-1}$ the variation of τ_Q with Q is indeed correctly described by $S(Q)/Q^2$. The simulated center-of-mass static structure factors for OTP is peaked around 0.8 \AA^{-1} [136]. Therefore, the plateau in τ_Q around 0.8 \AA^{-1} strongly supports our simplified picture that was drawn from $S(Q)$ in section 6.2.

The wave number dependence of the tagged-particle correlations measured by incoherent scattering has already been discussed extensively [163, 168]: all parameters depend monotonously on Q : $\beta_{inc}(Q) \approx \text{const.}$, $A_Q \propto f_Q$ decreases like $\exp(-cQ^2)$ and $\tau_{inc}(Q)$ decreases close to a Q^{-2} law which is perfectly confirmed by a recent molecular dynamic simulation [35].

7. Experiments under Pressure

7.1. Experimental Considerations

For practical reasons most investigations on the glass transition concentrate on temperature effects at ambient pressure $P_0 = 0.1$ MPa although there is a clear interest in studying supercooled liquid dynamics in the full T, P parameter space. We emphasize the difference between the effect of pressure and temperature. The primary effect of pressure is to change interatomic distances; changes, for example in atomic vibrations are a secondary effect via anharmonicity of the potential. In contrast, the primary effect of temperature is to alter the atomic vibrations; changes in interatomic distances are now a secondary effect. Pressure and temperature are thermodynamically independent variables even though their effects on one set of observables might be the same. Pressure experiments have demonstrated that the density is not the only driving force for the glass transition [175, 176, 177, 178]. In the microscopic approach of MCT, both pressure and temperature control the dynamics via variations of the static structure factor $S(Q)$ which has been measured on fully deuterated OTP- d_{14} . All other experiments have been performed with fully protonated OTP, thereby measuring the tagged-particle dynamics.

While low temperature is regularly used in neutron scattering, the use of high pressure is less standard as experiments under pressure are much more difficult to perform. There are special requirements for high-pressure cells used in neutron scattering. For example, the flux rates of current neutron sources require large sample volumes in order to get acceptable signal-to-noise ratios in reasonable time. On the other hand the cell body in the neutron beam gives rise to unwanted scattering and absorption which demands a minimum of material in the beam.

High pressure experiments are possible only in a limited temperature-pressure range characteristic for a certain material [179]. The high pressure limit of a cylindrical cell is set by the material strength and the ratio of outer-to-inner diameter r_o/r_i . In order to use the full size of a neutron beam the inner diameter has to be of the order of some centimetres. This easily results in large wall thicknesses leading not only to a strong background but also to an attenuation of the incoming beam and to rather difficult corrections. The background signal, however, not only depends on the wall thickness, *i. e.* from the number of scatterers in the beam but also from the scattering cross-sections of the material. Corrections are difficult to perform if the attenuation of the beam is caused by the energy dependent absorption. Consequently, small ratios are used to keep these effects as small as possible.

High pressure cells based on high strength Aluminum alloys have many of the required/desired properties. Vessels with small wall thicknesses withstanding high pressures produce a rather low background and nearly no absorption due to the low scattering and absorption cross-section. Bragg scattering of Al occurs only for wave numbers $Q \geq 2.7 \text{ \AA}^{-1}$.

The experiments reported here were performed in a standard high pressure cell made of the Aluminium based alloy Al7049.T6 of the ILL. The ratio of outer-to-inner

diameter of 2 allows to attain pressures up to 250 MPa at temperatures up to about 340 K. The composition and scattering cross-sections of the high pressure material are listed in table 3.

Table 3. Composition, scattering and absorption cross-sections of the high pressure material Al7049.T6 of the vessel.

Element	wt%	σ_c /[barn]	σ_i /[barn]	σ_t /[barn]	σ_a /[barn]
^{26}Fe	0.3	11.22	0.40	11.62	2.56
^{14}Si	0.4	2.16	0.004	3.49	0.171
^{24}Cr	0.15	1.66	1.83	4.35	3.05
^{30}Zn	7.6	4.05	0.077	4.131	1.11
^{12}Mg	2.5	3.63	0.08	3.71	0.063
^{29}Cu	1.5	7.49	0.55	8.03	3.78
^{13}Al	87.55	1.49	0.008	1.503	0.231
Al7049.T6	100	1.865	0.026	1.892	0.358

The transmission of the pressure cell was about 85 % and it was handled like a usual container. Restricting ourself to large scattering angles implying large wave numbers Q multiple scattering effects were neglected. The approximate correctness of this approach is demonstrated in figure 30 where the correlation functions measured with and without pressure cell are compared. Apart from a tiny difference in the plateau height the curves are identical.

Due to crystallization tendencies of OTP we had to use ^4He gas as pressure transmitting medium. Any other attempt to use a liquid or OTP itself failed. With a scattering cross-section $\sigma_{\text{coh}}=1.34$ barn ^4He gas is nearly transparent to neutrons. In addition the analysis is not complicated by the fact that a liquid pressure transmitting medium will show the same effects of dense liquid dynamics one is looking for in the sample. Clearly, ^4He diffuses into OTP with a time constant of several hours. However, although the solubility increases with temperature and increasing pressure according to Henrys law, with a typical solubility of about 10^{-5} mol/(gMPa) in aromates there is less than one He atom in the first coordination shell.

7.2. Static Structure Factor

The static structure factor of OTP- d_{14} was measured on the instrument D7, now used as a diffractometer without energy analysis. The pressure and temperature dependence of $S(Q)$ is shown in figure 31. $S(Q)$ was obtained in absolute units by comparison with a vanadium standard.

Under temperature variation at constant pressure (isobaric) the peaks behave as at ambient pressure. With decreasing temperature the scattering intensity in the $Q \rightarrow 0$ region reduces due to the decreasing isothermal compressibility χ_T . $S(Q=0) = n\chi_T k_B T$ compares well with the values calculated from temperature and pressure dependent specific volumes [46]. The peak positions shift slightly to higher Q values due to an

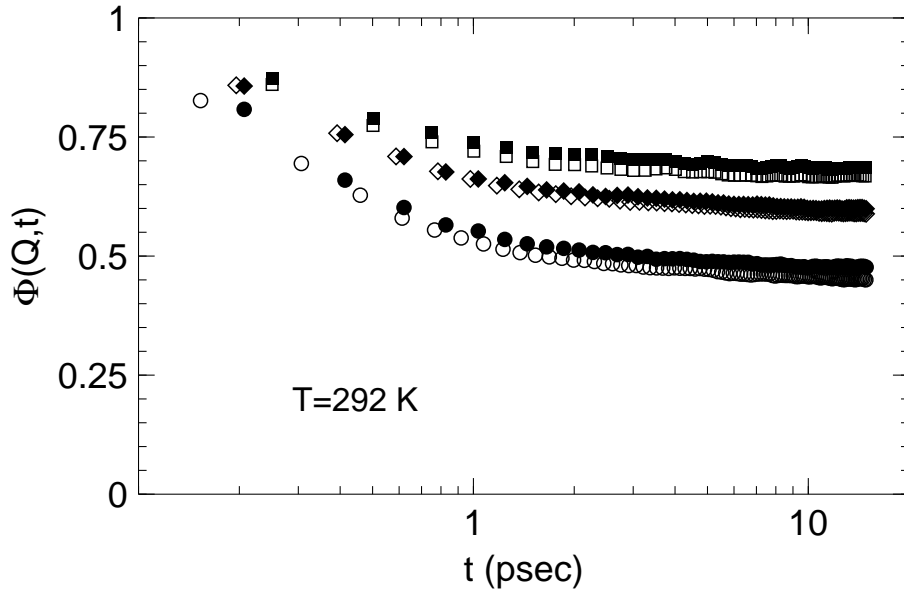


Figure 30. (*) Comparison of the correlation functions obtained without (open symbols) and in the high pressure cell (closed symbols) at $Q = 1.2$ (\square, \blacksquare), $Q = 1.5$ (\diamond, \blacklozenge) and $Q = 1.8 \text{ \AA}^{-1}$ (\circ, \bullet). The curves are nearly identical which validates the simplified approach of treating the high pressure cell like an ordinary container.

increase in density n . Concerning the peak heights the maximum at 1.4 \AA^{-1} is not much affected, the maximum at 1.9 \AA^{-1} is enhanced and the prepeak is lowered when cooling.

The effect of increasing pressure at constant temperature (isothermal) on $S(Q)$ is similar to the one of decreasing temperature: $S(Q \rightarrow 0)$ decreases and the peak positions move to higher Q . The intensity of the prepeak and the first maximum decreases while that of the second maximum increases. This behaviour is in agreement with results on other materials [180, 181].

Two other types of measurements are interesting in the light of MCT since the static structure factor is considered to be the trigger of the slowing down of the α -relaxation: isochoric measurements of $S(Q)$, *i. e.* at (T, P) combinations leading to the same bulk density and isochronous measurements, *i. e.* at (T, P) combinations where the α -relaxation time is identical. Such measurements are included in figure 31. While along isobars and isotherms the static structure factors $S(Q)$ evolve continuously, it is nearly identical along an isochor and an isochron.

7.3. Square Root Singularity

When the pressure dependence of the elastic scattering at constant temperature is monitored a behaviour slightly different as compared to the temperature dependent experiments is observed. In figure 32 left the isothermal DWF for incoherent scattering

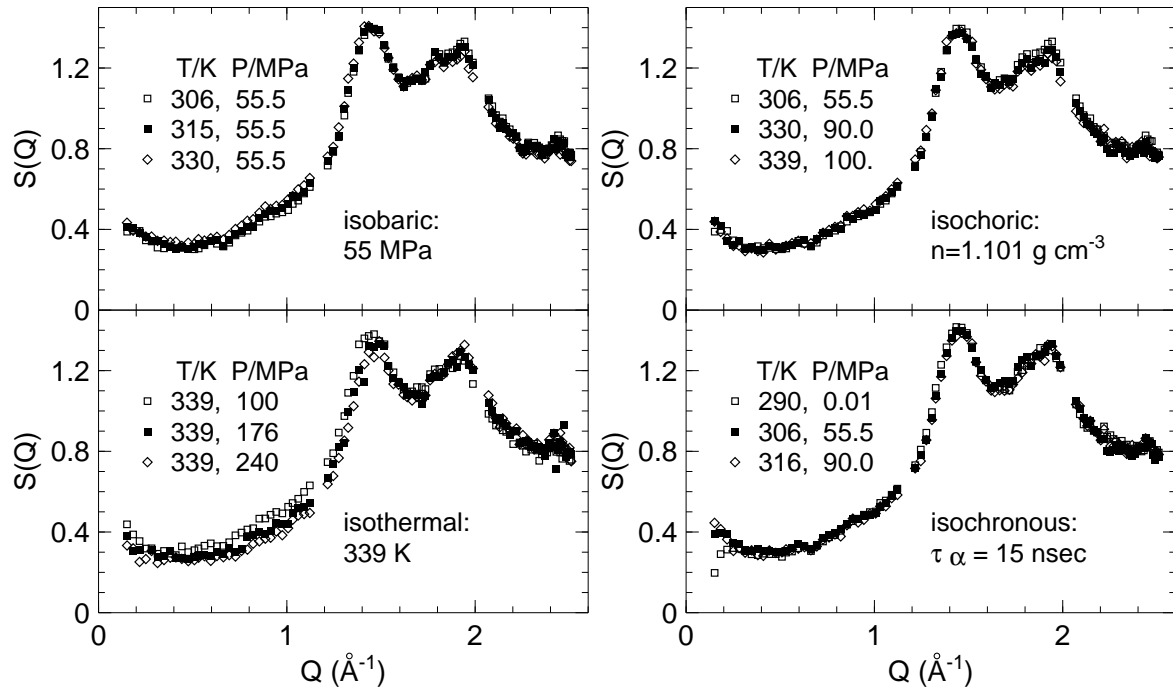


Figure 31. (*) Static structure factor $S(Q)$ under isobaric ($P = 55$ MPa), isothermal ($T = 339$ K), isochoric ($n = 1.101$ gcm $^{-3}$) and isochronic ($\tau_\alpha \simeq 15$ nsec) conditions.

(Möbbsauer–Lamb factor) as a function of density is shown for several wave numbers Q . At high pressures or densities, in the glassy phase, the elastic intensity remains rather constant. Thus, no harmonic evolution had to be taken into account as in the case of the temperature dependent measurements. Releasing the pressure, an anomalous decrease of the elastic intensity sets in and indicates the presence of a faster relaxation.

When constant pressure is applied the anomalous decrease shifts to higher temperatures with increasing pressure as apparent in figure 32 right which shows the isobaric DWF as a function of temperature for three different pressures at $Q = 1.8$ Å $^{-1}$.

Inspecting the isobaric decrease of f_Q in figure 32 at high temperatures more closely it seems that the slope of the decrease diminishes with increasing pressure and the transition range becomes broader. This slope is related to the strength of the fast β relaxation. One might speculate that the effect vanishes under extreme conditions. However, when the Q dependence of the elastic scattering is analyzed in terms of the mean square displacement $\langle r^2(T) \rangle$ extracted from the Debye Waller factors in a Gaussian approximation (inset of figure 32) this effect disappears. While around 200 K the $\langle r^2(T) \rangle$ are almost identical the anomalous increase shifts to higher temperatures. The pressure dependence of the mean square displacement can even be scaled to a master curve taking the thermodynamic shift dT_g/dP as the scaling parameter. Similar observations were made in the polymer polybutadiene [183, 184] while in polyisoprene the application of pressure separates an additional dynamic process [184].

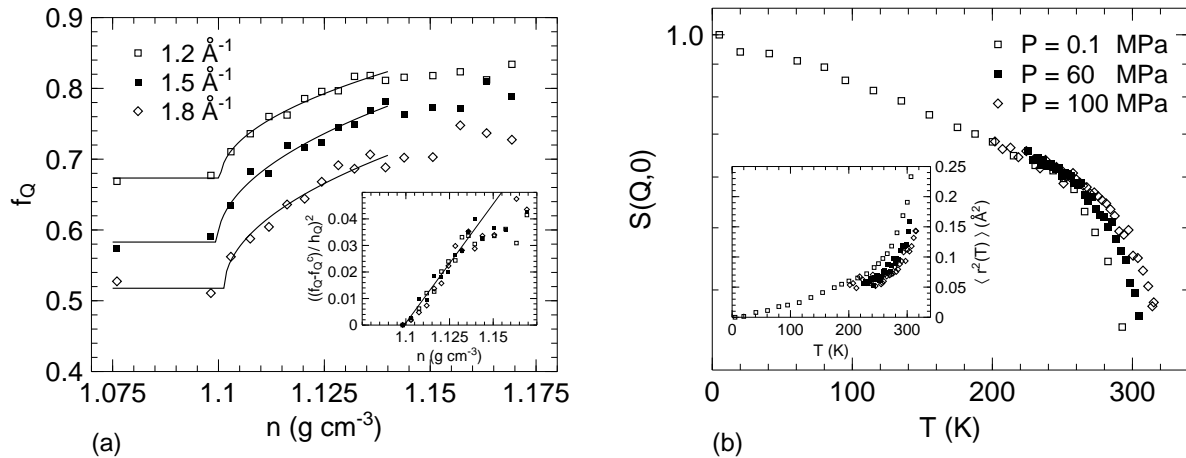


Figure 32. (a (*)) Plateau height f_Q of isothermal tagged particle correlations as a function of density at constant temperature $T = 301 \text{ K}$ for several Q -values. Solid lines are fits with a square root law leading to a critical density of $n_c \simeq 1.100 \text{ gcm}^{-3}$ which corresponds to a critical pressure of $P_c \simeq 42 \text{ MPa}$. Towards smaller densities the integrated α intensities are independent of pressure. The inset demonstrates the square root law in linearized form, based on [182]. (b (*)) Incoherent elastic scattering intensity (Möbbsbauer factor) as a function of temperature for different pressures at $Q = 1.8 \text{ \AA}^{-1}$. The linear behaviour at low temperatures is due to classical phonons $\exp(-Q^2 \langle r^2(T) \rangle)$ with $\langle r^2(T) \rangle \propto T$. With increasing pressure the anomalous decrease shifts to higher temperatures. Above a temperature $T_c(P)$ quasielastic broadening from structural relaxations comes into play and the integrated α intensity has to be taken into account. The inset shows the temperature dependence of the mean square displacement which contains the complete Q information.

7.4. Critical Correlations

We have already seen in the previous section that a kink in the Debye–Waller factor reveals the onset of the β -relaxation. The anomalous increase of the DWF above a certain density indicates that the β process is also strongly influenced by the pressure or density. This fast process is responsible for the decrease of elastic intensity on costs of inelastic intensity. Again the β -relaxation can be accessed directly on a TOF spectrometer like IN6. The spectral density below about 2 meV varies strongly with pressure. In this region the dynamic structure factor satisfies the factorization rule for all pressures as already demonstrated in figure 18.

The β -relaxation has been studied at variable pressure up to 240 MPa [182, 185]. The tagged-particle correlations in the compressed liquid also decay in two steps and can be described by the MCT scaling laws. Unfortunately, the used instruments IN16 and IN6 do not overlap (see table 2) and the dynamic range of IN6 alone is clearly not sufficient to warrant a four parameter fit. To get the pressure dependence of the β -relaxation amplitude h_Q and the cross-over times t_σ we use the results from the α -relaxation analysis to be presented in the following section in more detail. Besides the DWF f_Q we fix the line shape parameter to the known value $\lambda = 0.77$, which is compatible with

the frequency dependence ω^{1-a} ($a = 0.3$) shown in figure 18. The DWF was determined from a Kohlrausch fit to the long time tail of the low pressure data with fixed $\beta = 0.6$ and $\tau_Q(P)$. The insensitivity of line shape parameter λ to pressure is supported by broad band light scattering measurements on the glass formers Cumen [178] and Salol [186] where in isothermal and isobaric experiments identical line shapes were found. Figure 33 shows isothermal pressure dependent tagged particle correlation functions

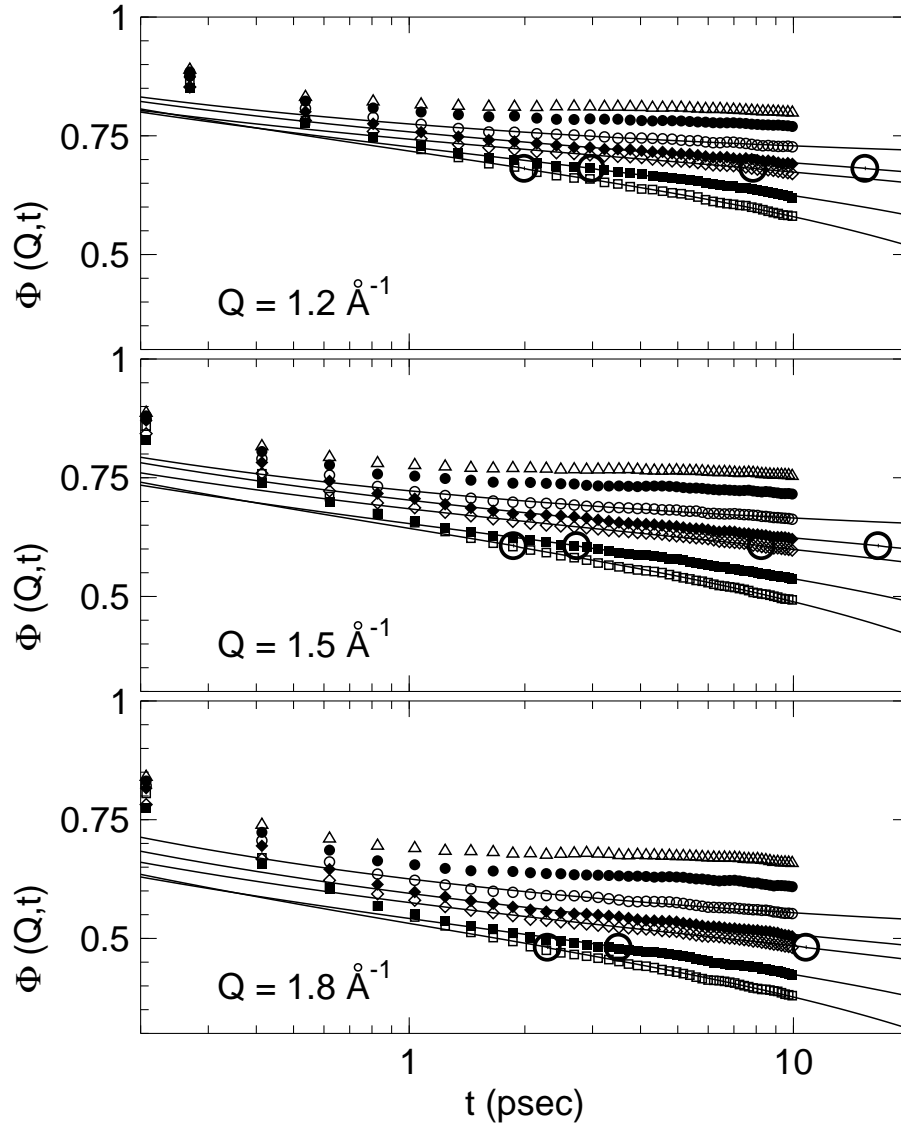


Figure 33. (*) Isothermal intermediate scattering function $S(Q, t)$ at 316 K obtained on IN6 at three different wave numbers $Q = 1.2, 1.5$ and 1.8 \AA^{-1} in the β -relaxation regime. Lines are fits with (17) with fixed line shape parameter $\lambda = 0.77$ and fixed plateau values (indicated by the thick circles). The pressures are from bottom to top: 0,1 MPa, 15 MPa, 45 MPa, 60 MPa, 90 MPa, 150 MPa and 200 MPa.

together with fits to (17). The correlation functions at the highest pressures decay to a

plateau which is constant in time and higher than the value for the liquid state: we are in the glassy state. For the lower pressures one recognizes a two step decay as in the temperature dependent case. While the first decay on the sub-pico-second time scale due to the microscopic dynamics is not covered by (17) it consistently describes the bending of $\Phi(Q, t)$ into and out of the intermediate plateau f_Q over about one decade depending on the pressure.

On approaching the cross-over from the liquid side, f_Q varies only weakly, whereas H_Q and t_σ should become singular. In figure 34 the power laws (18) are tested for two isotherms by plotting H_Q^2 and t_σ^{-2a} vs. P , with $a = 0.295$ determined by λ . Asymptotically, a linear behavior is observed allowing for a consistent determination

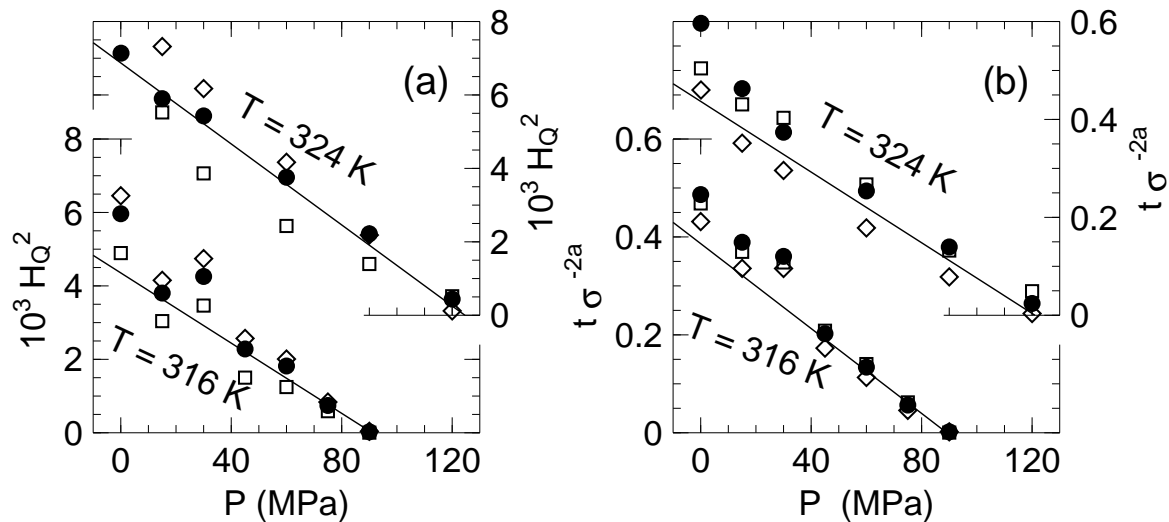


Figure 34. β -relaxation amplitude H_Q (a) and cross-over time t_σ (b) for two isotherms 316 and 324 K and three wave numbers $Q = 1.2(\square), 1.5(\bullet)$ and $1.8 \text{ \AA}^{-1}(\diamond)$. The data are linearized as H_Q^2 and t_σ^{-2a} according to (18); lines are fits to Q averaged values. Reproduced from [182].

of the mode-coupling crossover line $P_c(T)$ or $T_c(P)$.

Together with T_c at ambient pressure and the P_c values obtained from the elastic scans six points of the dynamic phase boundary $P_c(T)$ are obtained as summarized in table 4. The (P_c, T_c) line has a slope $dT_c/dP \simeq 0.26 - -0.28 \text{ K/MPa}$ which is in remarkable accord with the slope determined from α -relaxation, viscosity and $T_g(P)$ data: the mode-coupling crossover line is parallel to lines of equal α response (see figure 40). Lines of constant densities, however, have far steeper slopes of about 0.7 K/MPa . It confirms that the temperature influences the dynamics not only via the free volume. This finding is further illustrated by a direct comparison of isochoric correlation functions in figure 35. The loss of correlations is the faster the higher the temperature.

The above results imply that the dynamic crossover can be described by a single

Table 4. Critical pressure P_c and corresponding density n_c as function of temperature. The product $\Gamma_c = n\sigma^3(\epsilon/T)^{1/4}$ is found to be constant (its errors are estimated from $\Delta T_c = \pm 3$ K and $\Delta P_c = \pm 5$ MPa). The choice of $\sigma = 7.6$ Å and $\epsilon = 600$ K is explained in the text. The values in the lower part stem from temperature dependent elastic scans where the critical temperatures can only be estimated. Nevertheless, the (T, P) -combinations are compatible with the phase boundary.

T (K)	P_c (MPa)	n_c (nm ⁻³)	Γ_c
290	0.1	2.840	1.495(4)
301	42(3)	2.875	1.499(6)
316	90(7)	2.906	1.497(5)
324	123(7)	2.931	1.501(9)
306	60(3)	2.889	1.500(6)
317	100(5)	2.917	1.503(12)

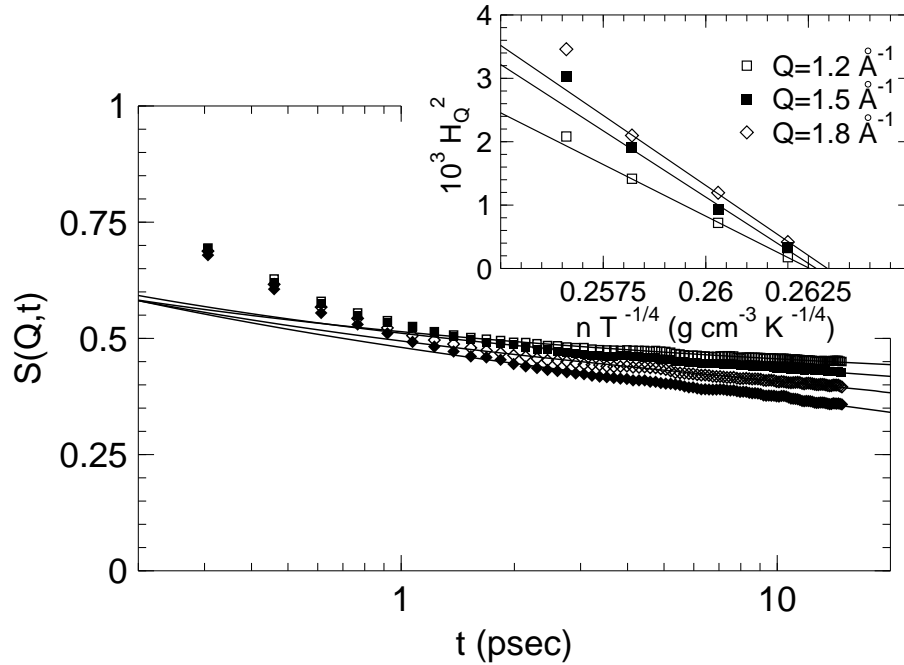


Figure 35. (*) Isochoric tagged particle correlation function $\Phi(Q, t)$ for $Q=1.8$ Å⁻¹ at a density $n \simeq 1.083$ g/cm³. The (T, P) combinations are from top to bottom: (292,0.1); (300,12); (310,26.5); (319,39) in K and MPa. Lines are fits with a fixed $t_\sigma(\Gamma)$. The inset shows the results for the β -relaxation amplitude H_Q in linearised form for three wave numbers all extrapolating to a consistent single value of $nT^{-1/4} \propto \Gamma$. For explanation of Γ see text.

separation parameter $\sigma(T, P)$ which, however, does not depend on density alone. Instead, it appears that density n and temperature T can be condensed into an effective coupling $\Gamma \propto nT^{-1/4}$ which is constant within experimental error as shown in table 4. Furthermore, constraint fits to all individual $\Phi(Q, t; T, P)$ confirm that the temperature

and pressure dependence of the amplitude and the cross-over time can be described by the power law (18) in conjunction with just one separation parameter $\sigma = (\Gamma - \Gamma_c)/\Gamma_c$ (figure 35). At least in a certain neighbourhood of $P_c(T)$ this parameter is linear in the effective coupling $\Gamma \propto nT^{-3/k}$ which is known to characterise equilibrium properties of a dense soft sphere fluid with repulsive core potentials of the Lennard–Jones r^{-k} type [187]. Note, that a plot $\log n_c$ vs. $\log T_c$ yields a slope of 0.27 very close to the theoretically expected value $1/4$ for $k = 12$.

In a supercooled and compressed liquid, we are actually in a high-density regime where the static structure factor $S(Q)$ is determined mainly by the repulsive part of the potential [187, 188, 189]. Since this repulsive part can be modeled well by a soft sphere system our results are thus evidence that for the glass transition subtle changes in the static structure factor are responsible for the slowing down of the dynamics. This view is also supported by computer simulations of binary soft sphere [190, 191, 192] and Lennard–Jones [148] systems, in which the glass transition was found to occur at constant Γ_c . It is astonishing that these results apply literally in a complex molecular liquid like OTP. In fact, the comparison with a Lennard–Jones liquid can be made almost quantitative. To do so, we need the two parameters of the 6 – –12 potential: a van der Waals diameter σ and a potential depth ϵ . $\sigma = 7.6 \text{ \AA}$ is estimated from structural information [86]. This is in good accord with the prepeak in the static structure factor at $Q \simeq 0.85 \dots 0.9 \text{ \AA}^{-1}$ [42, 157] and the scaling factor needed to describe the Q dependence of the critical Debye–Waller factors f_Q^c and the amplitudes h_Q in figure 22. A potential depth $\epsilon = 600 \text{ K}$ has been determined by calibrating a three-site OTP model to experimental density and diffusivity [135]. Using this input, we obtain $\Gamma_c = 1.50$ (table 4) which is closer to the Lennard–Jones result $\Gamma_c^{\text{LJ}} \simeq 1.25$ [146, 148] than one could reasonably expect.

Bengtzelius [146] calculated $T_c(n)$ for different densities for a Lennard–Jones system. In order to compare our $T_c(n)$ with his result we rescale his axis such that they coincide at P_0 . Our slope ($5.02 \cdot 10^{-4} \text{ g cm}^{-3}$) is in good accord with the theoretical one ($6.22 \cdot 10^{-4} \text{ g cm}^{-3}$). From the rescaling we get the two Lennard–Jones parameters: the potential depth $\epsilon/k_B \simeq 608 \text{ K}$ which astonishingly is the value found in the simulations [135] and the diameter $\sigma \simeq 7 \text{ \AA}$ being in good accord with the van der Waals radius.

We have found in the pressure and temperature dependent measurements of the static structure factor that along an isochronous line ($\tau_\alpha = \text{const.}$) $S(Q)$ does not change significantly (figure 31). According to the theory the spectra $S(Q, \omega)$ should all be identical (apart from the possibility of a trivial shift in the overall time scale t_0). In order to test this behaviour directly we measured the dynamics for several combinations of temperature and pressure leading to the same Γ (and not as usual along isothermal, isochoric or isobaric paths). A direct comparison of the dynamic structure factors in figure 36 shows indeed that the spectra are identical within statistical accuracy. This implies that the plateau height f_Q , the β -relaxation amplitude h_Q and the cross-over time t_σ are identical along a constant Γ , *i. e.* along a constant τ_α -line. Note, that for our purposes it is sufficient to compare $S(2\theta, \omega)$ after subtracting the empty can spectra.

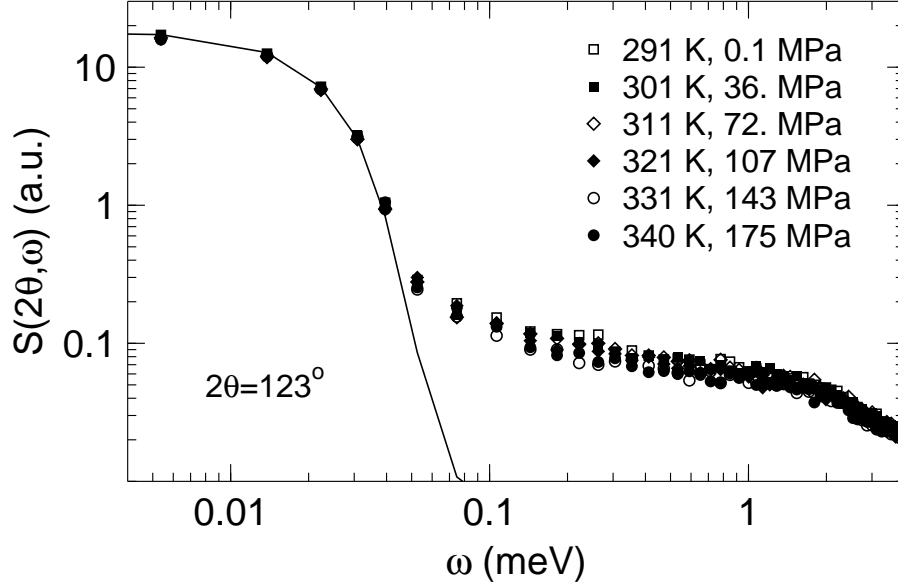


Figure 36. (*) Incoherent dynamic structure factor $S(2\theta, \omega)$ at a fixed scattering angle $2\theta = 123^\circ$ for several combinations of temperature and pressure leading to the same value for Γ . Note, the spectra are identical within experimental error.

Table 5. Connection between expansivity α , compressibility β and the repulsive part of the potential expressed via (29) along the dynamic phase boundary *i. e.*

T (K)	P_c (MPa)	$\alpha 10^4 / \text{K}^{-1}$	$\beta 10^4 / \text{MPa}^{-1}$	$T_c(\frac{\beta}{dT/dP _\tau} - \alpha)$
290	0.1	7.2	5.0	0.31
301	42(3)	6.4	4.4	0.28
306	60(3)	6.1	4.1	0.26
316	90(7)	5.7	3.8	0.25
317	100(5)	5.6	3.7	0.24
324	123(7)	5.3	3.6	0.24

Interestingly, a relation between the effective coupling Γ or, more exactly, the repulsive part of the potential and some macroscopic quantities can be established. To do so we assume the specific volume $v(T, P)$ to be linear dependent on temperature and pressure via the thermal expansivity α and the isothermal compressibility β :

$$v(T, P) = v(T_c, 0)(1 + \alpha(T - T_c) - \beta P_c(T)) \quad (28)$$

with T_c the critical temperature and $P_c(T)$ the critical pressure. At the phase boundary $\Gamma^{-1} = vT^{1/4} = \text{const.}$, thus we can derive the following equation using $T = T_c(1 + (T - T_c)/T_c)$ and developping in a Taylor series up to first order

$$T_c(\frac{\beta}{dT/dP|_\tau} - \alpha) \simeq \frac{1}{4} \quad (29)$$

where we have used the fact that the phase boundary follows

$$P_c(T) = \frac{(T - T_c)}{dT/dP|_\tau}. \quad (30)$$

Using our (T_c, P_c) combinations, the values for the expansivity and compressibility at these [46] and $dT/dP|_\tau \simeq 0.28 \text{ K/MPa}$ gives us the result in table 5. Astonishingly, equation (29) holds quite good indicating a deeper link between the microscopic repulsive part of the potential and the macroscopic quantities expansivity and compressibility.

It would indeed be interesting to check on other fragile glass forming liquids, whether the critical mode-coupling phase boundary is parallel to lines of constant α -relaxation time and whether an effective coupling and a link to the expansivity and the compressibility can be established in a similar manner as we found for OTP.

7.5. α -Relaxation

On the BS instrument IN16 we measured the slowing down of the structural α -relaxation as a function of pressure. In a first survey, we could show that the mean relaxation time follows the pressure dependence of the viscosity. The shape of the α -relaxation spectra was then determined in some long-running scans. At three different points (T, P) of equal viscosity, the quasielastic broadening of all spectra coincide as shown in figure 37 for three values of Q . The microscopic relaxation time is proportional to the macroscopic viscosity η and the spectral distribution is quite independent of pressure. This is confirmed from photon correlation [48] and dielectric measurements [60].

By construction of a master curve for isothermal spectra at 320 K we can further illustrate the invariance of the line shape and the viscosity scaling. Motivated by the result of figure 37 we use viscosity data [28] to rescale the times $t \rightarrow \hat{t} = t\eta(P_0)/\eta(P)$ with $P_0 = 0.1 \text{ MPa}$ similar to the procedure described in section 6.5. The rescaled $\hat{\Phi}(Q, \hat{t})$ coincide over two decades as shown in figure 38 for three Q values. The scaling is well satisfied. The α -relaxation amplitude and the line shape parameter β as derived from the iterative procedure are shown in figure 39. Both parameters are nearly independent of pressure, which in turn justifies the analysis of the β -relaxation presented in the previous section. The stretching parameter β is similar to that derived from previous investigations at atmospheric pressure [82]: The distribution of relaxation times is pretty much unaffected by the pressure and temperature changes. The mean relaxation times $\langle\tau(P)\rangle$ as obtained from Kohlrausch fits with fixed $\langle A_Q \rangle_P$ and β and after elimination of the Q dependence are also shown in figure 39. It follows the same pressure dependence as the viscosity, in agreement with the isoviscous measurements.

Thus, a time-temperature-pressure superposition principle holds. It is well established by PCS and dielectric spectroscopy in OTP as well as in some other fragile liquids [70, 193]. Our measurements extend the validity of this scaling principle down to the picosecond time range.

The pressure dependence of isochronous relaxation times is compiled in figure 40. Lines of isochronous α -relaxation times are connected by the same slope of about

$(dT/dP)_\tau \simeq (0.28 \pm 0.01)$ K/MPa over about twelve orders of magnitude regardless of the time scale. At long times the pressure dependence of the glass transition temperature (dT_g/dP) [45], is the same as in the second to microsecond time range covered by photon–correlation spectroscopy [48] and dielectric spectroscopy [60] down to the sub–nanosecond regime covered here by neutron scattering.

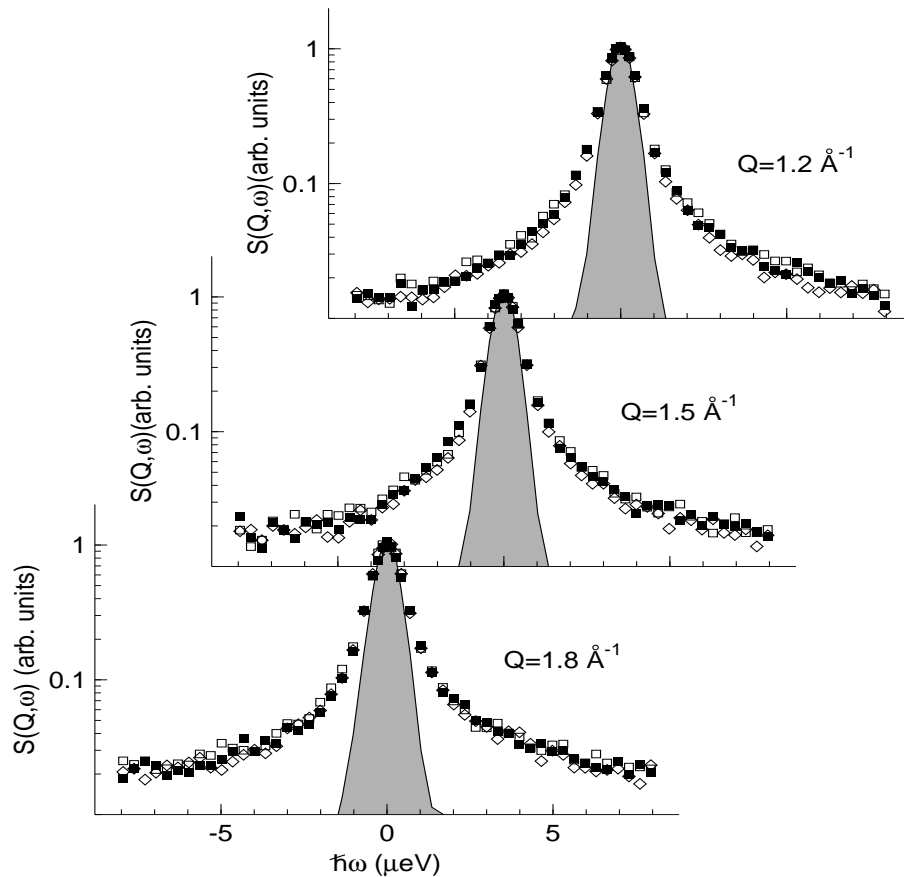


Figure 37. (*) α -relaxation spectra from IN16 at $Q = 1.2, 1.5$ and 1.8 \AA^{-1} for three combinations of temperature and pressure leading to approximately the same viscosity. The spectra are scaled to their value at $\omega = 0$. The hatched area represents the measured resolution function. The (T, P) combinations are: 306 K, 0.1 MPa (\square); 320 K, 50 MPa (\blacksquare) and 335 K, 100 MPa (\diamond).

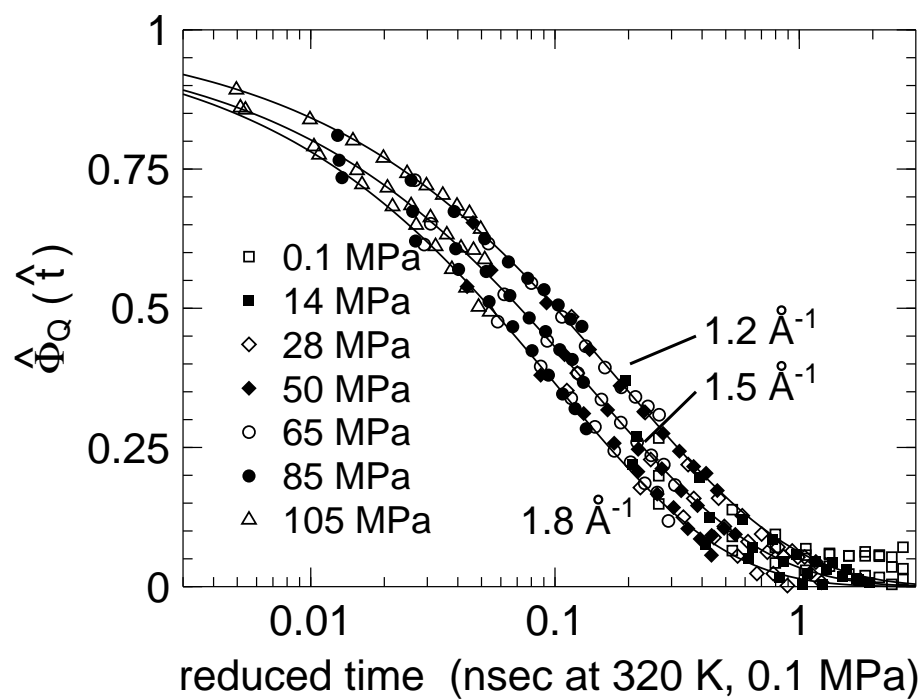


Figure 38. (*) Master curves $\hat{\Phi}_Q(\hat{t})/A_Q(P)$ for the isothermal α -relaxation of the tagged particle fluctuations at 320 K and different pressures, obtained by rescaling times with viscosity $\eta(P)$.

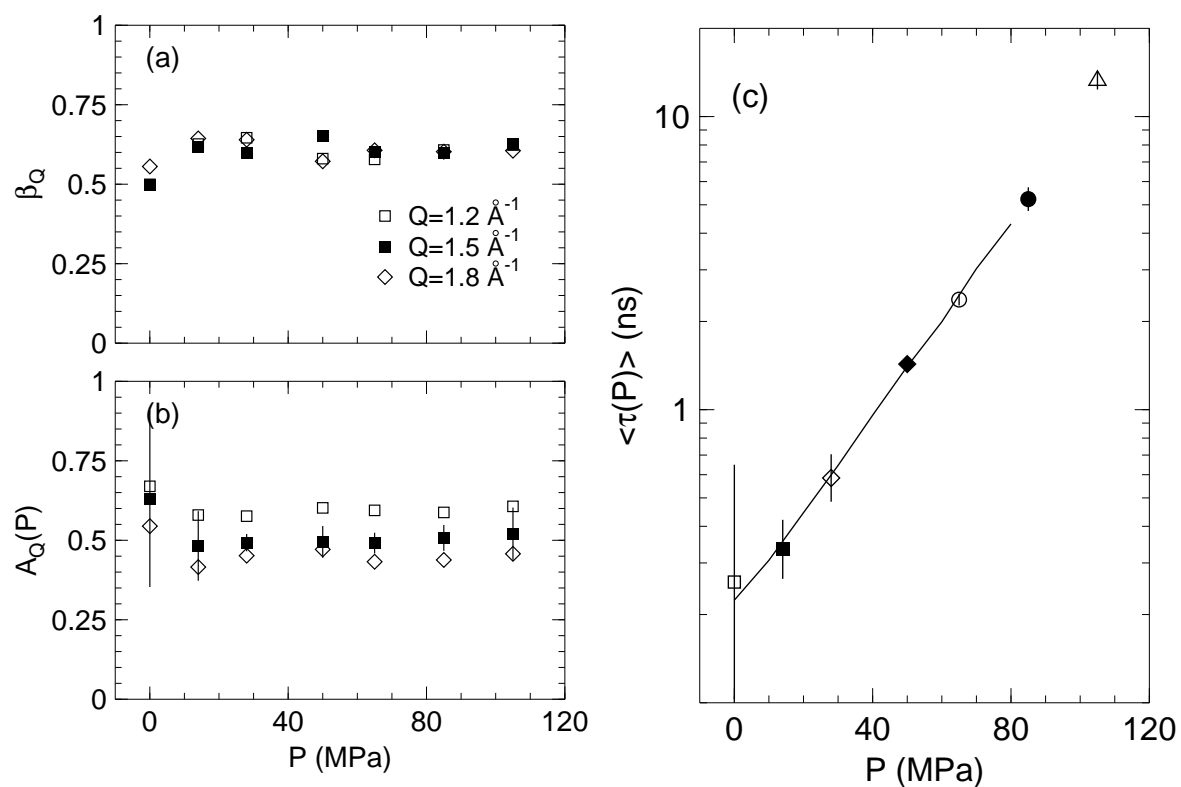


Figure 39. (*) Kohlrausch parameters β_Q (a), A_Q (b) and $\langle \tau \rangle$ (c) as obtained from the scaling analysis as a function of pressure. In each fit, two parameters were fixed at the values obtained from the master curve analysis. Amplitude A_Q and stretching exponent β_Q are roughly independent of pressure in the liquid state. The mean relaxation time $\langle \tau \rangle$ scales with viscosity (line).

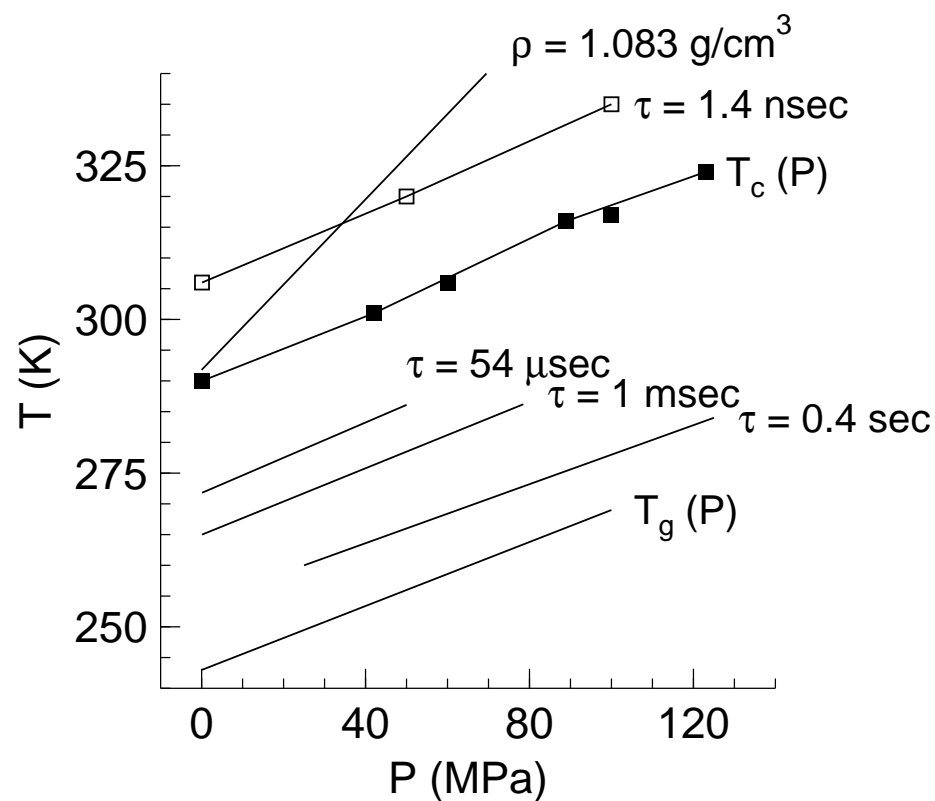


Figure 40. (*) Pressure and temperature dependence of isochronous α -relaxation times. Note that from T_g corresponding to relaxation time of the order of 100sec down to nsec all slopes are identical. In particular the dynamic phase boundary $T_c(P)$ is parallel to lines of equal α response. Constructed using values from [45, 48, 60].

8. Vibrational Dynamics [36]

When the dynamic anomalies of the glass transition are discussed it is particularly important for molecular glasses, which have a large number of internal degrees of freedom, to study at least qualitatively the vibrational mode structure. This seems to be even more important in view of the fact that low-frequency vibrational features – for obscure reasons called Boson peak – persist well into the supercooled phase.

This can be done by comparison of the absolute frequency scales of the vibrational density of states between the ordered and disordered state. From single crystal dispersion measurements – if available – information about low-energy internal modes and hybridisation of external and internal modes can be obtained.

8.1. Single Crystal: Phonon Dispersions

The phonon dispersions of single crystal OTP at 200 K along the three main symmetry directions $[100]$, $[010]$, and $[001]$ are presented in figure 41. Some optic-like phonons are detected as well, as an example, the lowest optic branch in $[010]$ direction is included in figure 41. However, for a detailed study of them thermal neutrons instead of cold ones would be needed. In the small Q limit the sound velocities of acoustic excitations

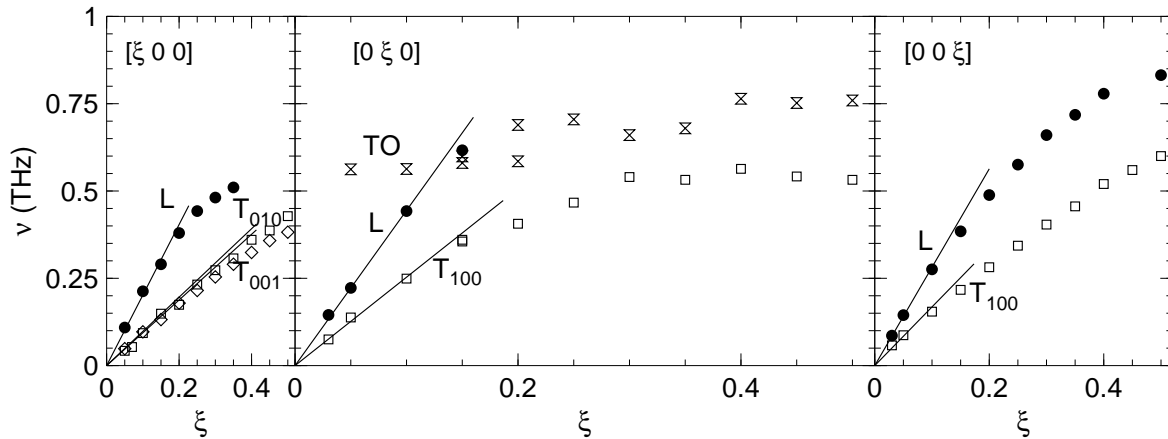


Figure 41. Phonon dispersion relations of crystalline OTP as measured on the triple axis spectrometer IN12 at 200 K. The wave vectors are given in reciprocal lattice units, excitation energies in THz ($1 \text{ THz} = 33.36 \text{ cm}^{-1} = 4.1357 \text{ meV}$). Taken from [36].

obtained from the initial slope are summarized in table 6. In all lattice directions, longitudinal sound modes are almost twice as fast as transverse modes. The single crystal data may also be compared with sound velocities in the glass. Results from Brillouin light scattering are summarized in table 7. Taking the simple arithmetic average over the three crystal axes, the mean longitudinal and transverse sound velocities $\langle v_{L,T} \rangle$ exceed those of the glass by about 20 % and 27 %, respectively.

Table 6. Sound velocities (in km/s) for three phonon branches and different lattice directions, obtained from linear fits to the low- Q limit of the measured phonon dispersions.

	$v_{[100]}$	$v_{[010]}$	$v_{[001]}$	$\langle v \rangle$	$\langle v^{-3} \rangle^{-1/3}$
v_L	3.71	2.68	3.30	3.23	3.11
v_{T_1}	1.82	1.52	1.97	1.75	1.71
v_{T_2}	1.67	–	–		

Table 7. Sound velocities in the glass as measured by Brillouin scattering, using visible light or X-rays.

T (K)	v_L (km/s)	v_T (km/s)	method	reference
220	2.94	1.37	light	[117]
223	2.63		light	[119]
200	2.70		X-rays	[121]

8.2. Glass versus Polycrystal: Density of Vibrational States

Without crystalline order, it is no longer possible to measure selected phonon modes with well-defined polarization and propagation vector. For polycrystalline or amorphous samples, the distribution of vibrational modes can be conveyed only in form of a spectral density of states (DOS).

The DOS of glassy and crystalline OTP at 100 K are shown in figure 42. They were calculated directly from the spectra at the highest scattering angles $S(2\theta, \omega)$ without interpolation to constant Q . Multiphonon contributions were calculated by repeated convolution of $g(\omega)$ with itself and subtraction from $S(2\theta, \omega)$ in an iterative procedure described in detail in [107]. Comparing our results with model calculations [194], we assign all vibrations below ν_g to the 16 degrees of freedom needed to describe the crystal structure. For 16 low-lying modes in a molecule with 32 atoms, we expect an integrated DOS

$$\int_0^{\nu_g} d\nu g(\nu) = \frac{16}{32} = 0.5. \quad (31)$$

Rather broad distributions are found for both phases showing a pronounced gap above $\nu_g \simeq 5$ THz ($1 \text{ THz} = 33.36 \text{ cm}^{-1} = 4.1357 \text{ meV}$). In the glass a first shoulder around 1.5 THz is followed by a second at 3.5 THz in accordance with results from Raman studies [115, 116]. As expected, the crystal DOS is more structured, in particular in the low energy region. Distinct peaks at 0.6, 0.8, 1.1 and 1.5 THz become apparent. They are due to strong contributions from zone-boundary modes (figure 41). Compared to the glass, significant density is missing in the low energy region and in the range from 1.5 to 3 THz, and reappears at higher frequencies around 3.5 THz. The gap for $\nu > 5$ THz

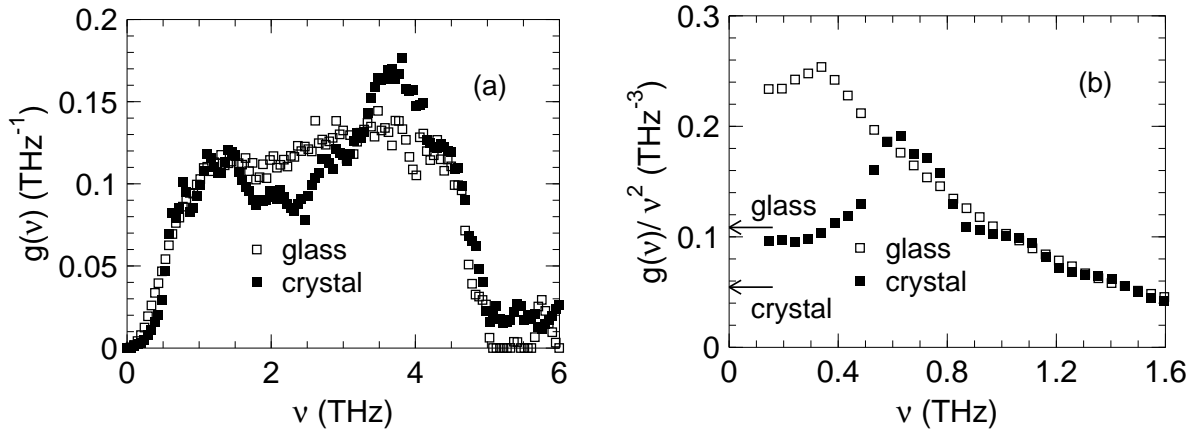


Figure 42. (a) Density of vibrational states of glassy and crystalline OTP at 100 K. (b) To emphasize the excess density of states of the glass over the crystal $g(\nu)/\nu^2$ is shown. The arrows mark the Debye limit $\nu \rightarrow 0$ calculated from sound velocities and densities at 220 K for the glass and at 200 K for the crystal. Taken from [36].

common for both states and indicates a separation from high energy intramolecular modes.

The DOS of the polycrystalline sample is in accord with the measured dispersion of the single crystal: A small shoulder at 0.4 THz can be attributed to the transverse acoustic zone-boundary phonons in [100] direction, and the main peak at 0.6 THz corresponds to the transverse acoustic zone-boundary phonons in the other two lattice directions. The peak at 0.8 THz reflects the longitudinal acoustic zone-boundary phonon in [001] direction and the transverse optic in [010] direction.

In order to show the low energy modes on an enhanced scale, we plot in figure 42 $g(\nu)/\nu^2$ which in the one-phonon approximation is proportional to $S(Q, \nu)$ itself. In this representation, the excess of the glass over the crystal becomes evident. A well defined frequency peak appears around 0.35 THz which is down shifted with respect to the first peak of the crystal at 0.6 THz and superposed to a long tail which is similar for both, glass and crystal. Note that the maximum of the boson peak at 0.35 THz is located below the lowest acoustic zone-boundary phonons in the crystal.

Another dynamic observable which can be obtained from neutron scattering is the atomic mean square displacement $\langle r^2(T) \rangle$. Roughly speaking, $\langle r^2(T) \rangle^{3/2}$ measures the volume to which an atom remains confined in the limit $t \rightarrow \infty$. For a large class of model situations (harmonic solid, Markovian diffusion, ...) it can be obtained directly from the Gaussian Q dependence of the elastic scattering intensity

$$S(Q, \nu=0) = \exp(-Q^2 \langle r(T)^2 \rangle). \quad (32)$$

For a harmonic solid,

$$\langle r(T)^2 \rangle = \frac{\hbar^2}{6Mk_B T} \int_0^\infty d\nu \frac{g(\nu)}{\beta} \coth\left(\frac{\beta}{2}\right) \quad (33)$$

(with $\beta = h\nu/k_B T$) crosses over from zero-point oscillations $\langle r^2(0) \rangle$ to a linear regime $\langle r^2(T) \rangle \propto T$. Note, for a meaningful application of (33), we have to assume the rigid-body limit (Sect. 3.1, Ref. [107]). Therefore, M has to be taken as the average atomic mass which in the case of OTP is 7.2. In any real experiment, which integrates over the elastic line with a resolution $\Delta\nu$, one actually measures atomic displacements within finite times $t_\Delta \simeq 2\pi/\Delta\nu$.

Figure 43 shows mean square displacements of OTP, determined according to (32) from elastic back-scattering (fixed window scans on IN13, with $t_\Delta \simeq 100 - 200$ psec) and from Fourier-deconvoluted time-of-flight spectra (taking the plateau $S(Q, t_\Delta)$ with $t_\Delta \simeq 5 - 10$ psec from Fourier transformed IN6 data). For the glassy sample, a direct comparison can be made and shows good agreement between IN6 and IN13.

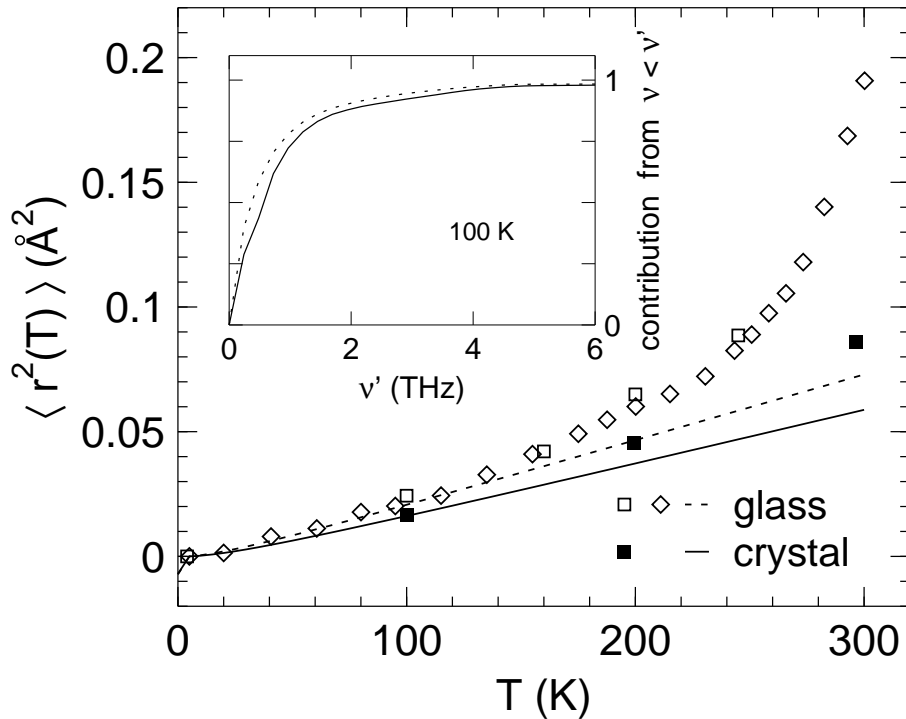


Figure 43. Mean square displacement $\langle r^2(T) \rangle$ of glassy OTP from elastic back-scattering (IN13, \diamond) and from time-of-flight spectra (IN6, plateau value of $S(Q, t)$, \square). For comparison, IN6 data of polycrystalline OTP are also shown (\blacksquare). The lines are calculated from the densities of states at 100 K of the glass (dashed) and the polycrystal (solid line). The inset shows the relative value of $d = \langle r^2 \rangle^{1/2}$ at 100 K for the crystal and the glass when the integral (33) is restricted to modes with $0 < \nu < \nu'$. Taken from [36].

The lines in figure 43 are calculated through (33) from the DOS at 100 K. For low temperatures, the $\langle r^2(T) \rangle$ are in full accord with the values determined through (32). This comparison can be seen as a cross-check between the analysis of elastic and inelastic neutron scattering data.

Equation (33) not only gives the absolute value of $\langle r^2(T) \rangle$, but enables us also to read off which modes contribute most to the atomic displacement. To this end, we restrict the integration (33) to modes with $0 < \nu < \nu'$. The inset in figure 43 shows the relative value $\langle r^2(\nu'; T) \rangle^{1/2} / \langle r^2(\nu; T) \rangle^{1/2}$ for $T = 100$ K as function of ν' . Modes below 0.6 THz in the crystal, or 0.4 THz in the glass contribute about 55% to the total displacement; 90% are reached only at about 2 THz. This means that the modes which are responsible for the mean square displacement and the Debye–Waller factor are not rigid body motions alone, but contain a significant contribution from other modes.

Anyway, one immediately recognizes that for all temperatures the mean square displacement in the glass is larger than in the crystal. For higher temperatures the measured mean square displacements are clearly larger than expected from harmonic theory. These anharmonic contributions to $\langle r^2(T) \rangle$ start around 140–150 K. Around the same temperature deviations from the proportionality $\langle r^2(T) \rangle \propto T$ can be observed in coherent elastic scans and in the Mößbauer experiment [162] (figure 15 in section 6.3). In addition, around 140–150 K the temperature dependence of the experimental specific heat $c_P(T)$ [43] shows a slight change for both glass and crystal.

Anharmonicities can directly be observed via the temperature dependence of the density of states. With increasing temperature the first moment, which provides a measure for the center of gravity, clearly shifts to lower frequencies for the glass and even more for the crystal. Note however, the strong increase above 240 K in the glass is connected with the glass transition.

Our vibrational density of states can also be checked against the heat capacity, which for a harmonic solid is given by the integral

$$c_P(T) \simeq c_V(T) = N_{\text{at}} R \int_0^\infty d\nu g(\nu) \frac{(\beta/2)^2}{\sinh^2(\beta/2)}. \quad (34)$$

With a Debye DOS, this yields the well-known $c_P \propto T^3$. Therefore, in figure 44 experimental data [43] for the specific heat of glassy and polycrystalline OTP are plotted as c_P/T^3 . In this representation, a boson peak at 0.35 THz is expected to lead to a maximum at about 4 K.

The lines are calculated through (34) from the neutron DOS. They agree with the measured data for both glass and crystal in absolute units and over a broad temperature range. Similar accord has been reported for a number of other systems [115, 195, 196, 105, 197].

At higher temperatures, the heat capacities of crystalline and glassy OTP differ only little (*e.g.* at 200 K: $c_P^{\text{cryst}} = 182.8 \text{ J mol}^{-1} \text{ K}^{-1}$ and $c_P^{\text{glass}} = 186.1 \text{ J mol}^{-1} \text{ K}^{-1}$ [43]). Towards higher frequencies, the DOS becomes less sensitive to the presence or absence of crystalline order and remaining differences (clearly visible in figure 42) are largely averaged out by the integral (34).

Altogether, these observations suggest that the mode structure in the glass and the crystal is quite similar except for an overall softening in the glass. Concerning the above presented analysis of quasielastic scattering in the supercooled liquid we can state that above 0.6 THz a very large portion of inelastic intensity in $S(Q, \nu)$ of glassy OTP must

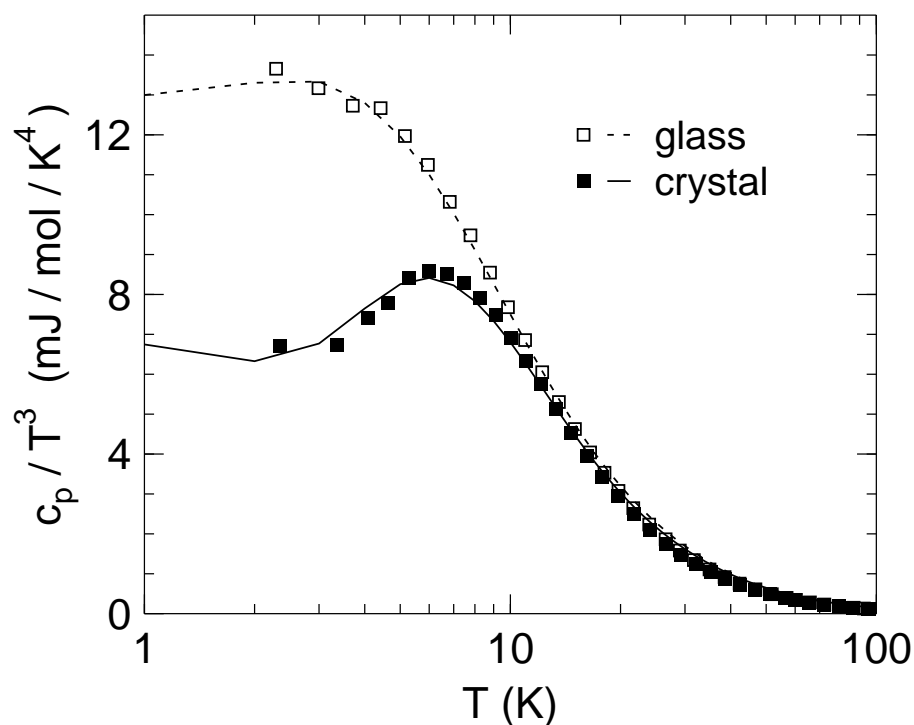


Figure 44. Experimental heat capacities c_p/T^3 of glassy (□) and crystalline (■) OTP [43], compared to c_p/T^3 calculated from the density of vibrational states $g(\nu)$ at 100 K of the glass (dashed line) and the polycrystal (solid line). Taken from [36].

arise from optic modes. Hybridisation and coupling between inter- and intramolecular modes plays an important role for frequencies higher than 0.6 THz [198, 115]. As a consequence, the quasielastic scattering, which is confined to below 0.25 THz (1 meV), is clearly dominated by rigid-body motions and the analysis in terms of relaxations remains reasonable.

9. Conclusions

As the reader has seen in the preceding sections, neutron scattering experiments on the fragile van der Waals liquid Orthoterphenyl provide clear evidence for a dynamic cross-over from a liquid-like to a solid-like motional mechanism occurring around the critical temperature T_c .

Mode-coupling theory gives a quantitative consistent description of the dynamics in the supercooled state. Time-temperature-pressure superposition, known from Hz–MHz spectroscopy, is valid down to the picosecond time range, where macroscopic properties of the material evolve from their microscopic dynamics. Spectral line shapes observed by coherent and incoherent neutron scattering experiments are invariant under temperature and pressure variations. The mean relaxation time is proportional to the viscosity and states of equal kinetics are connected by the same slope dT/dP , regardless of the time scale.

Temperature and pressure dependent Debye–Waller factors show an anomalous decrease that can be described by a square root law. Whether or not the square root law results in a sharp singularity is however sometimes not compelling, in particular for small wave numbers Q or at the structure factor maximum, *i. e.* where the effect is expected to be very small anyway. The lost scattering intensity reappears as a quasielastic process and is identified with the β -relaxation whose time correlations follow the predicted scaling behaviour. More importantly, all correlation functions can be described by the same MCT β correlator (17) with *one consistent set* of exponents. The fit parameters show the predicted Q dependence and consistently converge to the same critical $T_c(P)$. They allow the unambiguous determination of a dynamic crossover line $T_c(P)$. This line is parallel to the lines of equal viscosity: α - and β -relaxation are driven by the same parameter. At least in a certain neighbourhood of $T_c(P)$ this parameter is linear in the effective coupling $\Gamma \propto nT^{-1/4}$ which in turn ultimately depends on the short range interaction of the molecules. Our experiments have also allowed for to separate temperature from density effects and to relate at least qualitatively dynamic and structural changes.

Furthermore, we have excluded any intramolecular origin of the observed anomalies by measurement on partially deuterated samples and by comparison of frequency scales of the glass and the crystal. Any structural reason is excluded by the smooth temperature and pressure evolution of the static structure factor $S(Q)$. Also in that sense OTP represented a good model system for testing the predictions of MCT.

However, mode-coupling theory does not describes some other important aspects like slow processes in the vicinity of T_g , slow secondary Johari–Goldstein β -relaxation [59], cooperativity, dynamic heterogeneity [199] and the vibrational dynamics. We should also mention that in a molecular liquid the first critical exponent a has never been observed purely and that the appearance of the so-called "knee" below the critical temperature is still an open question.

Experimentally, the identification of the dynamic transition is far from being trivial

and the comparison of neutron scattering and MCT predictions still remains qualitative in many aspects. Complicated spectral shapes have to be measured with high precision, a good Q resolution and over a large time or frequency window. We presented two different approaches that partly satisfy these demands: the combination of different spectrometers and the analysis using mastercurves.

On a fundamental level, the presence of a de Gennes type narrowing in OTP-d₁₄ reinforces our very basic assumption that incoherent and coherent neutron scattering probe self and density correlations of OTP molecules, respectively. Of course, we measure correlations of single H, D and C atoms which, in addition to a translational component, also contain contributions from rotational motion relative to the center-of-mass. Whether such contributions are relevant and more sophisticated MCT extensions have to be used can only be decided by joint use of different experimental techniques including molecular dynamics simulations with appropriate models.

For the time being we believe that in our study we have exploited the very limits of neutron scattering in its present state of the art. We have also demonstrated that some very interesting experiments like the separation of coherent and incoherent scattering are feasible, but better and more accurate results have to await new high-flux neutron sources. The total efficiency has to be increased by at least one order of magnitude by increasing the incoming flux and / or by a much higher spectrometer efficiency. Upgrading and development of all types of spectrometers is currently under way.

Other methods, *e. g.* synchrotron radiation, optic Kerr effect, impulsive stimulated light scattering or high frequency dielectric spectroscopy, among others, seem also to be very promising for the investigation of glassy dynamics in particular as they couple to different degrees of freedom. They may open the way to a comparison of experimental data with more sophisticated versions of the theory.

Acknowledgments

The author is particularly grateful to his colleagues F. Fujara, W. Petry, H. Schober and J. Wuttke for this fruitful and long-standing collaboration. Much of the deuterated OTP and the single crystals have been prepared by H. Zimmermann. I owe special thanks to C. Alba-Simionesco, W. Götze, W. Kob, F. Sciortino and H. Sillescu for many discussions and suggestions. I am also very grateful to J. Seelig for the hospitality in his group during the completion of the manuscript. Financial support by the Bundesministerium für Bildung und Forschung (BMBF) under project numbers 03SI2MAI, 03FU4DOR4 and 03FU5DOR1 and by the Institute Laue Langevin, Grenoble is gratefully acknowledged.

References

- [1] M. H. Cohen, D. Turnbull, *J. Chem. Phys.* **31**, 1164 (1959).
- [2] M. H. Cohen, G. S. Grest, *Phys. Rev. B* **20**, 1077 (1979).
- [3] J. H. Gibbs, E. A. Di-Marzio, *J. Chem. Phys.* **28**, 373 (1958).
- [4] G. Adam, J. H. Gibbs, *J. Chem. Phys.* **43**, 139 (1965).
- [5] E. Leutheusser, *Phys. Rev. A* **29**, 2765 (1984).
- [6] U. Bengtzelius, W. Götze, A. Sjölander, *J. Phys. C* **17**, 5915 (1984).
- [7] W. van Meegen, S. M. Underwood, *Phys. Rev. Lett.* **70**, 2766 (1993).
- [8] W. van Meegen, S. M. Underwood, *Phys. Rev. E* **47**, 248 (1993).
- [9] W. van Meegen, S. M. Underwood, *Phys. Rev. E* **49**, 4206 (1994).
- [10] W. Götze, *J. Phys. Condens. Matter* **11**, A1 (1999).
- [11] F. Volino, H. Gerard, G. Gebel, *Ann. Phys. Fr.* **22**, 181 (1997).
- [12] F. Mezei, W. Knaak, B. Farago, *Physica Scripta* **T19**, 363 (1987).
- [13] W. Knaak, F. Mezei, B. Farago, *Europhys. Lett.* **7**, 529 (1988).
- [14] E. Kartini, M. F. Collins, B. Collier, F. Mezei, E. C. Svensson, *Phys. Rev. B* **54**, 6292 (1996).
- [15] J. Wuttke, M. Ohl, M. Goldhammer, S. Roth, U. Schneider, P. Lunkenheimer, R. Kahn, B. Ruffe, R. Lechner, MA. Berge, *Phys. Rev. E* **61**, 2730 (2000).
- [16] D. Richter, B. Frick, B. Farago, *Phys. Rev. Lett.* **61**, 2465 (1988).
- [17] B. Frick, B. Farago, D. Richter, *Phys. Rev. Lett.* **64**, 2921 (1990).
- [18] A. Arbe, U. Buchenau, L. Willner, D. Richter, B. Farago, J. Colmenero, *Phys. Rev. Lett.* **76**, 1872 (1996).
- [19] A. Meyer, J. Wuttke, W. Petry, A. Peker, R. Bormann, G. Coddens, L. Kranich, O. G. Rand, H. Schober, *Phys. Rev. B* **53**, 12107 (1996).
- [20] A. Meyer, J. Wuttke, W. Petry, O. G. Rand, H. Schober, *Phys. Rev. Lett.* **80**, 4454 (1998).
- [21] A. Meyer, R. Busch, H. Schober, *Phys. Rev. Lett.* **83**, 5027 (1999).
- [22] W. Petry and J. Wuttke, *Transp. Theory Stat. Phys.* **24**, 1075 (1995).
- [23] C. A. Angell, *Science* **267**, 1924 (1995).
- [24] E. McLaughlin, A. R. Ubbelohe, *Trans. Faraday Soc.* **54**, 1804 (1957).
- [25] R. J. Greet, D. Turnbull, *J. Chem. Phys.* **46**, 1243 (1967).
- [26] W. T. Laughlin, D. R. Uhlmann, *J. Phys. Chem.* **76**, 2317 (1972).
- [27] M. Cukierman, M. Lane, D. R. Uhlmann, *J. Chem. Phys.* **59**, 3639 (1973).
- [28] K. U. Schug, H. E. King, R. Böhmer, *J. Chem. Phys.* **109**, 1472 (1998).
- [29] J. N. Andrews, A. R. Ubbelohe, *Proc. Roy. Soc. A* **228**, 435 (1955).
- [30] G. M. Brown, H. A. Levy, *Acta Cryst. B* **35**, 785 (1979).
- [31] S. Aikawa, Y. Maruyama, *Acta Cryst. B* **34**, 2901 (1978).
- [32] I. L. Karle, L. O. Brockway, *J. Am. Soc.* **66**, 1974 (1944).
- [33] I. Baraldi, G. Ponterini, *J. Mol. Struct.* **122**, 287 (1985).
- [34] B. Geil, Ph. D. Thesis, Universität Mainz, 1994.
- [35] S. Mossa, R. Di Leonardo, G. Ruocco, M. Sampoli, *Phys. Rev. E* **62**, 612 (2000).
- [36] A. Tölle, H. Zimmermann, F. Fujara, W. Petry, W. Schmidt, H. Schober, J. Wuttke, *Eur. Phys. J. B* **16**, 73 (2000).
- [37] J. H. Magill, Hin-Mo Li, *J. Crystall Growth* **20**, 135 (1973).
- [38] G. Scherer, D. R. Uhlmann, C. E. Miller, K. A. Jackson, *J. Crystall Growth* **23**, 323 (1974).
- [39] P. I. K. Onorato, D. R. Uhlmann, *J. Non-Cryst. Solids* **41**, 189 (1980).
- [40] H. Yinnon, D. R. Uhlmann, *J. Non-Cryst. Solids* **44**, 37 (1981).
- [41] H. Yinnon, D. R. Uhlmann, *J. Non-Cryst. Solids* **50**, 189 (1982).
- [42] A. Tölle, H. Schober, J. Wuttke, F. Fujara, *Phys. Rev. E* **56**, 809 (1997).
- [43] S. S. Chang, A. B. Bestul, *J. Chem. Phys.* **56**, 503 (1972).
- [44] R. J. Greet, D. Turnbull, *J. Chem. Phys.* **47**, 2185 (1967).
- [45] T. Atake, C. A. Angell, *J. Phys. Chem.* **83**, 3218 (1979).

- [46] M. Naoki, S. Koeda, *J. Phys. Chem.* **93**, 948 (1989).
- [47] G. Fytas, C. H. Wang, D. Lilge, Th. Dorfmüller, *J. Chem. Phys.* **75**, 4247 (1981).
- [48] G. Fytas, Th. Dorfmüller, C. H. Wang, *J. Phys. Chem.* **87**, 5045 (1983).
- [49] Y.-H. Hwang, G. Q. Shen, *J. Phys. Condens. Matter.* **11**, 1453 (1999).
- [50] J. Wuttke, I. Chang, O. G. Randl, F. Fujara, W. Petry, *Phys. Rev. E* **54**, 5364 (1996).
- [51] R. Kohlrausch, *Pogg. Ann. Phys.* **91**, 56 and 179 (1854).
- [52] F. Kohlrausch, *Pogg. Ann. Phys.* **119**, 337 (1863).
- [53] H. Z. Cummins, Y. H. Hwang, G. Li, W. Du, W. Losert, G. Q. Shen, *J. Non-Cryst. Solids* **235–237**, 254 (1998).
- [54] P. Debye, *Polar Molecules*, Dover (1929).
- [55] K. S. Cole, R. H. Cole, *J. Chem. Phys.* **9**, 341 (1941).
- [56] D. W. Davidson, R. H. Cole, *J. Chem. Phys.* **19**, 1484 (1951).
- [57] S. Havrilak, S. Negami, *Polymer* **8**, 161 (1967).
- [58] G. Williams, D. C. Watts, *Faraday Soc.* **66**, 80 (1970).
- [59] G. P. Johari, M. Goldstein, *J. Chem. Phys.* **53**, 2372 (1970).
- [60] M. Naoki, H. Endou, and K. Matsumoto, *J. Phys. Chem.* **91**, 4169 (1987).
- [61] L. Wu, S. R. Nagel, *Phys. Rev. B* **46**, 11198 (1992).
- [62] C. Hansen, R. Richert, *J. Phys.: Condens. Matter* **9**, 9661 (1997).
- [63] C. Hansen, F. Stickel, T. Berger, R. Richert, E. W. Fischer, *J. Chem. Phys.* **107**, 1086 (1997).
- [64] G. Williams, P. J. Hains, *Chem. Phys. Lett.* **10**, 585 (1971).
- [65] G. Williams, P. J. Hains, *Faraday Symp. Chem. Soc.* **6**, 14 (1972).
- [66] M. F. Shears, G. Williams, *J. Chem. Soc. Faraday Trans. II*, **69**, 608 and 1050 (1973).
- [67] M. Davis, P. J. Haines, G. Williams, *J. Chem. Soc. Faraday Trans. II*, **69**, 1785 (1973).
- [68] M. Nakamura, H. Takahashi, K. Higashi, *Bull. Chem. Soc. Jpn.* **47**, 1593 (1974).
- [69] T. Nagai, Y. Koga, H. Takahashi, K. Higashi, *Bull. Chem. Soc. Jpn.* **47**, 1022 (1974).
- [70] M. Naoki, M. Matsushita, *Bull. Chem. Soc. Jpn.* **56**, 2396 (1983).
- [71] P. K. Dixon, L. Wu, S. R. Nagel, *Phys. Rev. Lett.* **65**, 1108 (1990).
- [72] P. D. Hyde, T. E. Evert, M. D. Ediger, *J. Chem. Phys.* **93**, 2274 (1990).
- [73] M. T. Cicerone, F. R. Blackburn, M. D. Ediger, *J. Chem. Phys.* **102**, 471 (1995).
- [74] L. Andreozzi, A. Di Schino, M. Giordano, D. Leporini, *Europhys. Lett.* **38**, 669 (1997).
- [75] K. A. Earle, J. K. Moscicki, A. Polimeno, J. H. Freed, *J. Chem. Phys.* **106**, 9996 (1997).
- [76] E. Rössler, K. Börner, J. Tauchert, M. Taupitz, M. Pöschl, *Ber. Bunsenges. Phys. Chem.* **95**, 1077 (1991).
- [77] P. K. Dixon, S. R. Nagel, *Phys. Rev. Lett.* **61**, 341 (1988).
- [78] R. Böhmer, K. L. Ngai, C. A. Angell, J. D. Plazek, *J. Chem. Phys.* **99**, 4201 (1993).
- [79] K. L. Ngai, *Phys. Rev. E* **57**, 7346 (1998).
- [80] C. A. Angell, *J. Non-Cryst. Solids* **131–133**, 15 (1991).
- [81] H. Z. Cummins, G. Li, Y. H. Hwang, G. Q. Shen, W. Du, J. Hernandez, N. J. Tao, *Z. Phys. B* **103** 501 (1997).
- [82] E. Bartsch, F. Fujara, M. Kiebel, H. Sillescu, *Ber. Bunsenges. Phys. Chem.* **93**, 1252 (1989).
- [83] D. W. McCall, D. C. Douglass, D. R. Falcone, *J. Chem. Phys.* **50**, 3839 (1969).
- [84] Th. Dries, F. Fujara, M. Kiebel, E. Rössler, H. Sillescu, *J. Chem. Phys.* **88**, 2139 (1988).
- [85] W. Schnauss, F. Fujara, H. Sillescu, *J. Chem. Phys.* **97**, 1378 (1992).
- [86] A. Bondi, *J. Phys. Chem.* **68**, 441 (1964).
- [87] B. Geil, F. Fujara, H. Sillescu, *J. Mag. Res.* **130**, 18 (1998).
- [88] F. Fujara, B. Geil, H. Sillescu, G. Fleischer, *Z. Phys. B* **88**, 195 (1992).
- [89] M. Lohfink, H. Sillescu: Proceedings of the 1st Tohwa University International Symposium, Fukuoka, Japan 4–8 November 1991. American Institute of Physics Conference Proceedings, no. 256, 30 (1992).
- [90] I. Chang, F. Fujara, B. Geil, G. Heuberger, T. Mangel, H. Sillescu, *J. Non-Cryst. Solids* **172–174**, 248 (1994).

- [91] G. Hinze, H. Sillescu, J. Chem. Phys. **104**, 314 (1996).
- [92] I. Chang, H. Sillescu, J. Phys. Chem. B **101**, 8794 (1997).
- [93] E. Rössler, Phys. Rev. Lett. **65**, 1595 (1990).
- [94] R. Scherm, Ann. Phys. **7**, 349 (1972).
- [95] G. L. Squires, *Introduction to the Theory of Thermal Neutron Scattering*, Cambridge University Press: London (1984).
- [96] S. W. Lovesey, *Theory of Neutron Scattering from Condensed Matter*, Clarendon: Oxford (1984).
- [97] M. Bée, *Quasielastic Neutron Scattering*, Hilger: Bristol (1988).
- [98] L. van Hove, Phys. Rev. **95**, 249 (1954).
- [99] O. Schärpf, H. Capellmann, Phys. Stat. Sol. **A135**, 359 (1993).
- [100] O. Schärpf, *The Spin of the Neutron as a Measuring Probe*, Institut Max von Laue – Paul Langevin (1996).
- [101] O. Debus, H. Zimmermann, E. Bartsch, F. Fujara, M. Kiebel, W. Petry, H. Sillescu, Chem. Phys. Lett. **180**, 271 (1991).
- [102] V. F. Sears, Neutron News, **3**, 29 (1992).
- [103] K. Ibel, ed: The Yellow Book, *Guide to neutron research facilities at the ILL*, Institut Max von Laue – Paul Langevin (1994).
- [104] U. Buchenau, A. Wischnewski, D. Richter, B. Frick, Phys. Rev. Lett. **77**, 4035 (1996).
- [105] J. Wuttke, W. Petry, G. Coddens, F. Fujara, Phys. Rev. E **52**, 4026 (1995).
- [106] V. Sears, Adv. Phys. **24**, 2 (1975).
- [107] J. Wuttke, M. Kiebel, E. Bartsch, F. Fujara, W. Petry, H. Sillescu, Z. Phys. B **91**, 357 (1993).
- [108] M. Russina, F. Mezei, R. Lechner, S. Longeville, B. Urban, Phys. Rev. Lett. **84**, 3630 (2000).
- [109] J. Wuttke, preprint
- [110] K. Böning, W. Gläser, U. Hennings, E. Steichele, Atomwirtschaft und Atomtechnik”, Verlagsgruppe Handelsblatt, Januar 1993, p. 61
- [111] The European Spallation Source Study, Vol III, Report ESS-96-53-M, (1996); G. S. Bauer, Physica B **234–236**, 1214 (1997).
- [112] D. Dubbers, *ILL and the new Millennium*, Institut Max von Laue – Paul Langevin (2000).
- [113] P. de Gennes, Physica **25**, 825 (1959).
- [114] W. Steffen, B. Zimmer, A. Patkowski, G. Meier, E. W. Fischer, J. Non-Cryst. Solids **172–174**, 37 (1994).
- [115] A. Criado, F. J. Bermejo, A. de Andres, J. L. Martinez, Molec. Phys. **82**, 787 (1994).
- [116] D. Kirin, V. Volovšek and R. M. Pick, J. Mol. Struct. **482–483**, 421 (1999).
- [117] Y. Higashigaki, C. H. Wang, J. Chem. Phys. **74**, 3175 (1981).
- [118] C. H. Wang, X. R. Zhu, J. C. Shen, Mol. Phys. **62**, 749 (1987).
- [119] G. Monaco, L. Comez, D. Fioretto, Phil. Mag. B **77**, 463 (1998).
- [120] C. Masciovecchio, G. Monaco, G. Ruocco, F. Sette, A. Cunsolo, M. Krisch, A. Mermet, M. Soltwitsch, R. Verbini, Phys. Rev. Lett. **80**, 544 (1998).
- [121] G. Monaco, C. Masciovecchio, G. Ruocco, F. Sette, Phys. Rev. Lett. **80**, 2161 (1998).
- [122] G. Monaco, D. Fioretto, C. Masciovecchio, G. Ruocco, F. Sette, Phys. Rev. Lett. **82**, 1776 (1999).
- [123] W. Steffen, A. Patkowski, G. Meier, E. W. Fischer, J. Chem. Phys. **96**, 4171 (1992).
- [124] W. Steffen, G. Meier, A. Patkowski, E. W. Fischer, Physica A **201**, 300 (1993).
- [125] W. Steffen, A. Patkowski, H. Gläser, G. Meier, E. W. Fischer, Phys. Rev. E **49**, 2992 (1994).
- [126] A. Patkowski, W. Steffen, G. Meier, E. W. Fischer, J. Non-Cryst. Solids **172–174**, 52 (1994).
- [127] H. Z. Cummins, G. Li, W. Du, Y. H. Hwang, G. Q. Shen, Prog. Theo. Phys. Suppl. **126**, 21 (1997).
- [128] A. Patkowski, W. Steffen, H. Nilgens, E. W. Fischer, J. Chem. Phys. **106**, 8401 (1997).
- [129] G. Hinze, D. D. Brace, S. D. Gottke, M. D. Fayer, Phys. Rev. Lett. **84**, 2437 (2000).
- [130] G. Hinze, D. D. Brace, S. D. Gottke, M. D. Fayer, J. Chem. Phys. **113**, 3723 (2000).
- [131] J. Baschnagel, Phys. Rev. B **49**, 135 (1994).
- [132] W. Kob, H. C. Andersen, Phys. Rev. Lett. **73**, 1376 (1994).

- [133] P. Gallo, F. Sciortino, P. Tartaglia, S.-H. Chen, Phys. Rev. Lett. **76**, 2730 (1996).
- [134] L. J. Lewis, G. Wahnström, Solid State Commun. **86**, 295 (1993).
- [135] L. J. Lewis, G. Wahnström, Phys. Rev. E **50**, 3865 (1994).
- [136] S. R. Kudchakar and J. M. Wiest, J. Chem. Phys. **103**, 8566 (1995).
- [137] G. Wahnström, L. J. Lewis, Prog. Theo. Phys. Suppl. **126**, 261 (1997).
- [138] F. Sciortino, P. Tartaglia, J. Phys.: Condens. Matter **11**, A261 (1999).
- [139] R. Schilling in: R. Richert, A. Blumen (eds) *Disorder Effects on Relaxational Processes*, Springer, Berlin (1994).
- [140] W. Götze, Z. Phys. B **60**, 195 (1985).
- [141] W. Götze in: J. P. Hansen, D. Levesque, J. Zinn-Justin (eds) *Liquids, freezing and the glass transition*, North Holland, Amsterdam (1991).
- [142] W. Götze in: T. Riste (ed) *Phase Transitions and Relaxation in Systems with Competing Energy Scales* (NATO ASI Series C415), Kluwer: Dordrecht (1993).
- [143] W. Götze, J. Phys. Condens. Matter. **2**, 8485 (1990).
- [144] M. Fuchs, J. Non-Cryst. Solids **172–174**, 241 (1994).
- [145] M. Fuchs, I. Hofacker, A. Latz, Phys. Rev. A **45**, 898 (1992).
- [146] U. Bengtzelius, Phys. Rev. A **33**, 3433 (1986).
- [147] J. Bosse, J. S. Thakur, Phys. Rev. Lett. **59**, 998 (1987).
- [148] M. Nauroth, W. Kob, Phys. Rev. E **55**, 657 (1997).
- [149] M. Fuchs, W. Götze, M. R. Mayr, Phys. Rev. E **58**, 3384 (1998).
- [150] T. Franosch, M. Fuchs, W. Götze, M. R. Mayr, A. P. Singh, Phys. Rev. E **55**, 7153 (1997).
- [151] T. Gleim, W. Kob, cond-mat/9902003
- [152] T. Franosch, M. Fuchs, W. Götze, M. R. Mayr, A. P. Singh, Phys. Rev. E **56**, 5659 (1997).
- [153] R. Schilling, Th. Scheidsteger, Phys. Rev. E **56**, 2932 (1997).
- [154] S.-H. Chong, F. Hirata, Phys. Rev. E **58**, 6188 (1998).
- [155] L. Fabbian, A. Latz, R. Schilling, F. Sciortino, P. Tartaglia, C. Theis, Phys. Rev. E **60**, 5768 (1999).
- [156] E. Bartsch, H. Bertagnolli, P. Chieux, A. David, H. Sillescu, Chem. Phys. **169**, 373 (1993).
- [157] C. Masciovecchio, PhD Thesis Université Joseph Fourier, Grenoble I, 16 Octobre 1998.
- [158] E. Bartsch, H. Bertagnolli, G. Schulz, P. Chieux, Ber. Bunsenges. Phys. Chem. **89**, 147 (1985).
- [159] D. Morineau, C. Alba-Simionesco, M.-C. Bellisent-Funel, M.-F. Lauthié, Europhys. Lett. **43**, 195 (1997).
- [160] C. Theis, R. Schilling, Phys. Rev. E **60**, 740 (1999).
- [161] S. L. Ruby, B. J. Zabransky, P. A. Flinn, J. Phys. Colloq. C6 **37**, 745 (1976).
- [162] A. Vasquez, P. A. Flinn, J. Chem. Phys. **72**, 1958 (1972).
- [163] W. Petry, E. Bartsch, F. Fujara, M. Kiebel, H. Sillescu, B. Farago, Z. Phys. B **83**, 175 (1991).
- [164] E. Bartsch, F. Fujara, J. F. Legrand, W. Petry, H. Sillescu, J. Wuttke, Phys. Rev. E **52**, 738 (1995).
- [165] E. Bartsch, F. Fujara, J. F. Legrand, W. Petry, H. Sillescu, J. Wuttke, Phys. Rev. E **53**, 2011 (1996).
- [166] F. Fujara, J. Mol. Struct. **296**, 285 (1993).
- [167] M. Kiebel, E. Bartsch, O. Debus, F. Fujara, H. Sillescu, Phys. Rev. B **45**, 10301 (1992).
- [168] E. Bartsch, O. Debus, F. Fujara, M. Kiebel, H. Sillescu, Ber. Bunsenges. Phys. Chem. **95**, 1146 (1991).
- [169] L. Sjögren, W. Götze, *Dynamics of Disordered Materials*, (Eds.: D. Richter, A. J. Dianoux, W. Petry, J. Teixeira), Springer Proceedings in Physics 37, Springer Berlin (1989).
- [170] J. Gapinski, W. Steffen, A. Patkowski, A. P. Sokolov, A. Kisliuk, U. Buchenau, M. Russina, F. Mezei, H. Schober, J. Chem. Phys. **110**, 2312 (1999).
- [171] E. Bartsch, V. Frenz, J. Baschnagel, W. Schärftl, H. Sillescu, J. Chem. Phys. **106**, 3743 (1997).
- [172] A. Tölle, J. Wuttke, H. Schober, O. G. Randl, F. Fujara, Eur. Phys. J. B **5**, 231 (1998).
- [173] M. Fuchs, A. Latz, Physica A **201**, 1 (1993).

- [174] C. Alba-Simionescu, A. Tölle, D. Morineau, G. Coddens B. Farago, submitted.
- [175] P. B. Macedo, T. A. Litovitz, *J. Chem. Phys.* **42**, 245 (1965).
- [176] R. L. Cook, H. E. King, C. A. Herbst, D. R. Herschbach, *J. Chem. Phys.* **100**, 5178 (1994).
- [177] H. Leyser, A. Schulte, W. Doster, W. Petry, *Phys. Rev. E* **51**, 5899 (1995).
- [178] G. Li, H. E. King, W. F. Oliver, C. A. Herbst, H. Z. Cummins, *Phys. Rev. Lett.* **74**, 2280 (1995).
- [179] I. L. Spain, J. Paauwe, *High Pressure Technology*, Marcel Dekker: New York (1977).
- [180] D. Morineau, G. Dosseh, R. J.-M. Pellenq, M. C. Bellisent-Funel, C. Alba-Simionesco, *Molec. Sim* **20**, 95 (1997).
- [181] C. Alba-Simionesco, D. Morineau, B. Frick, N. Higoncq, H. Fujimori, *J. Non-Cryst. Solids* **235–237**, 367 (1998).
- [182] A. Tölle, H. Schober, J. Wuttke, O. G. Randl, F. Fujara, *Phys. Rev. Lett.* **80**, 2374 (1998).
- [183] B. Frick, C. Alba-Simionesco, J. Hendricks, L. Willner, *Prog. Theo. Phys. Suppl.* **126**, 213 (1997).
- [184] B. Frick, C. Alba-Simionesco, *Physica B* **266**, 13 (1999).
- [185] A. Tölle, H. Schober, J. Wuttke, F. Fujara, *Physica B* **234–236**, 428 (1997).
- [186] G. Pratesi, A. Belloso, F. Barocchi, *Eur. Phys. J. B* **18**, 283 (2000).
- [187] J. P. Hansen, I. R. McDonald, *Theory of simple liquids*, 2nd ed., Academic Press, London (1986).
- [188] J. P. Boon, S. Yip, *Molecular Hydrodynamics*, McGraw-Hill, New York (1980).
- [189] J. D. Weeks, D. Chandler, H. C. Andersen, *J. Chem. Phys.* **54**, 5237 (1971).
- [190] B. Bernu, J.-P. Hansen, Y. Hiwatari, G. Pastore, *Phys. Rev. A* **36**, 4891 (1987).
- [191] J. N. Roux, J. L. Barrat, J.-P. Hansen, *J. Phys. Condens. Matter* **1**, 7171 (1989).
- [192] J. L. Barrat, A. Latz, *J. Phys. Condens. Matter* **2**, 4289 (1990).
- [193] M. Paluch, J. Ziolo, S. J. Rzoska, P. Habdas, *Phys. Rev. E* **54**, 4008 (1996).
- [194] W. R. Busing, *J. Am. Chem. Soc.* **104**, 4829 (1982).
- [195] F. J. Bermejo *et al.*, *Phys. Rev. B* **53**, 5259 (1996).
- [196] C. Talón *et al.*, *Phys. Rev. B* **58**, 745 (1998).
- [197] U. Buchenau *et al.*, *Phys. Rev. B* **34**, 5665 (1986).
- [198] A. Criado, F. J. Bermejo, M. Garcia-Hernandez, J. L. Martinez, *Molec. Phys.* **80**, 1263 (1993).
- [199] R. Böhmer, G. Hinze, G. Diezemann, B. Geil, H. Sillescu, *Europhys. Lett.* **36**, 55 (1996).